UNIVERSIDADE D
COIMBRA

Joana Diogo Mingacho

DETECTION OF TERRESTRIAL GAMMA-RAY FLASHES FOR AIRCRAFT SAFETY

Dissertação no âmbito do Mestrado Integrado em Engenharia Física, ramo de Instrumentação orientada pelo Professor Doutor Rui Curado Silva e pelo Doutor Miguel Moita e apresentada ao Departamento de Física da Faculdade de Ciências e Tecnologia.

Outubro de 2020

Acknowledgments

I would like to acknowledge everyone who contributed positively to this thesis.

To my supervisors, Dr. Rui Curado Silva and Dr. Miguel Moita, for all the time available, for all the understanding, support, and encouragement throughout this project.

To LIP for the welcome and opportunity to carry out this project.

To my parents for making all this possible and for giving me the opportunity to study at the Physics Department, at the University of Coimbra.

To my brother for all the support, patience, and unconditional motivation.

To my friends and family who were present and accompanied me on this journey.

Abstract

In the scope this thesis, we address a relevant question that has been answered since Terrestrial Gamma-ray Flashes (TGFs) were first discovered by the Burst and Transient Source Experiment (BATSE) mission in 1994: are TGFs a danger or not for passengers and crew members of commercial flights? In order to address this question, we analyzed the main characteristics of the TGFs that have been measured mainly by gamma-ray astrophysics satellite observatories. TGF emissions are generated on top of cumulonimbus clouds, which can exceed 10 km in altitude and reach up to 20 km. These emissions typically lay in the energy range between 100 keV and 100 MeV. A brief study was also carried out on the conditions and situations in which commercial aircraft fly and what knowledge the crew has about TGFs. Thus, an interview was conducted with an aircraft pilot and two mechanics of commercial aircraft, concluding that TGFs are unknown to them and no detector is provided on-board to measure radiation. The main task of this research work was to estimated the absorbed dose and the effective dose in a human model inside an aircraft cabin, at a typical flight altitude, when irradiated by a TGF emission. Using real satellite TGF emissions' data, we implemented a simulation program based in MEGALib toolkit, which allowed us to calculate the total number of triggered events generated by a representative TGF emission irradiating a commercial aircraft model carrying human beings. Firstly, it was considered a simple model of aircraft, which was irradiated by monochromatic beams. In the second model, the fuselage made of aluminum was added. The emission beam from the source was also made progressively complex, with a real flow modeled to a power-law profile and geometry approximated to a cone-shaped beam. A human model was also built to estimate the absorbed dose and the effective dose. The results here presented show that TGFs can in fact present real risks to passengers and crew members of aircrafts at distances longer than 2.5 km from the emission site for passengers and at distances longer than 500 m, in the case of strong TGF emissions (1×10^{20} during 100 μs). Even medium intensity TGFs emissions (1×10^{18} during 100 μs) should be reported to passenger for distances of the order of 500 m from the emission site. The possibility to monitor TGFs on board commercial aircraft using a CdTe based radiation monitor was also accessed. Results show that such kind of devices are a fine option to alert and characterize the magnitude of the TGFs' emissions.

Keywords— Terrestrial gamma-ray flashes, Detector, Aircraft, Absorbed dose, Cumulonimbus clouds.

Contents

Acknowledgments **1**

Abstract **2**

Figure index **5**

Table index **8**

Acronym list **12**

1 Chapter 1: Introduction **14**
1.1 Motivation 14
1.2 Project overview and objectives 15
1.3 Project Management 15
1.4 Document structure and organization 16

2 Chapter 2: Presentation of the existing theoretical concepts and studies **17**
2.1 The discovery and beginning of the TGFs study 17
2.1.1 BATSE: Burst And Transient Source Experiment 17
2.1.2 RHESSI: Reuven Ramaty High Energy Solar Spectroscopic Imager . 18
2.1.3 Fermi Gamma-Ray Space Telescope 18
2.1.4 AGILE: Astrorivelatore Gamma a Immagini Leggero 18
2.2 Terrestrial Gamma-Ray Flashes 19
2.2.1 Production process 20
2.2.2 The first image of TGFs globally 21
2.3 Cumulonimbus clouds 22
2.3.1 Thunderstorms 25
2.4 Earth atmosphere 27
2.4.1 Atmosphere layers 27
2.4.2 Cosmic rays in the atmosphere 27
2.5 Commercial aircraft 28
2.5.1 Interactions with the aircraft structure 29
2.5.2 Commercial aircraft features 32
2.5.3 Radiation doses 33
2.5.4 Questionnaire to the pilot and to the commercial aircraft mechanics 34

3 Chapter 3: TGF and Aircraft Irradiation Simulation **37**
3.1 Techniques and simulation tools: Software framing 37
3.1.1 MEGALib versus GEANT4 37
3.1.2 MobaXterm 38

3.1.3 MEGALib: The Medium-Energy Gamma-ray Astronomy library . . 39
3.2 Methodology . . . 40
3.3 Atmosphere composition overview and model creation for the composition . 43
3.4 Simulation methodology . . . 50
3.4.1 Calibration with CdTe Cubic detector model . . . 51
3.4.2 Aircraft Primary Model Simulation Set . . . 55
3.4.3 Aircraft Primary Model at 10 km altitude . . . 58
3.4.4 Aircraft Primary Model: Monochromatic beam . . . 62
3.4.5 Aircraft Primary Model: Power-law . . . 69
3.4.6 Aircraft Primary Model: Cumulative Spectrum . . . 77
3.4.7 Aircraft Primary Model: Broken Power-law . . . 80
3.4.8 Aicraft Primary Model: Cone Beam . . . 82
3.4.9 A first approach to the study of the cone angle opening . . . 85
3.4.10 Aircraft Primary Model: Real flux . . . 88
3.5 Aircraft Intermediate Model: With Aluminium and Air . . . 93
3.6 Aircraft Advanced Model: Phantom . . . 96
3.7 Human model . . . 98
3.7.1 Absorbed dose for a human inside the aircraft advanced model . . . 101
3.7.2 Absorbed dose for strong TGFs: High flux . . . 102
3.8 CdTe TGF Monitor . . . 103

4 Chapter 4: Conclusions **107**
4.1 Limitations . . . 108
4.2 Future work . . . 108

Figure index

List of Figures

1 Global image of terrestrial gamma-ray flashes by ESA [5]. 22
2 The cumulus stage [40]. 23
3 The mature stage [40]. 23
4 The dissipation stage [40]. 24
5 Tripole structure of a cumulonimbus cloud [18]. 25
6 The annualized distribution of total lightning activity (in units of fl km^{-2} yr^{-1}) [21]. 26
7 An example of a possible equipment irradiation for an aircraft exposed to a flux of incoming electrons [26]. 29
8 An example of TGF irradiation on aircraft, producing photo-production of secondary neutrons [26]. 30
9 Diagram for the horizontal interaction of gamma radiation with the aluminum layer (yellow) and neutron production. 32
10 MobaXterm graphical interface. 39
11 Atmospheric density for different altitudes [18]. 44
12 Representation of the atmospheric density for different altitudes [18]. 44
13 He, cm^{-3}, as a function of the altitude (km) [2]. 46
14 O, cm^{-3}, as a function of the altitude (km) [2]. 46
15 Nitrogen (N_2), cm^{-3}, as a function of the altitude (km) [2]. 47
16 Oxygen (O_2), cm^{-3}, as a function of the altitude (km) [2]. 47
17 Argon, cm^{-3}, as a function of the altitude (km) [2]. 48
18 Hydrogen, cm^{-3}, as a function of the altitude (km) [2]. 48
19 Nitrogen, cm^{-3}, as a function of the altitude (km) [2]. 49
20 Mass density, g/cm^{-3}, as a function of the altitude (km) [2]. 49
21 Diagram for the simple model of the cubic detector. 52
22 Efficiency (%) for the CdTe cubic detector as a function of energy (keV). . 53
23 CIPHER detection plane efficiency (%) (triangles curve) as a function of energy (keV), simulated with GEANT4 [34] [33]. 54
24 Diagram for a beam hitting the aircraft primary model. 56
25 Efficiency (%) for the aircraft primary model as a function of source distance (m), for a 300 keV beam in air, at 1 atm. 57
26 Efficiency (%) for the aircraft primary model as a function of source distance (m), for a 300 keV beam in vacuum. 58
27 Efficiency (%) for the aircraft primary model as a function of source distance (m), for a 300 keV beam, at 10 km altitude. 60

28 Efficiency (%) for the aircraft primary model as a function of source distance (m), for a 300 keV beam for our Earth's surface atmosphere model at 1 atm. 62
29 Efficiency (%) for the aircraft primary model as a function of source distance (m), for a 100 keV, 1 MeV and 100 MeV beam at 10 km altitude. 64
30 Efficiency (%) for the aircraft primary model as a function of source distance (m), for a 100 keV, 1 MeV and 100 MeV beam at 7.5 km altitude. 67
31 Efficiency (%) for the aircraft primary model as a function of source distance (m), for a 100 keV, 1 MeV and 100 MeV beam at 12.5 km altitude. 69
32 Efficiency (%) for the aircraft primary model as a function of source distance (m), for BATSE photon indexes, through a power-law from 100 keV to 100 MeV, at 12.5 km altitude. 72
33 Efficiency (%) for the aircraft primary model as a function of source distance (m), for RHESSI photon index, through a power-law from 100 keV to 100 MeV, at 12.5 km altitude. 73
34 Efficiency (%) for the aircraft primary model as a function of source distance (m), for Fermi photon index, through a power-law from 100 keV to 100 MeV, at 12.5 km altitude. 74
35 Efficiency (%) for the aircraft primary model as a function of source distance (m), for AGILE photon index, through a power-law from 1 MeV to 7.6 MeV, at 12.5 km altitude. 76
36 Efficiency (%) for the aircraft primary model as a function of source distance (m), for AGILE photon index, through a power-law from 7.7 MeV to 100 MeV, at 12.5 km altitude. 77
37 Cumulative spectrum for RHESSI and AGILE data [25]. 78
38 Efficiency (%) for the aircraft primary model as a function of source distance (m), for a RHESSI and AGILE cumulative spectrum, through a power-law from 100 keV to 100 MeV, at 12.5 km altitude. 80
39 Efficiency (%) for the aircraft primary model as a function of source distance (m), through a broken power-law from 100 keV to 100 MeV, at 12.5 km altitude. 81
40 Diagram of representation for the bremsstrahlung process [12]. 82
41 Geometry scheme for photon emission [18]. 84
42 Geometry scheme used in the simulations for photon emission. 85
43 Efficiency (%) for the aircraft primary model as a function of source distance (km), for a source with a cone beam with different opening angles. 88
44 Triggered photons for a linear extrapolation to 100 μs, considering a horizontal beam incident on the aircraft primary model. 91
45 Triggered photons for a linear extrapolation to 100 μs, considering a horizontal beam incident on the aircraft primary model; Stopping time = 1×10^{-13}s. 92

46 Triggered photons for a linear extrapolation to 100 μs, considering a cone beam incident on the aircraft intermediate model, for three different fuselages thicknesses. 95
47 Triggered photons for a linear extrapolation to 100 μs, considering a cone beam incident on the aircraft advanced model, for each phantom component. 98
48 Diagram for the approximate human model, with cylindrical geometry, inside the aircraft advanced model. 99
49 Representation of the energy spectrum of the recorded energy of a medium intensity TGF inside a human model volume, obtained by MEGALib. . . . 100
50 Triggered photons for a linear extrapolation to 100 μs, considering a cone beam incident on human model, inside the aircraft advanced model. 101
51 Diagram for the 1 cm edge CdTe detector, placed inside the aircraft advanced model. 105
52 Triggered photons for a linear extrapolation to 100 μs, considering a cone beam incident on the CdTe detector, inside the aircraft advanced model. . . 106

Table index

List of Tables

1 TAP commercial aircraft [11]. 32
2 SATA commercial aircraft [9]. 33
3 Equivalent dose limit according to Decree-Law No. 222/2008 of 17 November, Portugal [3], for specific body components. 34
4 Cumulonimbus clouds characteristics. 41
5 Aircraft characteristics. 42
6 TGF emissions characteristics. 43
7 Initial parameters used [2]. 45
8 Source with 4 mm beam at 10 cm from the cubic detector; Material: Air. . 53
9 Source with a beam of 10 mm in diameter, with constant energy of 300 keV and at a distance d from the aircraft primary model; Material: Air at 1 atm. 56
10 Source with a beam of 10 mm in diameter, with constant energy of 300 keV and at a distance d from the aircraft primary model; Material: Vacuum. . . 57
11 Atmosphere composition at 10 km altitude. 59
12 Source with a beam of 10 mm in diameter, with constant energy of 300 keV and at a distance d from the aircraft primary model; Material: Atmosphere at 10 km of altitude. 59
13 Atmosphere composition at sea level. 61
14 Source with a beam of 10 mm in diameter, with constant energy of 300 keV and at a distance d from the aircraft primary model; Material: our Earth's surface atmosphere model at 1 atm. 61
15 Source with a beam of 10 mm in diameter, with constant energy of 100 keV and at a distance d from the aircraft primary model; Material: Atmosphere at 10 km altitude. 63
16 Source with a beam of 10 mm in diameter, with constant energy of 1 MeV and at a distance d from the aircraft primary model; Material: Atmosphere at 10 km altitude. 63
17 Source with a beam of 10 mm in diameter, with constant energy of 100 MeV and at a distance d from the aircraft primary model; Material: Atmosphere at 10 km altitude. 64
18 Atmosphere composition at 7.5 km altitude. 65
19 Atmosphere composition at 12.5 km altitude. 65
20 Source with a beam of 10 mm in diameter, with constant energy of 100 keV and at a distance d from the aircraft primary model; Material: Atmosphere at 7.5 km altitude. 66

21 Source with a beam of 10 mm in diameter, with constant energy of 1 MeV and at a distance d from the aircraft primary model; Material: Atmosphere at 7.5 km altitude. 66
22 Source with a beam of 10 mm in diameter, with constant energy of 100 MeV and at a distance d from the aircraft primary model; Material: Atmosphere at 7.5 km altitude. 67
23 Source with a beam of 10 mm in diameter, with constant energy of 100 keV and at a distance d from the aircraft primary model; Material: Atmosphere at 12.5 km altitude. 68
24 Source with a beam of 10 mm in diameter, with constant energy of 1 MeV and at a distance d from the aircraft primary model; Material: Atmosphere at 12.5 km altitude. 68
25 Source with a beam of 10 mm in diameter, with constant energy of 100 MeV and at a distance d from the aircraft primary model; Material: Atmosphere at 12.5 km altitude. 68
26 Source with a beam of 10 mm in diameter, with a power-law from 100 keV to 100 MeV, and at a distance d from the aircraft primary model; Material: Atmosphere at 12.5 km altitude; Photon index = 0.6. 70
27 Source with a beam of 10 mm in diameter, with a power-law from 100 keV to 100 MeV, and at a distance d from the aircraft primary model; Material: Atmosphere at 12.5 km altitude; Photon index = 1. 71
28 Source with a beam of 10 mm in diameter, with a power-law from 100 keV to 100 MeV, and at a distance d from the aircraft primary model; Material: Atmosphere at 12.5 km altitude; Photon index = 1.5. 71
29 Source with a beam of 10 mm in diameter, with a power-law from 100 keV to 100 MeV, and at a distance d from the aircraft primary model; Material: Atmosphere at 12.5 km altitude; Photon index = 2.6. 73
30 Source with a beam of 10 mm in diameter, with a power-law from 100 keV to 100 MeV, and at a distance d from the aircraft primary model; Material: Atmosphere at 12.5 km altitude; Photon index = 2.20 $\pm$0.13. 74
31 Source with a beam of 10 mm in diameter, with a power-law from 1 MeV to 7.6 MeV, and at a distance d from the aircraft primary model; Material: Atmosphere at 12.5 km altitude; Photon index = 0.5 $\pm$0.1. 75
32 Source with a beam of 10 mm in diameter, with a power-law from 7.7 MeV to 100 MeV, and at a distance d from the aircraft primary model; Material: Atmosphere at 12.5 km altitude; Photon index = 2.7 $\pm$0.1. 76
33 Source with a beam of 10 mm in diameter, with a power-law from 100 keV to 100 MeV, and at a distance d from the aircraft primary model; Material: Atmosphere at 12.5 km altitude; Photon index = 0.04 $\pm$0.03. 79

34 Source with a beam of 10 mm in diameter, with a power-law from 100 keV to 100 MeV, and at a distance d from the aircraft primary model; Material: Atmosphere at 12.5 km altitude; Photon index = $0.2^{+0.12}_{-0.13}$. 79
35 Source with a beam of 10 mm in diameter, with a broken power-law from 100 keV to 100 MeV, and at a distance d from the aircraft primary model; Material: Atmosphere at 12.5 km altitude; Photon index min = 1.7; Photon index max = 2.6. 81
36 Average atmosphere composition between 7.5 km and 12.5 km. 86
37 Average atmosphere composition between 10 km and 12.5 km. 86
38 Average atmosphere composition between 12 km and 12.5 km. 86
39 Source with a cone beam, with a power-law from 100 keV to 100 MeV; Photon index = 0.04; $\theta = 5^{o}$. 87
40 Source with a cone beam, with a power-law from 100 keV to 100 MeV; Photon index = 0.04; $\theta = 30^{o}$. 87
41 Source with a cone beam, with a power-law from 100 keV to 100 MeV; Photon index = 0.04; $\theta = 40^{o}$. 87
42 Source with a beam of 10 mm in diameter, with a power-law from 100 keV to 100 MeV, at a distance d from the aircraft primary model; Material: Atmosphere at 12.5 km altitude; TGF duration approximated to 10^{-15}s. . . 90
43 Source with a beam of 10 mm in diameter, with a power-law from 100 keV to 100 MeV, at a distance d from the aircraft primary model; Material: Atmosphere at 12.5 km altitude; Approximation by 10^{-14}s. 90
44 Source with a cone beam, with a power-law from 100 keV to 100 MeV, at a distance d from the aircraft primary model; Linear extrapolation for 100 μs. 92
45 Source with a cone beam, with a power-law from 100 keV to 100 MeV, at a distance d from the aircraft intermediate model; Average for 100 μs; shield = 1 cm. 94
46 Source with a cone beam, with a power-law from 100 keV to 100 MeV, at a distance d from the aircraft intermediate model; Average for 100 μs, for a 22 cm aluminum shield. 94
47 Source with a cone beam, with a power-law from 100 keV to 100 MeV, at a distance d from the aircraft intermediate model; Average for a 100 μs duration TGF, for a 25 cm aluminum shield. 95
48 Source with a cone beam, with a power-law from 100 keV to 100 MeV, at a distance d from the aircraft advanced model; Average for 100 μs duration TGF, for the different phantom components. 97
49 Source with a cone beam, with a power-law from 100 keV to 100 MeV, at a distance d from the aircraft advanced model; Average for 100 μs, for a human model consisting of water. 100
50 Absorbed doses for the human model consisting of water, inside the aircraft advanced model, for medium intensity TGFs. 102

51 Absorbed doses for the human model consisting of water, inside the aircraft advanced model for strong TGFs. 103
52 Triggered photons by approximation for a 1 cm edge CdTe detector. 105

Acronym list

AC Anticoincidence system

AGILE Astrorivelatore Gamma ad Immagini Leggero

AGN Active Galactic Nuclei

ASCII American Standard Code for Information Interchange

ASI Italian Space Agency (Agenzia Spaziale Italiana)

ASIM Atmosphere-Space Interactions Monitor

BATSE Burst And Transient Source Experiment

CARI Care and Resilience Index

CERN European Organization for Nuclear Research

CG Cloud-to-Ground

CIPHER Coded Imager and Polarimeter for High Energy Radiation

CNEN National Nuclear Energy Commission

COVID-19 Coronavirus Disease 2019

DD Displacement Damage

DR Dose Rate

ENTLN Earth Networks Total Lightning Network

ESA European Space Agency

EPCARD European Program Package for the Calculation of Aviation Route Doses

FDP Flight Duty Period

GBM Gamma-Ray Burst Monitor

GEANT4 "for GEometry ANd Tracking"

GRB Gamma-Ray Burst

GRID AGILE Gamma-Ray Imaging Detector

i-Astro space Instrumentation for ASTROphysics

IC Intra-Cloud

LAT Large Area Telescope

LIP Laboratory of Instrumentation and Experimental Particle Physics

MCAL Mini-Calorimeter

MEGALib Medium-Energy Gamma-ray Astronomy library

NASA National Aeronautics and Space Administration

NIM Nuclear Instrumentation Module

OTD Optical Transient Detector

PC-AIRE Predictive Code for AIrCrew Radiation Exposure

PGD Patterned Gas Detectors

RFD Relativistic feedback discharge

RHESSI Reuven Ramaty High Energy Solar Spectroscopic Imager

RPC Resistive Plate Chambers

RREA Relativistic Runaway Electron Avalanche

SAFE Safety in Aviation Forum for Europe

SATA Serviço Açoriano de Transportes Aéreos

SEE Single Event Effects

SSH Secure Socket Shell

TAP Transportes Aéreos Portugueses

TARANIS Tool for the Analysis of Radiation from Lightning and Sprites

TERA Thunderstorm Energetic Radiation Array

TGF Terrestrial Gamma-ray Flashes

TLE Transient Luminous Events

TID Total Ionizing Dose

WWLLN World Wide Lightning Location Network

1 Chapter 1: Introduction

This chapter will introduce and present the motivation and the context of this this master's dissertation. It is also important to mention the team and the work already done in the laboratory that led to this thesis manuscript. The main objective and the different steps to be achieved will also be mentioned. Finally, it will present the overall structure of the thesis.

1.1 Motivation

This dissertation focuses on the detection of Terrestrial Gamma-ray Flashes (TGF) for aviation safety, aiming to achieve a scientific answer about the possibility that these gamma-ray flashes might present risks for crews and passengers of different kinds of aircrafts: commercial, scientific or military. The motivation lies in the need to access the TGFs impact on the passenger's health when crossing, bypassing or over a cumulonimbus cloud. For this reason, this knowledge has a social impact, as it affects aircraft safety.

Furthermore, it is intended to develop a CdTe (Cadmium Telluride) detector operating as a radiation monitor to estimate the dose absorbed by the crew and by passengers exposed to a TGF emission during a commercial flight. So, as future work, a CdTe detector will be designed and optimized to be deployed on-board an aircraft in order to provide an optimal record for harmful and harmless TGFs. The objective of the development of a TGF monitor is to contribute to the safety of the crew and passengers, by measuring the intensity of the flow, the duration, and the spectral profile, when a TGF occurs in a cumulonimbus cloud next to an aircraft, which flies in its vicinity. Since TGFs are distinctly detected by satellites in space, the range of these TGF emissions can reach distances of up to 500 km. Therefore, even at distances of a few tens of kilometers, at commercial flight altitude ($\sim$10 km), where the air is rarer and the absorption of gamma-rays by the atmosphere is substantially less, the flow of TGF emissions can pose a danger and this is important to determine. Although aircraft are the safest means of transporting mass passengers and TGF is a rare phenomenon, occurring more frequently near the tropics and over land masses, it is, therefore, essential to understanding the level of health risks that are exposed, in particular the dose absorbed by the crew and passengers in the vicinity of a TGF emission. TGF emissions and their potential risks are still relatively unknown among airlines. Therefore, no product or idea that offers any type of crew and passenger monitoring has been proposed. A CdTe TGF monitor may also address a market opportunity, without competition so far. Potential users of a TGF monitor may be almost global, with a particular focus on airlines, military or scientific aircrafts operating in tropical regions. A TGF monitor prototype must provide output spectra with a level of sensitivity that allows the characterization of a typical TGF emission (spectrum, flow, and duration) in order to determine its risks to the health of the crew and passengers.

It should also be noted that this thesis work is a spin-off of LIP i-Astro (space In-

strumentation for ASTROphysics) group research activities, in particular from activities concerning the development of gamma-ray telescope detection planes based on CdTe detectors' technology. It must be stressed that as a spin-off activity of the main research lines of our group, this thesis is not only a challenge for all of us, as well it represents a risky decision, as it is always risky when addressing not only a new research field for the group but also a novel research field, since TGFs were discovered as recently as 1994. Therefore, this thesis also stands as a path-finder activity with all the associated risks and uncertainties, which we hope will provide further future work with extended ramifications and deeper conclusions.

1.2 Project overview and objectives

The main objective is to access the health risks associated to commercial flight when exposed to a TGF emission, for typical commercial flight altitudes, circa 12 km high. The main topics to be addressed are evaluating the TGFs' emission flux at commercial flight altitude, assessing the potential dose absorbed by the crew. The object of work and analysis in this project is simulation data that allow to access the number of photons detected in a human model volume. In other words, based on the number of events recorded, it is intended to estimate at the absorbed dose and the dose equivalent, to access the greater or lesser degree of harmfulness of TGFs, for the human body and for the different irradiation scenarios.

Another objective that goes beyond this thesis time frame, is to to build a partnership for the further development of the CdTe monitor, to contribute to make aviation a safer activity. With this intent, we contacted Safety in Aviation Forum for Europe (SAFE), to present and discuss TGFs potential risks for aircraft crew of commercial airlines. However, probably due to Coronavirus Disease 2019 (COVID-19) and the deep crisis in the airline sector, the contact with SAFE had no developments during the last months. Further contact will be made with other commercial airlines' institutions, to create an eventual partnership, such as national aviation safety agencies and crews' and pilots' unions.

1.3 Project Management

This project takes place at Laboratory of Instrumentation and Experimental Particle Physics (LIP), at the Physics Department of the University of Coimbra. LIP is a reference national laboratory conducting research on experimental particle physics and associated technologies, that has been working in relevant projects with international research infrastructures and organizations, such as European Organization for Nuclear Research (CERN) or European Space Agency (ESA). The LIP emerged to unite the community of experimental particle physicists. CERN was the first scientific organization in which Portugal became a member. Its areas of research are particle physics and the new instruments and methodologies development for applications in other scientific domains. Staff training and

scientific dissemination are other LIP priorities. LIP staff totals more than 200 people. This project is supervised by Dr. Rui Curado Silva and Dr. Miguel Moita and is being developed at the space Instrumentation for ASTROphysics (i-Astro) group that is composed by circa 12 researchers and students. i-Astro group operates in LIP pole located in Coimbra, specialized on radiation detection, having a long history of building Patterned Gas Detectors (PGD), as well as Resistive Plate Chambers (RPC) and Xenon based detectors. i-Astro has access to facilities such as modern mechanical and electronics workshops that provide essential services for detector prototype's development. LIP laboratorial rooms are equipped with indispensable equipment (Nuclear Instrumentation Module (NIM) modules, oscilloscopes, multichannel analyzers and radioactive sources, etc.) for solid state detector testing. Projects developed in Coimbra have generated applications in medical physics and space exploration.

1.4 Document structure and organization

The document structure is divided into four chapters. The first chapter presents the introduction, covering the motivation, the objectives and the work team, working as the project presentation.

The second chapter refers to the state of the art and the theoretical presentation of the concepts. Namely the Terrestrial Gamma-ray Flashes, the existing space programs, the cumulonimbus clouds and the commercial aircraft. Also presented in this chapter is a set of questions and answers from airline pilots.

The third chapter is completely dedicated to all the simulations performed, as well as small conclusions about the data obtained. Tables, graphs, and diagrams are mostly found here. The software architecture and the Medium-Energy Gamma-ray Astronomy library (MEGALib) description is also introduced in this section.

Finally, the fourth chapter presents the conclusions and the objectives accomplished of this project. The limitations, difficulties encountered and suggestions for future work will also be addressed.

2 Chapter 2: Presentation of the existing theoretical concepts and studies

In this topic the theoretical context of the project will be presented. Thus, the theoretical concepts to be addressed in this master thesis are defined here, as well as values and graphics obtained through studies on the subject. A set of questions, made to a pilot and two mechanics of commercial aircraft, are also presented.

2.1 The discovery and beginning of the TGFs study

The Terrestrial Gamma-ray Flashes, also nominated TGFs, are gamma-ray emissions which occur in the Earth's atmosphere. Currently, there are three operational space instruments for detecting TGFs: the Reuven Ramaty High Energy Solar Spectroscopic Imager (RHESSI), the Gamma-Ray Burst Monitor (GBM) on board the Fermi satellite, and the Astrorivelatore Gamma ad Immagini Leggero (AGILE).

2.1.1 BATSE: Burst And Transient Source Experiment

TGFs were first discovered in 1994 by Burst And Transient Source Experiment (BATSE), aboard National Aeronautics and Space Administration (NASA) Compton Gamma-Ray Observatory. BATSE was launched on April 5, 1991, in a low earth orbit of 450 km high, with a slope of 28.5^{o}. Although the main objective was to measure cosmic Gamma-Ray Burst (GRB), BATSE detected 78 TGFs during its 8 years of operation [18].

Initially, using BATSE data, it was established that the TGF duration was 1 ms and had energies above 1 MeV. However, the reading made by BATSE was not correct, since the electronic system was not fast enough to detect all received pulses. Also, the instrument saturation and the Compton dispersion in the atmosphere brought errors to the data, artificially increasing the TGFs duration. This also allowed to determine that TGFs are produced at a low altitude, less than 20 km high. Later with RHESSI and Fermi - GBM, it was found that the typical TGF duration is between 50 μs and 1 ms, having an average of 200 μs.

Thereafter, it was raised the hypothesis that the TGFs source was related to other atmospheric phenomena, namely with red sprites, blue jets, and transionospheric pulse pairs. The similarity with the red sprites arises from the fact that it has a duration of milliseconds, reaching up to 90 km high. On the other hand, blue jets reach 50 km and are characterized by their conical shape, oriented vertically, in its emission. The blue jets' duration is in the order of tens of seconds. On the other hand, transionospheric pulse pairs happen in pairs, so they were associated due to the fact that there were TGFs with two pulses. Finally, comparing the three atmospheric events, it was found that the strongest hypothesis would be the red sprites [32].

2.1.2 RHESSI: Reuven Ramaty High Energy Solar Spectroscopic Imager

RHESSI was launched on February 5, 2002, with an orbit of 600 km in altitude and 38º of inclination. The limit of TGFs detection energies increased with RHESSI, being able to measure up to 20 MeV, beating the BATSE that could only capture up to 1 MeV [18]. Besides, the detection rate also increased, giving a total of 820 TGFs detected from 2002 to 2008, a significant growth when compared to BATSE [24]. It is believed that RHESSI, like other satellites, only captures TGFs that have higher energy and can reach the satellite's altitude. Photons always suffer atmospheric attenuation and if they have less energy they may not be able to be detected in space.

Also through RHESSI it was discovered that TGFs have a lower origin, 15 to 21 km in altitude and that they do not come from red sprites [23]. The RHESSI cumulative spectrum also complies with these altitude limits and is compatible with radiation from high energy electrons produced through Relativistic Runaway Electron Avalanche (RREA). The TGFs observed by RHESSI at a latitude below 2.5º are compatible with those detected by AGILE, for the same orbit latitude. There is a good agreement between the AGILE and RHESSI spectra, the only differences being in the intensities distribution are due to calibration and dead time problems [24].

2.1.3 Fermi Gamma-Ray Space Telescope

The Fermi Gamma-ray Space Telescope consists of two instruments: the Large Area Telescope (LAT) and the GBM. Its orbit has an inclination of 25.6º, located above the tropics, for an altitude of 560 km. LAT observes gamma-rays between 20 MeV and 300 GeV. GBM is composed by 14 detectors, of which 12 are NaI (Sodium Iodide) scintillation detectors, with an energy range between 8 keV and 1 MeV. The remaining two are BGO (Bismuth Germanate) scintillation detectors, covering 200 keV to 40 MeV of energy. GBM records approximately 100 counts per TGF. Finally, the TGF duration resolution is 2 μs [35]. The satellite was launched on June 11, 2008, and, from that date until March 16, 2013, it detected approximately 1330 TGFs, although its main objective was to detect GRBs. The GBM made it possible to correlate TGFs with storms and conclude that they are associated with individual lightning strikes by matching 287 TGFs to lightning rays from the World Wide Lightning Location Network (WWLLN) and Earth Networks Total Lightning Network (ENTLN)[17].

2.1.4 AGILE: Astrorivelatore Gamma a Immagini Leggero

The Astrorivelatore Gamma ad Immagini Leggero (AGILE) is a scientific space mission whose objective is to detect high-energy events. This satellite is able to record photons within two energy bands: the 10 keV-40 keV X-ray band and the 30 Mev-50 GeV gamma-ray band [28].

It was launched on April 23, 2007 by Italian Space Agency (Agenzia Spaziale Italiana) (ASI) and it is a large combination of sensors, which are the silicon-tracker, the Super-AGILE, the Mini-Calorimeter (MCAL), the Anticoincidence system (AC) and the data handling system. All of them allow the AGILE to perform many tasks, such as monitoring Active Galactic Nuclei (AGN), GRBs and solar flares. It can also detect the diffuse galactic and extra-galactic emission. The MCAL and the gamma-ray tracker detect TGFs and impulsive events, and are highly efficient at detecting photons with energies greater than tens of MeV. Between March 2009 and July 2012, AGILE had a detection rate of approximately 10 TGFs/month, that is, 0.3 TGFs/day [25]. TGFs are geographically distributed throughout the equatorial region, always associated with the lightning distributions [26]. In fact, in tropical regions, the ratio between TGFs and normal lightning is 10^{-4} [26]. Events were recorded in Africa, between 0^{o} and 30^{o} longitude, corresponding to half of the total number of observations. In Southeast Asia, TGFs were observed between 90^{o} and 120^{o} longitude, one-third of the total.

In addition, some of AGILE's specifications are very suitable to detect TGFs, such as the ones listed below:

1. It covers $\sim 1/5$ of the earth sphere [28];

2. The AGILE Gamma-Ray Imaging Detector (GRID) has the smallest dead time ever observed for the detection of gamma-rays, being ≤ 200 μs [28];

3. The orbit is low with 550 km of altitude and it's equatorial, with a slope of 2.5^{o} [27]. Due to its very low inclination orbit, AGILE has the highest density of detection rate in the equatorial region;

4. MCAL acquires data per sub millisecond trigger and allows to sample the highest emitted photon energies. It has an energy range of 0.35 up to 100 MeV [27].

2.2 Terrestrial Gamma-Ray Flashes

The majority of TGFs were detected by satellites at a low orbit and, in average, at least one TGF explosion occurs in each thunderstorm [23]. Its average duration is 200 μs [26] and by observing its geographical distribution, there is a peak in the equatorial regions [27]. The TGF rate per day is 10^2 - 10^3 and depends on the geometry and intensity of the flow [27]. Regarding their location in the Earth's atmosphere, TGFs are located in the tropopause, which lies between the troposphere and the stratosphere, at an average altitude of 17 km from the equator. The shorter pulses detected by satellites are equivalent to very short emissions of TGFs, about 10 μs.

In August 2003, Dwyer [23] saw an intense gamma-ray flash at sea level, having a much higher energy range than X-rays, coming from lightning, and a pulse shape equivalent to individual photons. This flash registered energies above 10 MeV, implying that it was

formed from a RREA. On June 30, 2009, a gamma-ray flash was also observed at ground level, with a duration of 52.7 μs. The phenomenon was detected by the station - 19 Thunderstorm Energetic Radiation Array (TERA) and had an energy spectrum consistent with RREA, being the definitive association of TGFs with natural cloud-to-ground rays.

Gamma-rays experience strong attenuation in the atmosphere. As the distance increases between the source and the observer, the TGF decreases its intensity and its time duration, due to Compton dispersion. Compton scattering is also responsible for changing direction and reducing photon energies. Thus, photons that have less energy, suffer a greater dispersion, traveling a long path up to the satellite altitude and, consequently, are detected during a longer period of time. This lag was visible in 15 BATSE TGFs, having been quantified through the difference between the peak of the weak counts (25 - 110 keV) and the peak of the strongest counts ($>$ 110 keV). The time lag varied from 70 to 370 μs, which average value was 100 μs. Later, through 431 TGFs observed by RHESSI, it was found that the time delay, again between weak and strong counts, was $28.0 \pm 0.3\mu$s. This difference in value is justified by the fact that in the BATSE initial results, the dead time effects were not considered. In turn, the time delay values, observed by Fermi - GBM, are between 20 and 80 μs, with an average value of approximately 24 μs, very close to that verified in RHESSI [17].

From the analysis of 820 TGFs observed from the first RHESSI sample, there is no case of several peaks, that is, it is concluded that TGFs are isolated events. Subsequently, a larger sample was obtained, with three times more values than the initial one, where few examples of double peak TGFs were found. Also in the Fermi satellite, in 53 TGFs, three had a double peak [25]. The longest ones, $\geq$ 100 ms, are a set of overlapping emissions, which individually have a short period. So, a TGF pulse can not only be individual, but can also be a set of multiple emissions. Considering the individual impulses, the TGF can be symmetric or asymmetric and Fermi observed that 67% of TGFs are asymmetric, at satellite altitude [35]. In the symmetrical, there is a rise time approximately equal to the descent time. In an asymmetric pulse, the time on the rise is faster than in the fall, and the fall time varies from 50 to 200 μs [35]. This situation was initially observed by BATSE.

2.2.1 Production process

In the atmosphere, there is naturally cosmic radiation, which allows the formation of secondary particles, such as electrons. The frictional force on the electrons decreases with increasing energy, so when applying an electric field, the electrical accelerating force can exceed the frictional force of the electrons, which have an average energy of 7.2 MeV [22]. This allows the electrons to gain energy, now called runaway electrons, and when they collide with air molecules, produce bremsstrahlung radiation. This phenomenon is called the Relativistic Runaway Electron Avalanche (RREA) and can occur in thunderstorms. TGFs also involve the production of X-rays, due to the interactions of these electrons with air [22]. Through the avalanche, relativistic feedback can happen, where positrons and

photons are created and produce more energetic electrons.

Connaughton [15] found a relationship between WWLLN sferics and Fermi-measured TGFs. Thus, in 50 TGFs, 15 matches were found. Later, in 972 TGFs captured by RHESSI, Collier [14] discovered 93 equivalences. Thus, it is suggested that TGFs have the same place of origin as a sferic, that is, they are produced in the initial phase of a lightning discharge. So, TGFs formation is associated with intra-cloud discharges at an altitude between 10 km to 20 km [26], this is, they happen at the same time as a leader is propagating inside the cumulonimbus cloud. The leader is defined as the lightning channel. The channel that corresponds to the initial lightning stroke is called a stepped leader, which consequently will be branched as the lightning division occurs. The electric fields created have a spherical shape, which center is on the leader. This way, TGFs can be defined as natural accelerators, because they are produced by RREA and the amount of electrons produced can reach values of 10^{17} - 10^{18} [26], which generate radiation. Previous simulations have shown that for a source at 21 km altitude, corresponding to 50 g/cm^2 of atmospheric density, 1×10^{16} runaway electrons with energies greater than 1 MeV are obtained. For a source at 15 km altitude (130 g/cm^2), there are 2×10^{17} runaway electrons and 10^{23} secondary electrons, due to air ionization [22]. Naturally, the energy of the electrons must be greater than the energy of the photons, since the photons undergo atmospheric attenuation and Compton dispersion, until reaching the satellite's altitude. They radiate by bremsstrahlung and have an energy range between 100 keV to 100 MeV.

TGFs production electromagnetic component is composed by electrons and positrons, these result from pair production processes. Besides this electromagnetic component there is also a neutron component, that will be addressed later.

TGFs can also be classified into two categories [36]:

1. Lightning leader emissions: In this model, TGFs are generated by large-scale electric fields of thunderclouds or formed by fields associated with the lightning leader.

2. Relativistic feedback discharge (RFD): The relativistic runaway electron avalanches are produced by the formation of runaway positrons and back-scattered X-rays.

However, it is unknown the accurate acceleration distance inside the cloud, it can be between 50 to 100 m, which corresponds to a step-leader size, or even bigger. And then the TGF consists of a primary flow of electrons/positrons and gamma-rays within the lightning discharge channel.

2.2.2 The first image of TGFs globally

Not all instruments that detected TGFs were designed for that purpose. Currently, Atmosphere-Space Interactions Monitor (ASIM) and Tool for the Analysis of Radiation from Lightning and Sprites (TARANIS) are designed to detect TGFs. On December 12, 2019 an article was published by ESA stating that the ASIM team obtained the first

image of TGFs globally. From the 217 flashes detected, it was possible to identify the source location of 30 flashes [5]. ASIM's goal is to detect TGFs and Transient Luminous Events (TLE), both occurring at the top of storm clouds. TLEs are events that include sprites, blue jets, and elves and consist of electromagnetic discharges, in the atmosphere. Its typical altitude is well above storm lightning and represents the family of events that occur in the upper atmosphere. ASIM has two instruments: one to detect TGFs, which is a X- and gamma-ray instrument, and the other to detect TLEs, consisting of an optical instrument.

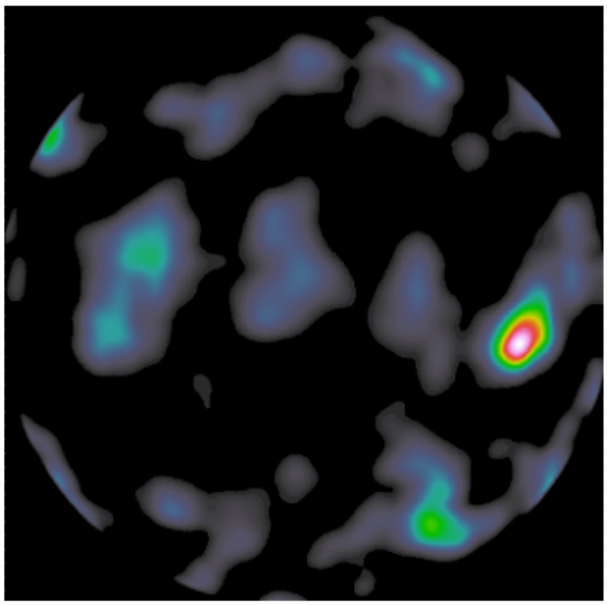

Figure 1: Global image of terrestrial gamma-ray flashes by ESA [5].

From figure 1 it is possible to verify the occurrence of TGFs globally and not only in the equatorial orbit of AGILE. Although it can also be seen that there is a great predominance of TGFs in the equator.

2.3 Cumulonimbus clouds

The cumulonimbus clouds are clouds of extended vertical development, characterized by the anvil shape at their top and are also associated with high precipitation production. These are local and high instability phenomena, their top usually exceeds 10 km and can reach altitudes of up to 20 km. The formation of these clouds is due to high humidity,

atmospheric instability and rising air currents, and their process is based on three stages: cumulus, maturity and dissipation.

Figure 2, 3 and 4 represent the life cycle of a cumulonimbus cloud.

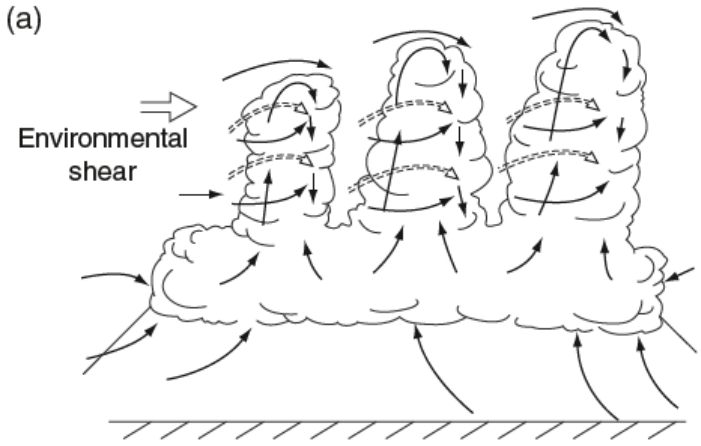

Figure 2: The cumulus stage [40].

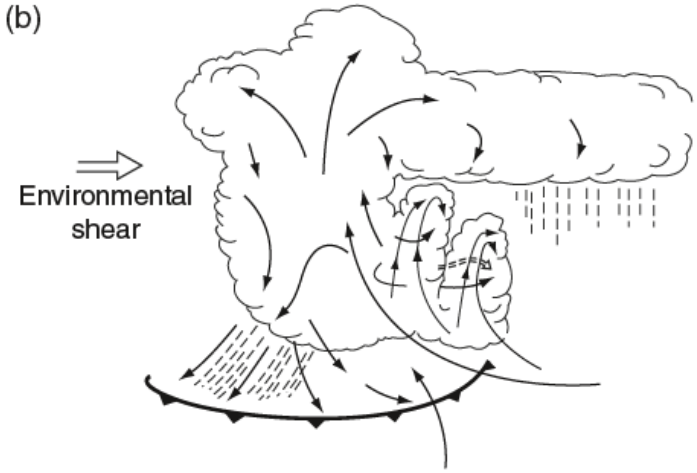

Figure 3: The mature stage [40].

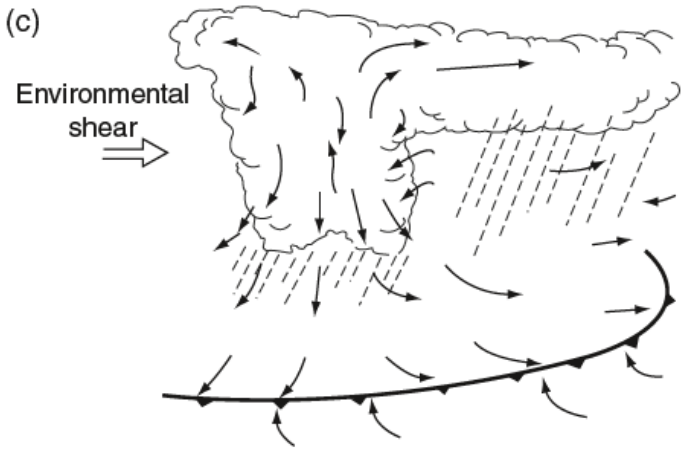

Figure 4: The dissipation stage [40].

In the cumulus phase, the cloud is formed and has its smallest dimension. The movements are upward, forming one or more air towers, and there are also some lateral movements [40]. At maturity there are strong downward drafts and lightning strikes, being the most dangerous phase for aircraft. At this stage there are upward and downward currents of air and rain and the anvil begins to rise at the upper levels of the cloud. Finally, dissipation corresponds to cloud dispersion [29]. There is also a decrease in precipitation, although there are still air currents [40].

There are three different models for storm cloud movement and propagation:

1. Translation: It is a process where the storm moves through the medium wind as it evolves in its shape.

2. Forced propagation: This consists in the regeneration of the storm cloud through an external force mechanism.

3. Auto-propagation: It is based on storm regeneration or in the creation of similar elements, called thunderstorm cells, within the same system.

On average, precipitation and electrical activity of a storm cell has a duration of 30 min. The electric charge is created in a volume with a radius of approximately 2 km and between the temperature range -5 to -40°C. Negative charges cluster between -10 and -20°C and positive charges are kilometers above. After the first precipitation particles appear, charge arises. Although charge creation is related to precipitation, it is known that the charge center is displaced from the precipitation core [40]. When the lightning occurs between the cloud and the ground, the negative branch carries the negative current towards the ground

and is called the leader ray. The electric discharge consists of several rays that move in both directions and this region can reach 30000 K of temperature. Also, 90% of lightning is Intra-Cloud (IC) and 10% is Cloud-to-Ground (CG) [18].

2.3.1 Thunderstorms

Cumulonimbus clouds are characterized by a positive dipole, that is, they have a positive charge over the negative one. In more detail, they can be described in a three-pole structure, in which there is a small region with a positive charge below the dipole. The potential in the dipole varies theoretically from 50 to 500 MV, with the maximum measured voltage being 100 MV. Thus, for a potential of 50 MV, it is possible to accelerate electrons with energies up to 50 MeV, a value within the energy range of the TGFs [18]. The maximum voltage occurs within the cloud rather than at the top, so some of the electromotive force is dissipated inside the cloud. Therefore, the maximum potential (ΔV) values are higher for IC flashes than for CG flashes [37]. As a matter of fact, ΔV_{IC} ranges from dozens of MV to 100 MV and the electric field has a range of values from 50 to 100 kV/m [27].

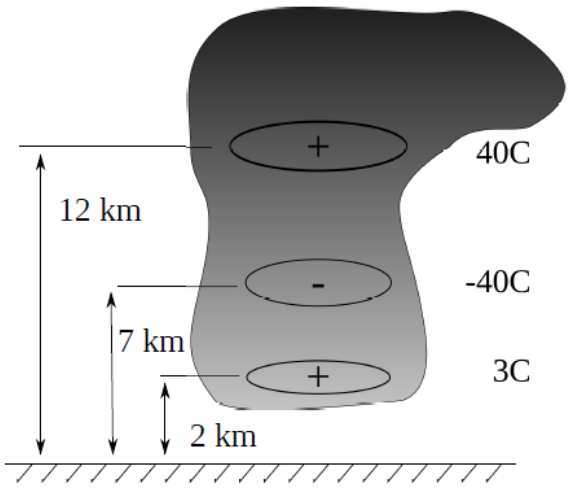

Figure 5: Tripole structure of a cumulonimbus cloud [18].

Cumulonimbus clouds are more frequent in the tropics and mid-latitudes and are often associated with harsh weather conditions. They pose a great risk for aviation, so observing these clouds is quite relevant, such as geostationary satellite imagery, which allow to control and get a forecast of these weather phenomena. Due to the Coriolis effect, where the rotation of the Earth interferes with air movement, aircraft have to shift in a certain direction,

depending on their hemisphere. Thus, when a flight is made in the South Hemisphere, pilots must make left shifts to avoid penetration into the formation. If it is in the North Hemisphere, they shift to the right. When an aircraft enters a cumulonimbus cloud, the aircraft's speed slows due to the immense turbulence. In fact, in these clouds, temperatures are below zero degrees Celsius, with precipitation and formation of ice balls. Turbulence can occur up to a distance of 21 nautical miles (1 nautical mile = 1.853 km) from the center of the cumulonimbus cloud, so the recommended minimum deviation distance is 20 nautical miles from the cloud [29].

Currently exists an Optical Transient Detector (OTD) capable of detecting lightning from space. It consists of a lens system, an array detector and a circuit for converting the electronic output of the system into data that can be analyzed [7]. It was developed by NASA's Marshall Space Flight Center in Huntsville, Alabama, and it was launched on April 1995. This instrument locates all electrical discharges throughout the Earth and has a 70^{o} inclination orbit. However, regions with higher latitude are observed more often than regions with low latitude. Each local observation lasts for 2 min, so 400 data are taken from each region each year, and it is estimated that 1.4 billion flashes occur annually. The average occurrence of lightning is 44 $\pm$ 5 fl/s, where the IC and CG lightning are included [21]. In the North Hemisphere, the annual rate varies between a maximum and a minimum, according to seasons. Thus, it reaches its maximum in summer, 55 fl/s, and its lowest in winter, 35 fl/s [21].

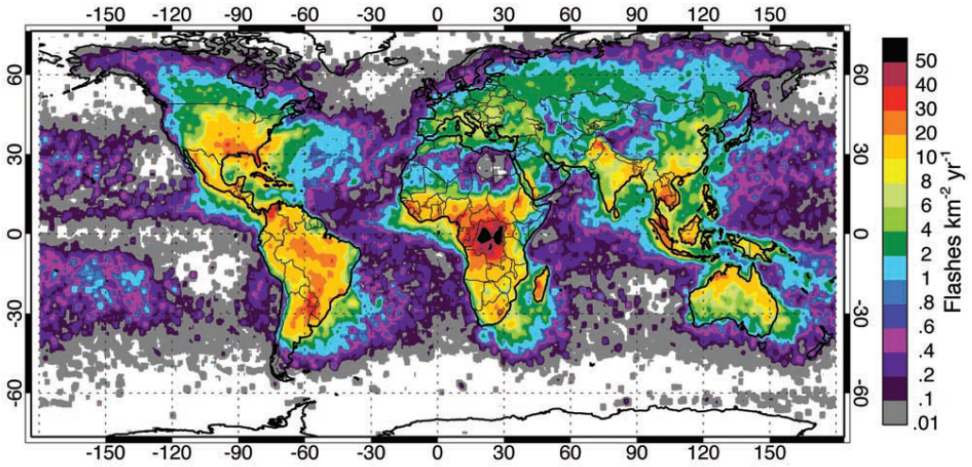

Figure 6: The annualized distribution of total lightning activity (in units of fl km^{-2} yr^{-1}) [21].

Through figure 6 it is possible to verify that the electric discharges occur mainly in the

continental zones, having a continent/ocean ratio of 10:1. However, it is observed that in the North Atlantic zone there is some frequency of lightning, due to the instability of cold air that comes into contact with the warm ocean water. In the Eastern Pacific and Indian Ocean there is not much activity, as the air is warmer [21]. Between the 30°S and 30°N latitudes is where 78% of all lightnings occur. In fact, the annual flash rate variation in tropical zones is very low, only 10% [21].

2.4 Earth atmosphere

2.4.1 Atmosphere layers

The atmosphere is divided into different layers, each with its characteristics. The troposphere is the layer closest to the Earth's surface and here, the temperature decreases with increasing altitude. Thus, at the base of the troposphere, the average temperature is 15°C, while at the top is -60°C. Meteorological phenomena occur practically all in this layer, extending up to 20 km altitude. Then there is the stratosphere, which extends to an altitude of 50 km. Here temperature increases with altitude, since radiation absorption by ozone occurs, ranging from -50 to 10°C. In the mesosphere, the temperature decreases again with altitude, reaching -90°C and 80 km altitude. The penultimate layer of the atmosphere is the thermosphere, reaching an altitude of 500 km. It is a very hot layer, due to solar radiation and the absorption of heat by gases, such as atomic oxygen. Finally, there is the exosphere, the last layer, which is between 500 and 1000 km from the Earth's surface. It is the transition layer to the outside, and the temperature can reach 1000°C.

It is also noted that the density of the atmosphere decreases with altitude, which is the most relevant property for our study. In this sense, the atmosphere model used in this project will be presented in chapter 3.

2.4.2 Cosmic rays in the atmosphere

The radiation coming from outer space interacting with Earth's atmosphere may be very energetic. Cosmic radiation is divided into two categories according to its origin. Thus, there are energetic particles from the sun and galactic cosmic radiation that represents the bulk of the radiation present in the Earth's atmosphere. The cosmic radiation particles are 86% protons, 11% α particles with helium nuclei, 2% electrons and the rest are ionized metals and antimatter particles. Specifically at 35000 feet (10668 m) altitude, there is 55% neutron, 20% electron and positron, 15% proton, 5% photon and 5% muon [19].

Radiation is always characterized by its range and penetrating power. The bigger the energy of the particle, the greater its range in the medium. However, the higher the density of the medium, the smaller the radiation range. Cosmic rays interact with the molecules and the atoms of the atmosphere, creating secondary particles. The radiation that can transfer energy to the irradiated medium is called ionizing radiation and is also a

characteristic of gamma-rays.

2.5 Commercial aircraft

Aviation is an activity with several health risks, namely radiation, vibration, noise, low humidity and hypobarism. This is something that affects not only passengers, but especially aircraft crews. Besides being exposed to TGF particles, aircraft crew members are subjected to cosmic radiation. Aircraft have structures with different characteristics according to the altitude at which they fly and the function they perform. They must also be able to withstand the lightning coming from cumulonimbus clouds, therefore, it is always intended to avoid the interaction of the electric current with the different systems of the aircraft. In fact, when struck by lightning, a large amount of energy is deposited on the aircraft structure. In particular, when striking a structure made of aluminum, electrical power is conducted with great ease [31].

To show a little of the aircraft's composition, it is considered the Boeing 787 "Dreamliner" as an example. This is an aircraft capable of carrying 335 passengers, which composition is 50% composites, 20% aluminium, 15% titanium, 10% steel and 5% other, where composite materials are fiber-reinforced matrix systems [30]. By replacing aluminum with carbon fiber, the weight of the plane is reduced by 10 to 20%, depending on the aircraft's structure and dimensions. Although titanium and carbon fiber are the best components, they are more expensive and harder to produce. Therefore, in order to minimize costs, steel or fiberglass are sometimes used. This way, each part of the aircraft can have different materials, depending also on its function, location, the tensile forces and the exposure to which it is subjected.

With this in mind, any aircraft has a weather radar that allows it to assist pilots in different weather conditions. The operation of the weather radar is based on synchronization between the emitted and received signals and thus becomes similar to the operation of a conventional radar. The display shows a set of colors in ascending order: green (small precipitation), yellow (moderate precipitation), red (heavy precipitation) and magenta (moderate to strong turbulence), according to the severity of the event. The weather radar only gives information about the frontal area of the cloud and is unable to transmit knowledge about its interior. Therefore, the radar should not be used to cross severe phenomena.

It is known that in unprotected components, the total cumulative dose, resulting from radiation interaction, is 30% higher than for shielded components. To obtain this result, simulations were performed, considering an aluminum shield layer with a thickness of 1 cm and energy gamma-rays between 15 and 40 MeV [26]. For that matter, for electronic components, the critical value of the total radiation dose is D_c=5×10^3 rad(Si) (1 rad = 0.01 Sv).

2.5.1 Interactions with the aircraft structure

Following the interaction of the TGFs particles with the aircraft structure components, a secondary flux of particles, now circulating within the aircraft environment, is created. The following study, carried out by *M.Tavani* [26], consists of a set of simulations performed with "for GEometry ANd Tracking" (GEANT4), to measure the interactions of TGFs particles with the aircraft's fuselage and with its electronic devices. The aircraft is considered to be inside the active channel of the TGF, with the active channel being defined as the cylindrical region where the particles can radiate the aircraft. The spectrum used is according to the AGILE data and the irradiation is made along the axis of the aircraft in a direction from the front to the rear.

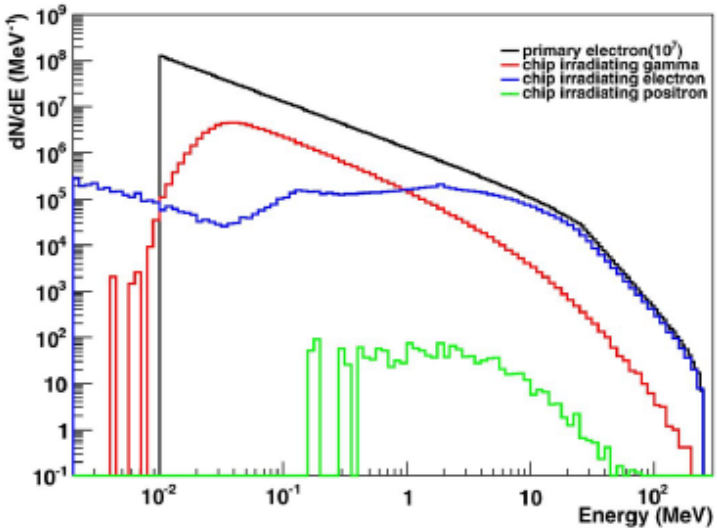

Figure 7: An example of a possible equipment irradiation for an aircraft exposed to a flux of incoming electrons [26].

Figure 7 represents the interaction of the primary and secondary flux of the electromagnetic component, upon reaching an Si electronic device located inside the aircraft with an aluminium shielding layer of $l = 0.5$ cm. The black curve represents the primary flux, while the coloured ones correspond to the resulting flows after the interaction and penetration of the shield layer. The red curve is the gamma radiation, the blue represents the electrons and the green the positrons. As mention above, when TGFs particles interact and react with the aircraft structure, they are divided into two components, the electromagnetic component and the neutron component.

1. The electromagnetic component consists of gamma-rays and electrons/positrons and is the result of the interaction of particle bremsstrahlung, electron/positron pair production, electron/positron and gamma-ray attenuation with the aircraft structure.

2. The neutron component is the result of gamma-rays interaction with the aircraft structure. Specifically, they are produced by gamma-rays with an energy range approximately greater than 15 MeV. The interaction can be represented by the following reaction:

$$\gamma + {}^{27}Al \longrightarrow {}^{27}Al^{*} \longrightarrow {}^{26}Al + n$$

In this case, it is represented the interaction of energetic gamma-rays with aluminum, which is a component of the aircraft's structure. Other similar reactions occur with the remaining elements, such as carbon components:

$$\gamma + {}^{12}C \longrightarrow {}^{12}C^{*} \longrightarrow {}^{11}C + n$$

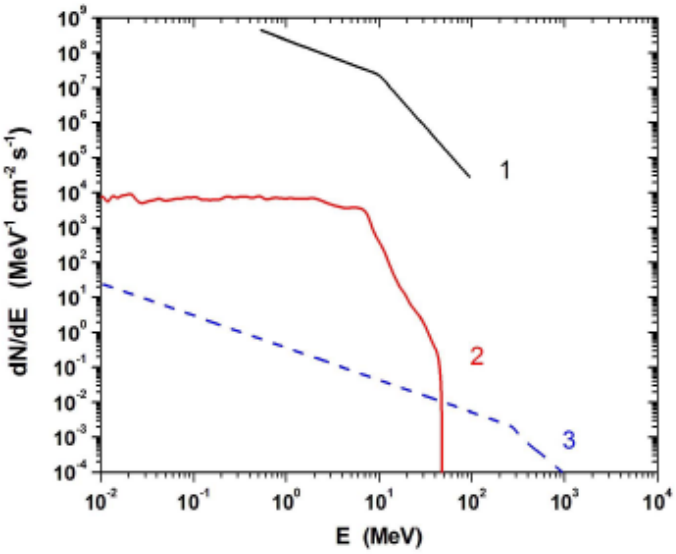

Figure 8: An example of TGF irradiation on aircraft, producing photo-production of secondary neutrons [26].

Figure 8 shows the primary flow spectrum of TGFs, with the black curve. The red curve corresponds to the energy range of the neutrons produced after interaction with the aircraft structure. Finally, the blue dotted line represents the average energy spectrum of neutrons in the atmosphere at an altitude of 12000 m (40000 feet). Upon entering matter, neutrons do not produce ionization directly because they are unloaded particles. However, they transfer energy to other charged particles, which can ionize the medium. Neutrons are very penetrating particles and can be shielded by hydrogen rich materials such as paraffin and water.

Thus, these two side effects create a set of damage to aircraft electronics that fall into four categories.

1. Total Ionizing Dose (TID) effects: They are due to the cumulative effect of ionizing particles, which cause charge entrapment and lead to breakdown of integrated circuits.

2. Displacement Damage (DD) effects: These cause parametric variations as they are originated from cumulative effects of ionizing and non-ionizing particles.

3. Dose Rate (DR) effects: They are produced by intense bursts of ionizing radiation, causing large photo-currents.

4. Single Event Effects (SEE): They occur through the interaction of an ionizing particle with a sensitive region of a device.

As seen above, gamma-rays interact with the aircraft's structure, made up of aluminum and carbon fibers. This interaction results in neutrons, as represented in figure 9. This issue was no longer addressed and no simulations were carried out for neutrons, because it is a much more complex process and for this initial study situation, it is not relevant. Thus, it is purposely considered that this analysis will be for future work.

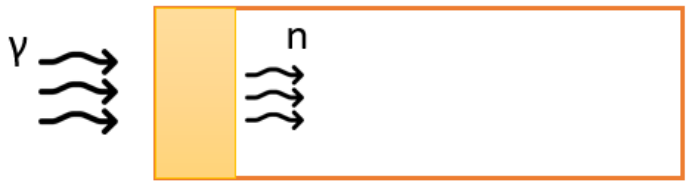

Figure 9: Diagram for the horizontal interaction of gamma radiation with the aluminum layer (yellow) and neutron production.

2.5.2 Commercial aircraft features

Information on the general dimensions of commercial airplanes and respective altitudes are shown in tables 1 and 2. These actual data were obtained through the Transportes Aéreos Portugueses (TAP) and Serviço Açoriano de Transportes Aéreos (SATA) website.

Commercial aircraft	**Flight altitude (km)**	**Passengers**	**Length (m)**	**Height (m)**
Airbus A330	12.5	263/269	58.82	17.39
Airbus A321	11.9	216	44.51	12.09
Airbus A320	11.9	174	37.57	12.14
Airbus A319	12.17	144	33.84	12.17
Embraer 195	12.5	118	38.65	10.55
Embraer 190	12.5	106	36.24	10.55
ATR 72-600	7.62	70	27.16	7.65

Table 1: TAP commercial aircraft [11].

Commercial aircraft	Flight altitude (km)	Passengers	Length (m)	Height (m)
Airbus A321LR neo	11.9	190	44.51	11.70
Airbus A321 neo	11.9	186	44.51	11,70
Airbus A320	10.6	161/165	37.47	11.76
Bombardier Q400	7.62	80	32.83	8.84
Bombardier Q200	7.62	37	22.25	7.49

Table 2: SATA commercial aircraft [9].

2.5.3 Radiation doses

The crew is exposed to various agents, such as radiation, vibration, noise, and low humidity. Depending on the aircraft, the noise varies between 80 to 140 dB, which can lead to hearing loss when the exposure is high. Low humidity also affects the human body, leading to drier skin and loss of moisture in the mucous membranes. It is known that the highest speeds of the aircraft are achieved at higher altitudes, allowing to reduce fuel consumption. This condition has consequences such as low atmospheric pressure, which can generate hypoxia and higher radiation levels. When an individual is exposed to radiation, its effect is determined by taking into account the following factors: dose intensity, exposure time, organ, or tissue that was exposed. The absorbed dose (D) is defined as the average energy deposited by radiation in a volume of mass, whose unit is Gray (Gy) [16].

$$D = E/m \quad Gray(Gy) \tag{1}$$

The equivalent dose (H) considers a radiation weighting factor, W_r. Therefore, the equivalent dose depends on the absorbed dose and the type of radiation. W_r reflects the ability of radiation to cause damage. For gamma-rays, $W_r = 1$.

$$H = D \times W_r \quad Sievert(Sv) \tag{2}$$

The Sievert (Sv) is the unit used to measure the damage caused by radiation, in living beings. The unit of effective dose is Sv and this is the weighted sum of doses for each tissue. According to Decree-Law No. 222/2008 of 17 November, in Portugal, dose limits are divided between exposed workers and the general public. Exposed workers are defined as "people subjected during work, on their account or by others, to exposure arising from practices covered by this decree-law, which may result in a dose higher than any of the dose limits fixed for members of the public" [3]. The effective dose limits are set for exposed workers and the general public, over five-year periods. Therefore, for exposed workers, the value is 100 mSv for five years, and the effective dose cannot exceed 50 mSv per year. For the general public, the effective dose limit is 1 mSv per year. This limit can only

be exceeded, provided that the average effective dose over a period of five years does not exceed 1 mSv per year. In addition, there are also fixed values for three different parts of the human body, which are represented in the table 3 below.

Body Component	**Exposed workers**	**General public**
Crystalline	150 mSv/year	15 mSv/year
Skin	500 mSv/year	50 mSv/year
Extremities	500 mSv/year	Not applicable

Table 3: Equivalent dose limit according to Decree-Law No. 222/2008 of 17 November, Portugal [3], for specific body components.

Also, the National Nuclear Energy Commission (CNEN) states that the world population absorbs 2.6 mGy/year of background radiation. It was found that radiation at cruising altitude, and for domestic flights, is seven to ten times greater than the radiation intensity at ground level. There is still no confirmation on the relationship between radiation at cruising altitudes and the increase in the appearance of cancer in the crew. However, excessive exposure to solar radiation, flight hours, time zones and lifestyle can lead to an increase in health problems. For now, it is known that for doses above 4000 mSv, received in a single time and in a short period can be fatal. Above 100 mSv there is a high probability of leading to the development of cancer [20]. This way, there are some recommendations, such as the use of eye lenses, sunscreens for the skin, and better control of humidity in the cabin.

2.5.4 Questionnaire to the pilot and to the commercial aircraft mechanics

A survey was conducted of two commercial aircraft mechanics and a former executive jet pilot currently flying canadair aircraft. The questions and answers are presented below.

1. **Do aircraft routes change often? If so, how often?**

   Routes are changed as required by the airlines and may always change with each flight. Airplanes have a predefined route, always at a minimum distance of at least one airport, so that in case of total loss of all engines or any other incident, they can always land. Commercial flight routes are organized by air corridors, which remain constant and guided by international airspace organizations. Airplanes, depending on their altitude and type of flight, are controlled along their route by different air traffic controllers.

   A commercial aircraft flies at around 30000 feet (9.144 km), while a business jet travels at 40000 feet (12.192 km) and can use directly air corridors, from departure

to destination, as they are the aircraft that move higher. Of course, flight conditions will always depend on the weather of the atmosphere, and a jet plane may have to lower its altitude. Jet aircraft can reach the maximum possible altitude due to their cabin pressurization as it is smaller and takes fewer individuals. In contrast, a commercial flight has to move at 30000 feet, because it supports the crew and a large number of passengers, taking into account the atmospheric pressure of the cabin.

2. **What is the limit of hours a pilot can fly an aircraft? For example, what is the limit of hours per week or per month?**

   The pilot Luís Santos does between 85 to 90 hours/month on flights. In addition, the Flight Duty Period (FDP), is from 11 hours and 30 minutes to 12 hours a day, however, this time is not always spent on flights. In fact, the time spent checking the plane or in service, even waiting for the next flight, also counts for its service time, never exceeding the daily FDP. It depends on the type of the flight and the aircraft.

3. **Does an aircraft has a weather radar? Or how can pilots detect storm clouds? How accurate is the device?**

   All aircraft have a weather radar, the accuracy of which depends on the device model and brand. A wave is emitted and reflected by the clouds and atmosphere, and a specific zone is indicated on the device: green, if it's mostly water vapor; yellow if it's a cloud of greater development; red for a very aggressive and violent storm from a meteorological point of view.

4. **When or under what conditions can an aircraft cross a storm cloud?**

   Pilots avoid crossing cumulonimbus clouds, because they are places of great violence for the aircraft. There are side-by-side upward and downward layers of air that can create very large tensile forces, for example breaking the aircraft wing. The temperatures in these clouds are varied, reaching the -40ºC and -50ºC, due to their large extent.

5. **When an aircraft deviates from a storm, what is the limit distance? How far can the pilot get off the route?**

   Usually, a pilot always tries to get around the storm cloud on the right or left side. This is because cumulonimbus clouds are clouds too high to fly over, causing a lot of fuel loss. A pilot always evaluates the maximum altitude that the fuel allows him, because he may have to go back and land, wait for the storm to dissolve and then resume the flight. In fact, an aircraft is always supplied with enough fuel for its route and for a few more km it may have to fly in case of an emergency.

6. **When an aircraft deviates from a storm cloud, does the pilot choose to fly over or bypass it?**

Generally, cumulonimbus clouds are bypassed as described above. However, passing over the cloud may occur.

7. **Do aircraft have a "shield" for radiation in the atmosphere? If so, how does it work?**

   The existence of such a shield is unknown to pilots and mechanics.

8. **How can radiation affect aircraft electronics during the flight?**

   From an electronic point of view, the pilots and mechanics are uninformed. However, for the human body at 30000 feet, the humidification of the air is different, even controlling the atmospheric pressure of the cabin. The pilot Luís Santos hopes that there will soon exist a device that detects how much radiation has been absorbed during the flight. He also reported that during his flights at 40000 feet, he always wear long sleeves, sunglasses and a hat. It is simply a precaution that he takes, especially to protect himself from solar radiation. It is also known that, for every aircraft, the cockpit glass has some protection from solar radiation.

9. **After a flight, are measurements made of the radiation that was absorbed by the aircraft? Or is there any mechanism that does something similar or that controls the absorbed radiation?**

   Pilots and mechanics are unaware of any radiation-related caution or safety.

3 Chapter 3: TGF and Aircraft Irradiation Simulation

In this chapter, the simulation tools used and the respective characteristics are going to be presented. It will be indicated the reason for its use, its limitations, and its advantages. Then, the entire procedure to simulate TGF emissions in the atmosphere, as well as how these emissions may irradiate a commercial aircraft will be presented, in particular the discussion about the methodology and the results relative to the different simulation sets.

3.1 Techniques and simulation tools: Software framing

On average, air traffic doubles over 15-year cycles, so constant monitoring of routes is very important. Currently, the most widely used calculation programs for radiation exposure control are:

1. **EPCARD:** The European Program Package for the Calculation of Aviation Route Doses (EPCARD) is a software program that allows to simulate the dose of cosmic radiation to which any aviation route is exposed, between altitudes of 5 and 25 km. It was produced by the Institute of Radiation Protection of the Helmholtz Zentrum München and with the help from the European Commission and University of Siegen, Germany [4].

2. **CARI:** The Care and Resilience Index (CARI) consists of a set of carefully asked questions that measure mental health, well-being and emotional involvement. The analysis of the answers and their comparison allows a correct evaluation of the performance and improvement of the person's health [1].

3. **PC-AIRE:** The Predictive Code for AIrCrew Radiation Exposure (PC-AIRE) is a model for calculating radiation exposure from commercial, private and military flights, at any time in the solar cycle. It is one of the largest flight control database [8].

4. **SIEVERT:** This model also allows to calculate the radiation dose absorbed for any type of flight [10].

5. **GEANT4:** It is a model for particle transport simulation and interaction with matter. Its applications fall into high energy programs, nuclear physics, medical physics and space physics [6].

3.1.1 MEGALib versus GEANT4

The two most suitable software for carrying out TGF aircraft irradiation simulations are GEANT4 and MEGALib. These two programs simulate the interaction of particles

with matter and their path through matter and are used for studies of medical physics, nuclear physics, and space studies, with high energies. Both provide the study with various types of particles, such as electrons, protons, neutrons, gamma-rays, and more. Physical processes include electromagnetic, hadronic, transportation, decay, optical, and parameterization processes. The distribution of the energies spectrum is also obtained in a similar way, through mono-energetic, linear, exponential, power-law, Gaussian, bremsstrahlung, or blackbody beams.

Finally, for our study, MEGALib was chosen, as it is the one that presents a programming language that is more accessible and faster to learn. Although there is already a lot of information and many examples of projects with GEANT4, this is in C ++ language, being more complex than MEGALib. Furthermore, the MEGALib version (version 2.32) used in this research work is based on GEANT4 physics' libraries. The properties of MEGALib will be described below.

3.1.2 MobaXterm

MobaXterm is a Windows Unix terminal, allowing remote access to the server. Gives access to Unix / Linux, on a Windows system, facilitating simultaneous use between operating systems. Through MobaXterm is possible to carry out the communication between client and server. It is an encryption system, which automatically generates public-private key pairs to encrypt a network connection. In other words, the public-private key pair ensures that the information is not altered and that it comes from the expected client. The cryptographic network protocol used is the Secure Socket Shell (SSH), which authenticates the remote computer and the user. This way, the connection was established, connecting the client to the "fermi" machine of the LIP Lisbon servers. Finally, access to the MEGALib program is done through MobaXterm and all simulations will be performed here.

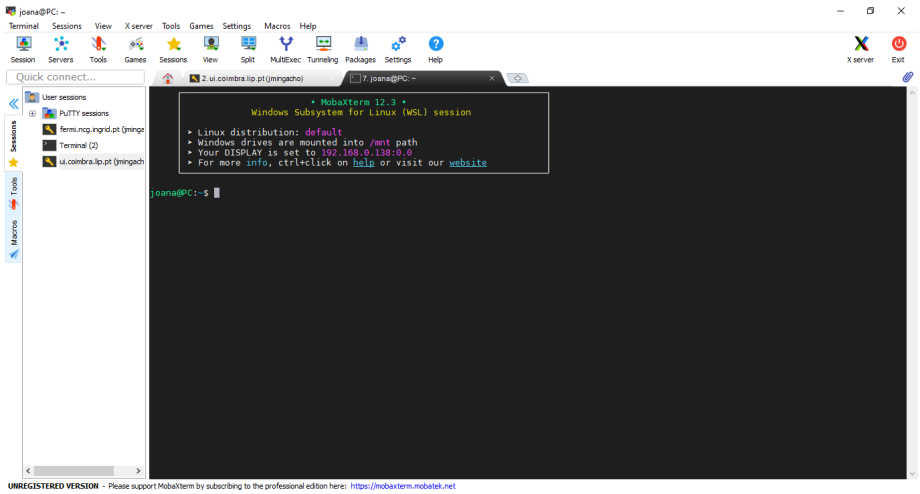

Figure 10: MobaXterm graphical interface.

3.1.3 MEGALib: The Medium-Energy Gamma-ray Astronomy library

MEGALib is a software library for the purpose of simulating and analyzing data, building geometries, imagery, Monte Carlo simulations and event reconstruction. This is a tool written in C ++, which was initially devoted to Compton telescopes and low-energy pairs, but later covered different X-ray and gamma-ray telescopes. This software consists of the following components:

1. **Geomega:** Geometry and detector description: This allows to create geometry and provide information about the volume, the material and the detector used.

2. **Cosima:** Geant4 based simulation: This component is intended to predict the detector response to gamma-ray or high energy particle interactions. Through the Geomega library, Cosima accesses the detector geometry and performs the simulations.

3. **Sivan:** Interpreting simulations: The "Simulated event analysis" interprets all information from the simulation output and links the simulation to the final answer.

4. **Revan:** Event reconstruction: The "Real event analyzer" allows to reconstruct events and to identify the initial interaction process.

5. **Mimrec:** High level data analysis and image reconstruction: It allows the reconstruction of the MegaLib image, by selecting events and evaluating parameters, and reverses the measurement task.

3.2 Methodology

As seen above, Cosima allows to simulate different measurement scenarios. Through simulations, it is possible to model the profile of a TGF emission in a range of energies from keV up to hundreds of GeV. Photons with greater energy, which escape the atmosphere, suffer little interaction with the atmosphere, and are able to reach the satellite detectors. TGFs that reach the satellite altitude with low energy, are actually TGFs with high energy initially, which have suffered interactions through their path in the atmosphere. The lower energy photons are subject to Compton dispersion, constantly changing their direction and decreasing their energy. They also have a longer path compared to TGFs that suffer less from Compton dispersion. Considering all these scenarios and interactions, simulations will be performed through MEGALib. Through Revan MEGALib tool, it is possible to obtain the statistics of the triggered photons and the energy spectrum of the TGF emission in the atmosphere or in an aircraft material. For the reconstitution of the events, it is necessary to initialize Revan with the desired geometry and with the configuration file, this is,".cfg" file, resulting from the Revan configuration. The output of this reconstruction generates a ".tra" file, which should be used for more detailed analysis in Mimrec. So, although Mimrec is not going to be used much, it also allows the analysis of the energy spectrum. Finally, the cumulonimbus cloud, aircraft and TGF emission data to be modeled are represented in the following tables 4, 5, and 6.

TGF Project Data	**Simulations**
Vertical development; Bottom-up formation in the atmosphere; The life cycle goes through three consecutive states, lasting from 20 to 180 min; In the last state: Average diameter $\sim$ 10 km Cloud base diameter $\sim$ 1 to 4 km Top diameter $\sim$ 8 to 20 km	Cloud model 1- Simple conical geometry 2- Approximate geometry with 3 conical volumes
Cloud up to 23 km in altitude, most commonly the top being at 10 km; Cloud top temperature $\sim$ -40^{o}C; Latitudes greater than 45^{o} - the top of storm clouds rarely exceeds 8 km in height; Latitudes less than 45^{o} - the top usually exceeds 10 km and can reach altitudes of up to 20 km	Modeling atmosphere and air density gradient (in MEGALib)

Table 4: Cumulonimbus clouds characteristics.

TGF Project Data	**Simulations**
Velocity: 750 to 800 km/h Average altitude of flight: 10 km high Safety distance: - 5000 ft (1524 m) vertical separation; - 20 mile (32186.88 m) lateral separation	Aircraft position/distance modeling from the cloud
Fuselage: - Aluminum alloy with anti-corrosion treatment; - Composites; - In limited quantities, magnesium and stainless steel are also used	Aircraft modeling and materials that may eventually shield the cabin or contribute to diffusion phenomena

Table 5: Aircraft characteristics.

TGF Project Data	Simulations
Tropical storms tend to generate the most TGFs; TGFs are associated with a storm strengthening phase	Modeling photon emission and neutrons or other particles, during TGF emissions
Energy: 100 keV to 100 MeV; Associated with individual lightning strikes; Cone shaped with 30^o to 40^o opening; Duration: 50 μs to 1 ms; Ratio between TGFs and the remaining radiation(in the tropics): $\sim 10^4$; Neutron emission of a few ms; Typical energy $\sim$ 7 MeV; Average number of accelerated electrons: 10^{17} to 10^{18}; TGFs occur on average once in a storm	- Energy profile; - Position and emission geometry

Table 6: TGF emissions characteristics.

3.3 Atmosphere composition overview and model creation for the composition

The Earth's atmosphere mass is about 5.1×10^{18} kg and its most abundant constituents are: Nitrogen (N_2) with 78.08 % fraction by volume in air (total atmosphere); Oxygen (O_2) with 20.95 %; Argon (Ar) with 0.934 %; Carbon dioxide (CO_2) with 353 ppmv (ppmv = 10^{-6}); and Helium (He) with 5.24 ppmv. The water vapor in the atmosphere has a very variable amount, but on average it is about 1% of all air. The remaining components of the atmosphere have very small amounts, which will not be presented here, as it is considered that they are not relevant to our model. As already mentioned above, the density of the atmosphere decreases with altitude. This variation can be confirmed through the table 11. However, for a better observation of the density behavior, the data in the table 11 were represented in the graph 12.

Altitude, km	Column Density, g/cm^2
10	270
15	129
20	62
30	14
40	3.2
50	0.74
60	0.17

Figure 11: Atmospheric density for different altitudes [18].

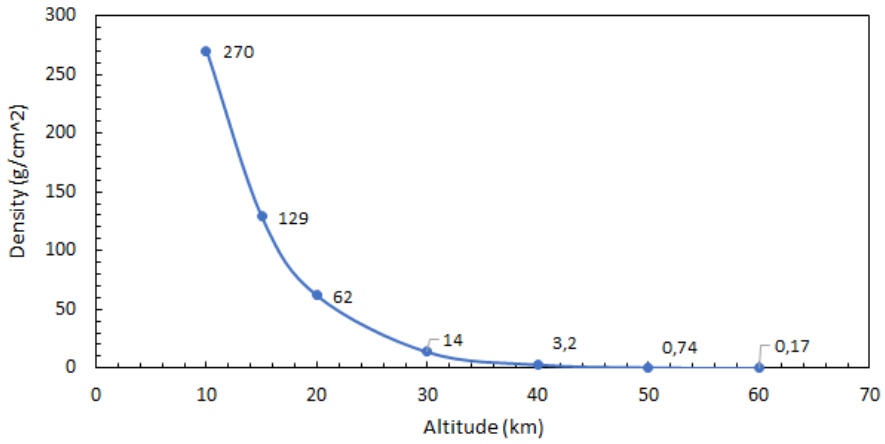

Figure 12: Representation of the atmospheric density for different altitudes [18].

To achieve a better approximation of the atmosphere components, as well as of the mass density, the creation of a model data file in American Standard Code for Information Interchange (ASCII) format was used. Thus, the website of the "Community Coordinated Modeling Center" [2] was used, whose page allows to obtain the values and graphs of a set of parameters of the atmosphere, namely: neutral temperature, exospheric temperature, densities of helium (He), atomic oxygen (O), nitrogen (N_2), oxygen (O_2), argon (Ar), atomic hydrogen (H), atomic nitrogen (N), and total mass density. The inputs are placed to describe the conditions that the user wants to simulate. Our objective was to obtain a model that describes the general and most basic conditions of the atmosphere as a function of altitude and in this sense, our inputs are described in the following table 7.

Parameter	**Value/Amount**
Date	Last allowed date: 2020/02/15
Time	Universal
Hour of day	12
Coordinates Type	Geographic
Latitude(deg.,from -90. to 90.)	0
Longitude(deg.,from 0. to 360.)	0
Height (km, from 0. to 1000.)	1000
Profile type:	Height (km, from 0. to 1000.) Start: 0 Stop : 1000 Stepsize: 1

Table 7: Initial parameters used [2].

Then, the desired format for the output is selected and thus, a ".txt" file with the characteristics of the atmosphere is obtained, according to the scenario chosen initially. The obtained ".txt" file contains all the properties of the atmosphere (neutral temperature, exospheric temperature, densities of He, O, N_2, O_2, Ar, H, N, and total mass density) as a function of altitude (km). This way, it is possible to analyze each km of altitude individually, but also generate graphs that express the behavior of each property. The properties that we are going to use in this project are the densities of He, O, N_2, O_2, Ar, H, N, and total mass density, and are the ones that will be represented next.

In other notes, although the cumulonimbus cloud model has been described, this approximation has not been performed, since the components of the atmosphere have been approached at certain altitudes. Since it is possible to create the desired atmospheric environment through MEGALib, the cone-shaped geometric approximation of the cumulonimbus cloud was not made.

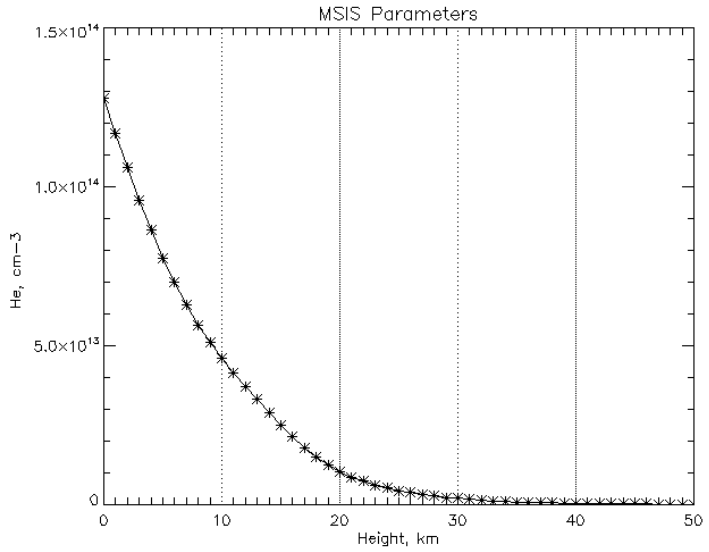

Figure 13: He, cm^{-3}, as a function of the altitude (km) [2].

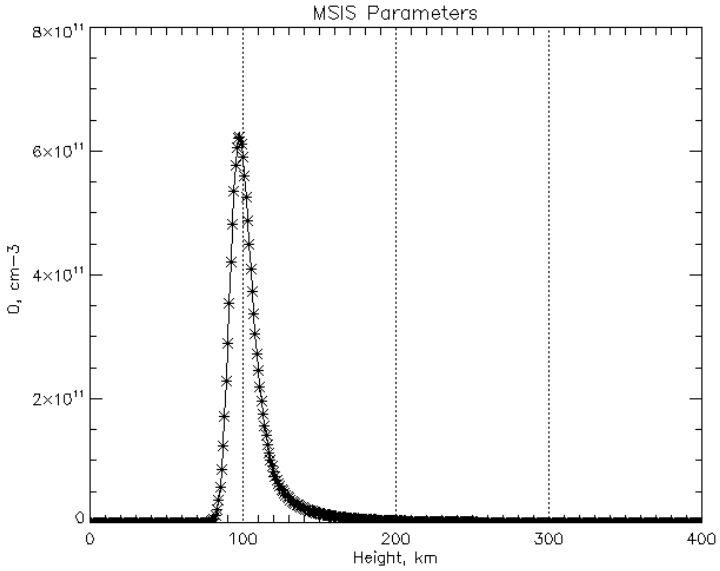

Figure 14: O, cm^{-3}, as a function of the altitude (km) [2].

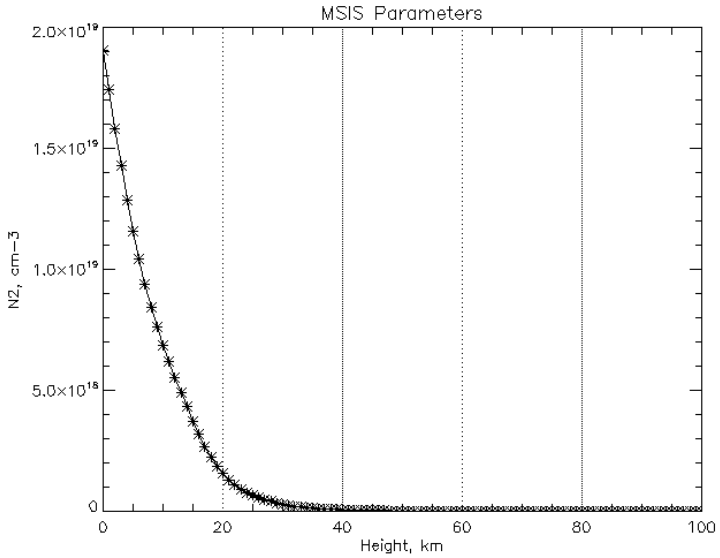

Figure 15: Nitrogen (N_2), cm^{-3}, as a function of the altitude (km) [2].

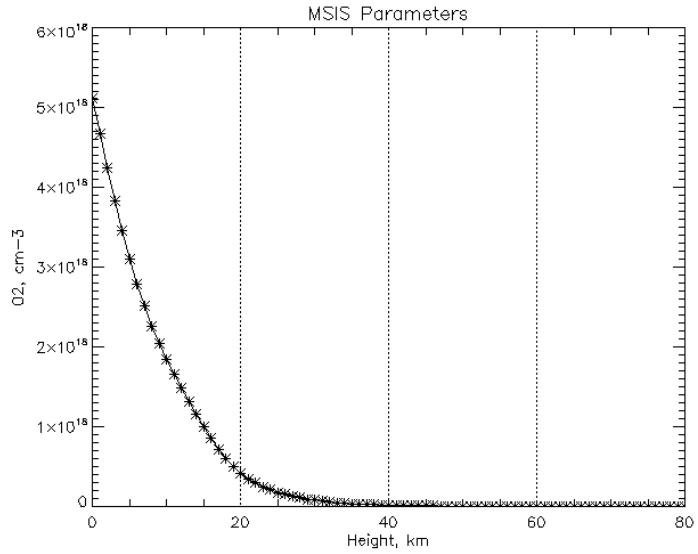

Figure 16: Oxygen (O_2), cm^{-3}, as a function of the altitude (km) [2].

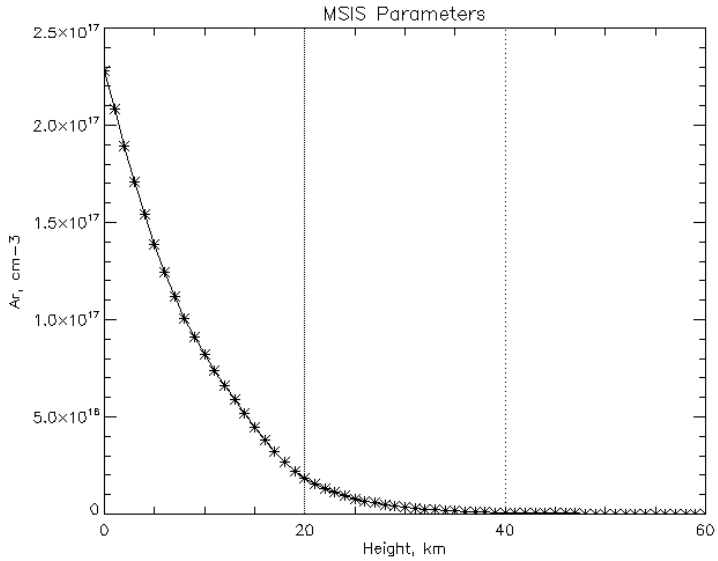

Figure 17: Argon, cm^{-3}, as a function of the altitude (km) [2].

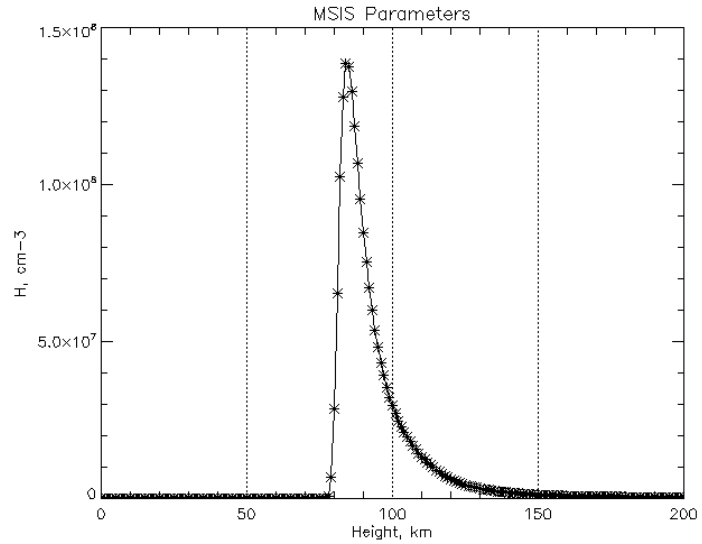

Figure 18: Hydrogen, cm^{-3}, as a function of the altitude (km) [2].

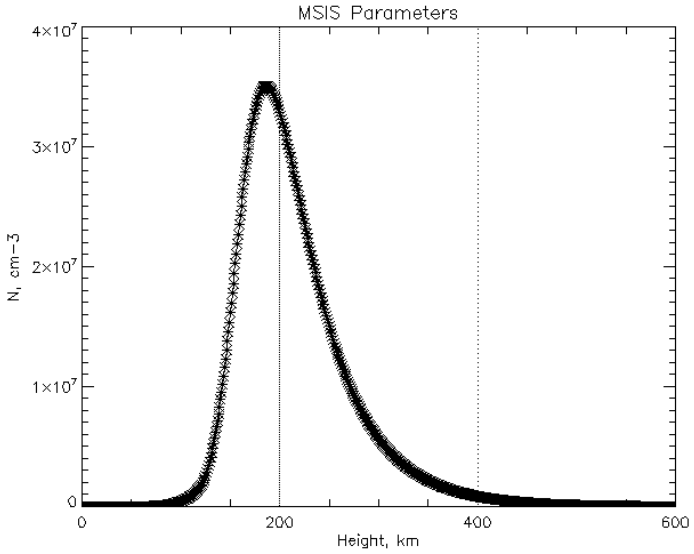

Figure 19: Nitrogen, cm^{-3}, as a function of the altitude (km) [2].

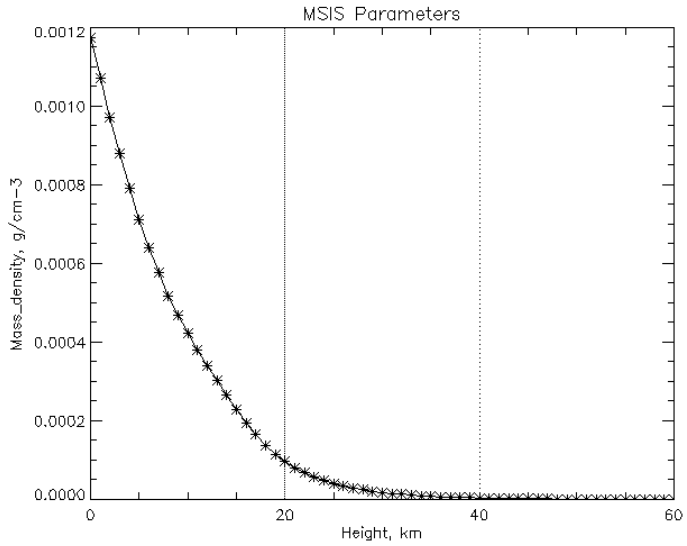

Figure 20: Mass density, g/cm^{-3}, as a function of the altitude (km) [2].

Considering the eight graphs presented, it is possible to draw some conclusions. First, the molecular components, namely N_2 and O_2, have very similar curves, where its density

decreases with altitude in the atmosphere. It is also observed that for 40 km of altitude, both concentrations are 0 cm^{-3}. Subsequently and analyzing the atomic components, it is concluded that He and Ar decrease with altitude, unlike N, H, and O, which present a different behavior. For H and O there is a peak of concentration at 100 km altitude, while N has a peak at 200 km high. This is due to the fact that for these much higher altitudes, the molecular components cease to exist and start to inhabit the atomic components. Finally, graph 20 corroborates again the decrease in density as a function of altitude, as can be seen in table 11 and the respective graphical representation.

All points of the graphs are well known and are presented in the output ".txt" file, making it very easy to obtain the atmospheric density and abundance of components, for each altitude. In this sense, each simulation will be performed at altitude z, so the environment will be the atmosphere at altitude z. In a more advanced and complex phase of the simulations, the atmosphere will be represented between two altitudes, for example, through an average between the values. This allows a good approximation of how the particles interact considering a range of altitude values. These simulations will be presented later and this average will be duly mentioned.

3.4 Simulation methodology

In order to build the aircraft TGF irradiation simulation code, by evaluating the potential effects of radiation on passengers and crews of commercial flights, we started by building the simulation model geometry. That is, the geometry of the irradiated volumes (atmosphere, aircraft materials, humans, etc.) and its respective position. The second simulation code entry was the source, the photon emission characteristics and irradiation configuration. Finally, the detection trigger conditions were set as well as the simulation stopping instructions.

The first set of simulations has the main objective to calibrate the simulation code by calculating the efficiency of a simple CdTe detector model, when irradiated in the 100 keV - 1 MeV energy band, and by comparing the obtained results with previous validated experimental and simulated results with a CdTe detector in the same irradiation conditions. After the calibration, a simple aircraft size model will be considered when irradiated by monochromatic beams. According to the data obtained, the airplane model will be built increasingly complex, namely adding aluminum fuselage. Then, the source model will be made increasingly complex as well, in order to simulate as close as possible the actual TGF emissions, i. e., it will assign a power-law distribution and a cone-shaped emission beam. In the final phase of the simulations, an estimated real flow will be used, to approximate emissions to the most real case possible. An approximation of the atmosphere composition for the different altitudes used will be obtained. A human being simulation model will be built, in which a cylindrical approximation of a human body will be created. For the human body, the most correct material to use and which is also the most approximate is the phantom. The entire process and model used will be defined later. Also, the performance

of a simple CdTe TGF monitor inboard the aircraft will be simulated and analysed.

Finally, a simulations section for a satellite altitude will be presented, to validate our simulation methodology. This is because the fluency data of the satellites are known, and the values of the simulations allow us to correct and verify the models used, by calculating the fluency for those satellite altitudes.

The simulations are a set of data/counts obtained over a time interval. Note that there is no error associated with MEGALib models, i. e., there is no systematic error in the program. Thus, the uncertainty associated with this direct count will be the square root of the counts, this is, for each N value, there is an uncertainty of $\sqrt{N}$, being the best estimate for the deviation from the true value.

3.4.1 Calibration with CdTe Cubic detector model

As mentioned earlier, the simulation plan started by validating our code with previous published results, experimental and simulated [33] [34], by comparing the detection efficiency of a CdTe cubic detector model within the same energy range (100 keV up to 1 MeV) and for the same detector type and thickness (10 mm). The published data resulted from GEANT4 home made code simulating a CdTe matrix of about 700 cm^2 and 10 mm thickness as well as experimental results obtained under a gamma-ray of the Eurpean Synchrotron Radiation Facility in Grenoble, France.

Source features:

For a source to be defined, at least one type of particle, a beam, a spectrum and an average total flow is required. Here we will use a gamma-ray source, $ID = 1$ according to the Cosima manual, with a homogeneous and mono-energetic beam in keV. In this initial phase, the flux is set to 50 particles per second, not influencing the number of photons that reach the cubic detector. The beam has a radius of 0.2 cm and is located at a distance d from the detector, as shown in the diagram below, figure 21. The source will emit 100000 photons towards the detector, which will be used as a simulation termination factor, i. e. the simulation in MEGALib ends after the 100000 photons are shot.

Detector features:

The geometry file includes, in a basic and general way, the detector volume, the detector type and its characteristics, the list of materials, and the trigger criteria. The bill of materials can be included here as a file. Geomega has several types of detectors, each with different parameters and ways of being represented and, in this case, the detector is defined as a *Simple detector*. For this, the first scenario is a cubic detector, a 10 mm edge, consisting of CdTe (Cadmium Telluride). The center of the detector is at position (0,0,0) and the source is 10 cm away, placed on the x-axis in the Cartesian framework. As the flow is 4 mm in diameter, it is possible to verify that the beam does not overlap with

the dimensions of the cubic detector. This is a very important aspect, since the 100000 photons should be emitted within the detector's limits. For the simulation to occur it is necessary to consider a *WorldVolume* and here *Material Air*, defined by MEGALib, was used for the surrounding material. *WorldVolume* must be large enough to allow both the geometry of the detector and the source to be in this volume.

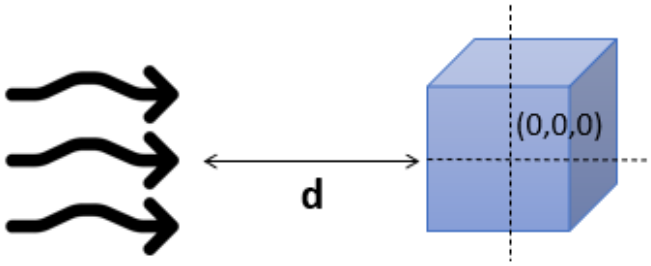

Figure 21: Diagram for the simple model of the cubic detector.

Cubic Detector Simulation

Nine simulations were carried out, each with a homogeneous and mono-energetic beam for the following energies: 200, 300, 400, 500, 600, 700, 800, 900, and 1000 keV. Running Cosima and later Revan, in trigger statistics, the *Number of triggered events* is obtained. Dividing this value by the *Total number of particles generated*, the values of the efficiency of the detector in percentage are obtained, described in table 8. The corresponding graph allows better observation of the variation in efficiency as a function of energy. As the vertical error bars have approximately the same amplitude as the dimensions of the dots represented in the graphs, it was decided not to show this error bars. The same happens in the following simulations, where the errors always remain in the same order of magnitude and are always represented in the respective tables.

Energy (keV)	Triggered/Beamphotons	Efficiency (%)
200	82329	82.329 ±0.287
300	58591	58.591 ±0.242
400	46379	46.379 ±0.215
500	40085	40.085 ±0.200
600	36499	36.499 ±0.191
700	33326	33.326 ±0.183
800	31329	31.329 ±0.177
900	29337	29.337 ±0.171
1000	28161	28.161 ±0.168

Table 8: Source with 4 mm beam at 10 cm from the cubic detector; Material: Air.

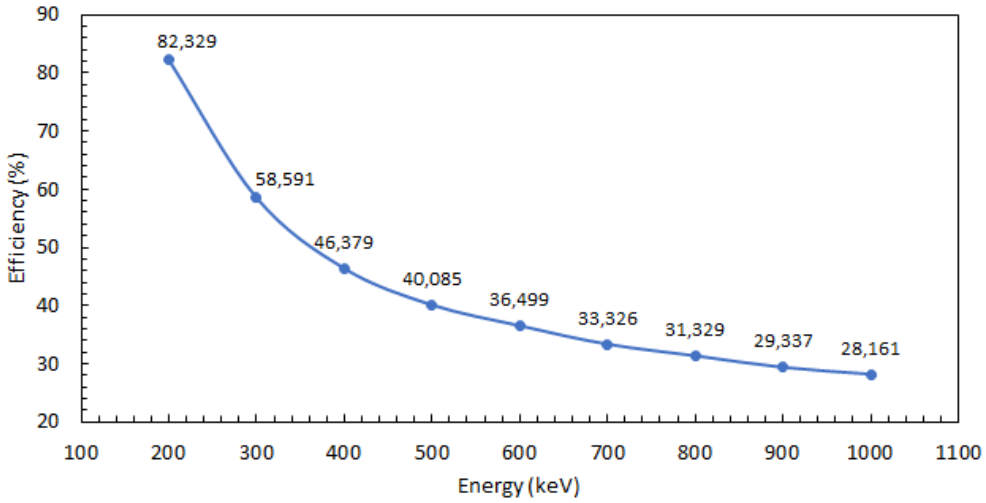

Figure 22: Efficiency (%) for the CdTe cubic detector as a function of energy (keV).

The graph in figure 22 is in agreement with the graph in figure 23 (triangles curve) that represents the efficiency for the Coded Imager and Polarimeter for High Energy Radiation (CIPHER) telescope, for the same energy range, obtained with a GEANT4 simulation code that was validated in several experimental tests for the same type of detector and the same energy range.

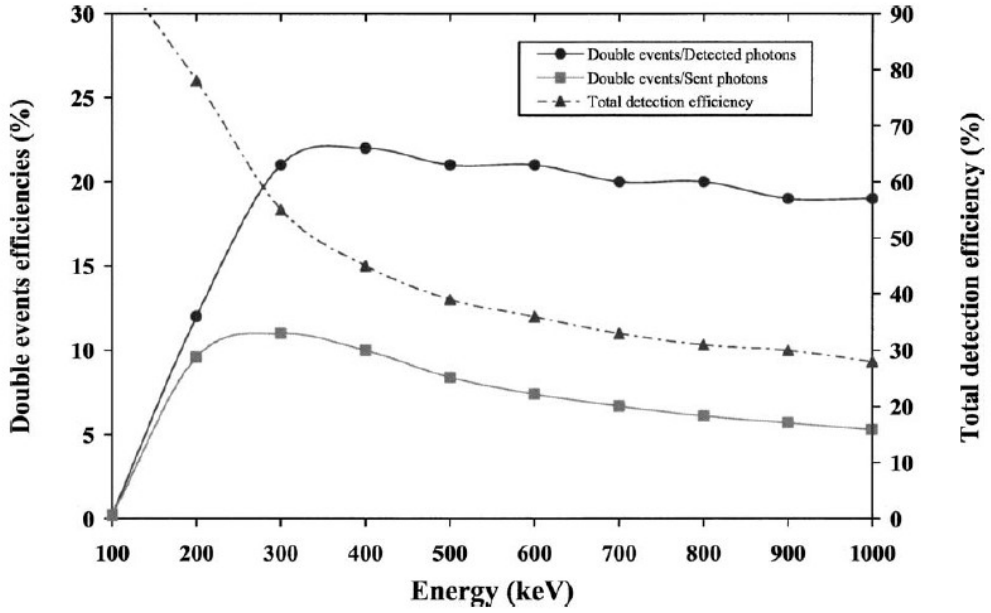

Figure 23: CIPHER detection plane efficiency (%) (triangles curve) as a function of energy (keV), simulated with GEANT4 [34] [33].

The CIPHER is an X-ray and flexible-ray polarized spectroscopic and polarimetric coded mask telescope based on cadmium telluride microspectrometers. It consists of a 10 mm thick CdTe detector, as our cubic detector. However, CIPHER was simulated for a 700 cm^2 of a total effective area, therefore a slight better efficiency was obtained due to Compton events with scattering angles near 90^o that are better collected within a larger detector, for the same thickness. Its energy range is from 10 keV to 1 MeV. So it turns out that our model of the cubic detector is correct since both curves have the same shape and very close values for each energy.

It was decided to use a CdTe detector as a TGF monitor, since these detectors are suitable for spectroscopy and imaging for gamma-ray emission sources (0.1 MeV to $\sim$ 5 MeV). CdTe detectors can monitor gamma-ray emissions due to its high resistivity ($\sim$ 109 Ω.cm) and gap energy ($\sim$ 1.44 eV) that allows low leakage current and operation at room temperature. Its high average atomic number (Cd: 48; Te: 52) and high density (5.85 g/cm^3) offer the advantage of an excellent efficiency of detection of gamma-rays up to some MeV when compared to other semiconductor detectors, such as Ge (Z = 32) and Si (Z = 14). It is a compact, high-efficiency gamma-ray detector that can fit in small volumes in an airplane cabin or cockpit. A CdTe monitor can operate with low complexity and low power electronic system. A polarization voltage of about 100 V is provided by

a low power DC/DC converter that can be powered by a normal cabin or cockpit plug. The CdTe detectors are robust, provide good energy resolution (< 5% at 100 keV) and time resolution (<10 μs), and an operational range superposed with the most intense flux section of the TGF emission spectrum profile.

3.4.2 Aircraft Primary Model Simulation Set

After calibration, a set of simulations was performed with a simple CdTe cylinder of the size of an aircraft, allowing to step to a model closer to a more realistic aircraft model, making sure that in this next step we can cross check the data with cubic model calibration and we can verify that our final TGF aircraft irradiation performs correctly under different atmosphere flight altitudes and densities. Although the dimension of the CdTe aircraft is much larger than the cubic detector used above, it is considered that this is the best approximation and verification of the values, since the material remains constant and the only difference are the dimensions of the aircraft model. The aircraft primary model was then irradiated for a representative monochromatic beam of 300 keV at different distances between the source and the aircraft primary model for Air at 1 atm, for Air density at 10 km altitude and vacuum. This set of simulations will allow to validate the simulation model by verifying if the gamma-ray beam absorption trends in air as a function of air density, of altitude and of air thickness between the source and the aircraft model, follow the expected absorption rates.

Source features:

The beam is 10 mm in diameter and has a constant energy of 300 keV (photon energy within the TGF emission range and inside the CIPHER efficiency analysis energy range), for the following distances from the outer surface of the cylinder: 1, 5, 10, 20, 50, 100, 200, 500 and 1000 m. The stop factor remains the 100000 events, that is, the beam will emit 100000 photons as in the simulation above. The flow is maintained at 50 photons per second, therefore, in this case, the only factor that changes is the distance from the source to the aircraft. The source is on the same plane, horizontal plane, as the aircraft. For the simulations, it will be considered that the TGFs behave as individual pulses.

Aircraft Primary Model features:

In this scenario, was built a shaped cylinder model, which is considered to be the geometric shape that best fits the approximate shape of an aircraft. The material of this aircraft model is CdTe. For the geometric shape and size of this model, the dimensions of the Airbus A380 were considered, which is 72.72 m long and 24.1 m high. This way, the cylinder is 72 m long and 12 m in radius. The Airbus A380 was chosen, since it is the largest commercial airplane that exists, having a flight altitude of 10700 m. Then, the largest real dimensions that exist for a commercial airplane are considered in our model. So

for smaller aircraft, the simulation's behavior is expected to remain similar. The aircraft model will retain its geometric shape and size for all subsequent simulations.

Finally, the aircraft primary model is in position (0,0,0) and the source is at a distance d from it, as shown in the diagram, figure 24.

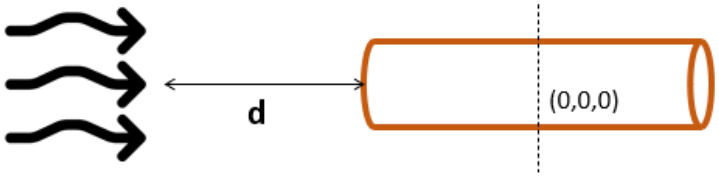

Figure 24: Diagram for a beam hitting the aircraft primary model.

Simulation

The surrounding material between the source and the aircraft primary model is the *Material Air* defined by MEGALib, corresponding to the atmosphere at sea level, 101.325 kPa and 20°C, with a density of 1.2041^{-3} g/cm^{-3}, according to the MEGALib tool kit created by Andreas Zoglauer. From table 9, the following graph 25 is obtained.

Distance (m)	**Triggered/Beamphotons**	**Efficiency (%)**
1	100000	100.000 ±0.316
5	100000	100.000 ±0.316
10	100000	100.000 ±0.316
20	95166	95.166 ±0.308
50	71918	71.918 ±0.268
100	41385	41.385 ±0.203
200	12601	12.601 ±0.112
500	345	0.345 ±0.019
1000	1	0.001 ±0.001

Table 9: Source with a beam of 10 mm in diameter, with constant energy of 300 keV and at a distance d from the aircraft primary model; Material: Air at 1 atm.

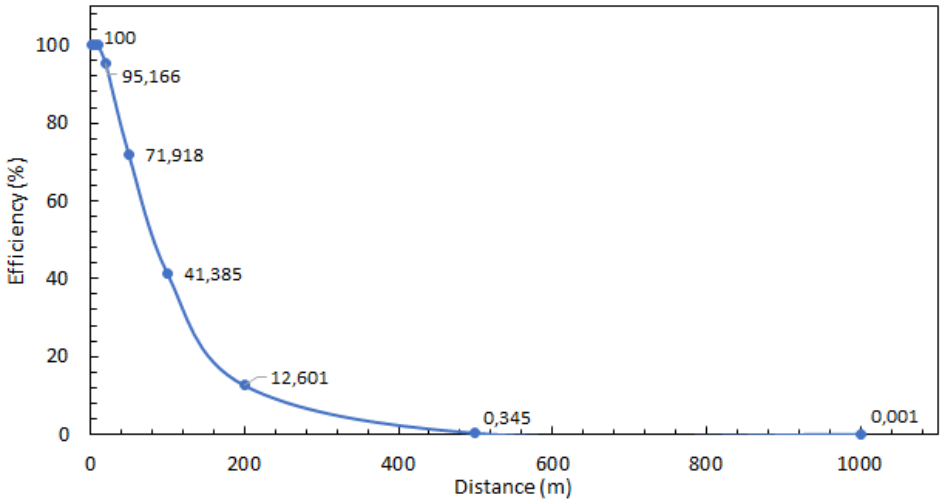

Figure 25: Efficiency (%) for the aircraft primary model as a function of source distance (m), for a 300 keV beam in air, at 1 atm.

It follows that for the air density at 1 atm, there is practically no interaction with the aircraft primary model 1 km away. For the data validation, a new set of simulations was carried out, but now considering vacuum as the environment which is also defined by MEGALib.

Distance (m)	**Triggered/Beamphotons**	**Efficiency (%)**
1	100000	100.000 ±0.316
5	100000	100.000 ±0.316
10	100000	100.000 ±0.316
20	99974	99.974 ±0.316
50	99979	99.979 ±0.316
100	99974	99.974 ±0.316
200	99983	99.983 ±0.160
500	99984	99.984 ±0.316
1000	99984	99.984 ±0.316

Table 10: Source with a beam of 10 mm in diameter, with constant energy of 300 keV and at a distance d from the aircraft primary model; Material: Vacuum.

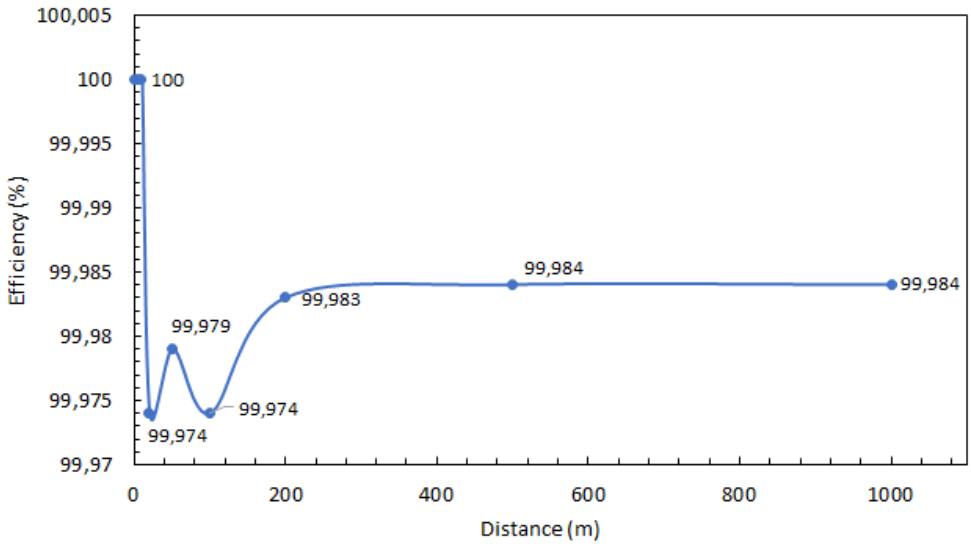

Figure 26: Efficiency (%) for the aircraft primary model as a function of source distance (m), for a 300 keV beam in vacuum.

As expected, we verified that for the vacuum, the efficiency for the aircraft primary model varies from 100 to 99.974%, since there is no interaction of the gamma radiation with the environment. The vacuum type is not specified in MEGALib, but according to GEANT4 specifications, the vacuum is defined as a very low density common gas [13]. In fact, GEANT4 uses a vacuum with a density defined in *PhysicalConstants.h* [13], where density = "universe_mean_density"; pressure = "1.e-19*pascal"; and temperature = "0.1*kelvin", as defined in GEANT4 code. So the medium vacuum is not absolute vacuum and that explains why the efficiency is not 100% for further distances.

3.4.3 Aircraft Primary Model at 10 km altitude

Then, it was simulated using the same procedure, but now considering the Earth's atmosphere at 10 km altitude as the surrounding material, since this altitude corresponds to a typical flight altitude level of the commercial airline flights. To obtain the model of the atmosphere at 10 km altitude, the ".txt" file was used, as explained in section 3.3. An important aspect is that the file provides the quantity of each component in atoms/cm^{-3}. However, for these quantities to be entered in MEGALib it is necessary to use one of two commands: *ComponentByMass*, which asks for the fractional mass of the component in the material; or *ComponentByAtoms*, which requires the number of these atoms in the material (an integer). This way, we will use the *ComponentByMass* and from the quantity,

it is possible to calculate the mass fraction of each constituent; the values are shown in the table 11 below. The values in the *ComponentByMass* column have a different notation since this is how it is necessary to place the values in the code of the file "Atmosphere.geo" of MEGAlib. The same notation is verified in the density since it is also one of the parameters to be placed in the code.

Component	**Atoms/(cm^{-3})**	**ComponentByMass**
Atomic oxygen (O)	0.000	0.000
Nitrogen (N_2)	6.855×10^{18}	7.55584E-01
Oxygen (O_2)	1.839×10^{18}	2.31529E-01
Helium (He)	4.600×10^{13}	7.24327E-07
Argon (Ar)	8.199×10^{16}	1.28871E-02
Atomic hydrogen (H)	0.000	0.000
Atomic nitrogen (N)	0.000	0.000
Density (g/cm^{-3})		4.21700E-04

Table 11: Atmosphere composition at 10 km altitude.

Taking this into account, the simulation was performed and the values are in the table 12 and represented in the graph 27.

Distance (m)	**Triggered/Beamphotons**	**Efficiency (%)**
1	100000	100.000 ±0.316
5	100000	100.000 ±0.316
10	100000	100.000 ±0.316
20	98275	98.275 ±0.313
50	88544	88.544 ±0.298
100	72255	72.255 ±0.269
200	46825	46.825 ±0.216
500	12498	12.498 ±0.112
1000	1315	1.315 ±0.036

Table 12: Source with a beam of 10 mm in diameter, with constant energy of 300 keV and at a distance d from the aircraft primary model; Material: Atmosphere at 10 km of altitude.

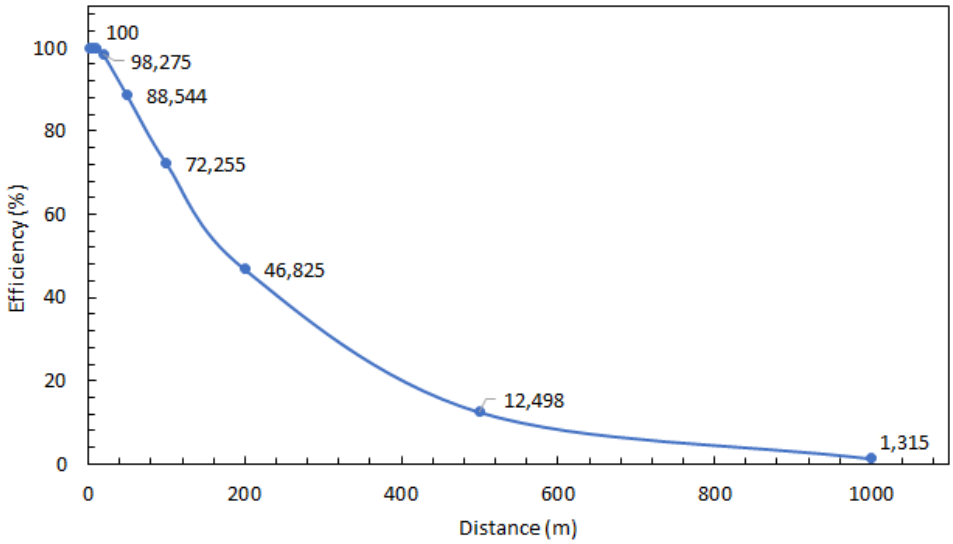

Figure 27: Efficiency (%) for the aircraft primary model as a function of source distance (m), for a 300 keV beam, at 10 km altitude.

The results obtained in the table for the atmosphere at 10 km altitude make sense when compared to those obtained for air, because this graph curve has the same shape as the one for air. The only difference found, as expected, is that for the same distance, data for 10 km of altitude have a greater efficiency when compared with data for air at sea level. This is simply because the density of the atmosphere is lower for 10 km altitude, allowing more interactions with the aircraft primary model. To conclude that the method used to determine the atmospheric composition at 10 km high is correct, the atmosphere composition at 1 atm, that is, on the Earth's surface, will be determined in the same way. That is, according to MEGALib, the *Material Air* corresponds to 1 atm, so we will proceed to the same simulation for 1 atm, but using our model. Thus, if the efficiency values for 1 atm and *Material Air* are similar, it is concluded that our model for approximating the atmosphere is correct and can be used in the following phases of the simulations. The table (table 13) for the composition of the atmosphere at sea level is shown below.

Component	**Atoms/(cm^{-3})**	**ComponentByMass**
Atomic oxygen (O)	0.000	0.000
Nitrogen (N_2)	1.907×10^{19}	7.555E-01
Oxygen (O_2)	5.117×10^{18}	2.316E-01
Helium (He)	1.280×10^{14}	7.245E-07
Argon (Ar)	2.282×10^{17}	1.289E-02
Atomic hydrogen (H)	0.000	0.000
Atomic nitrogen (N)	0.000	0.000
Density (g/cm^{-3})		1.174E-03

Table 13: Atmosphere composition at sea level.

Thus, a 300 keV beam is then emitted, 10 mm in diameter, and at a distance d from the aircraft simple model. The values are shown in table 14 and in the graph 28.

Distance (m)	**Triggered/Beamphotons**	**Efficiency (%)**
1	100000	100.000 ±0.316
5	100000	100.000 ±0.316
10	100000	100.000 ±0.316
20	95447	95.447 ±0.309
50	72832	72.832 ±0.270
100	42167	42.167 ±0.205
200	13497	13.497 ±0.116
500	390	0.390 ±0.020
1000	0	0.000 ±0.000

Table 14: Source with a beam of 10 mm in diameter, with constant energy of 300 keV and at a distance d from the aircraft primary model; Material: our Earth's surface atmosphere model at 1 atm.

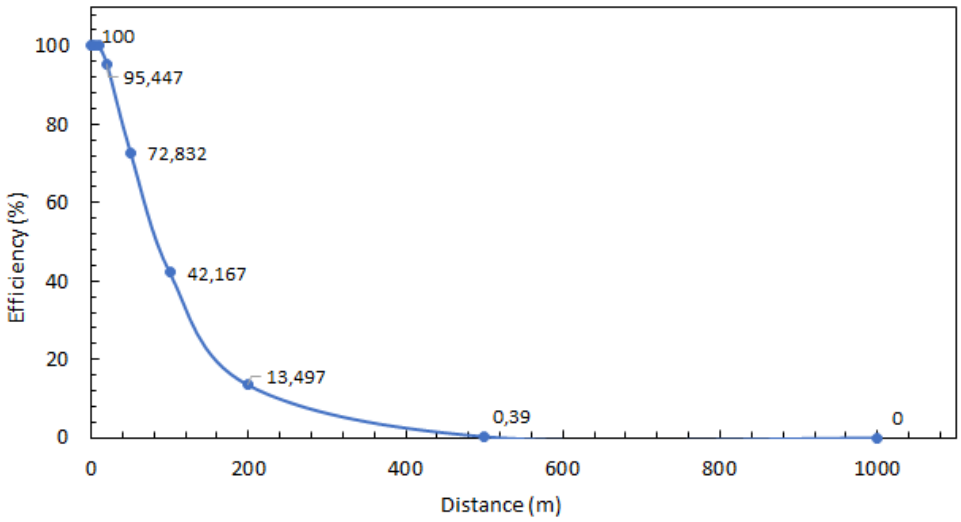

Figure 28: Efficiency (%) for the aircraft primary model as a function of source distance (m), for a 300 keV beam for our Earth's surface atmosphere model at 1 atm.

Comparing graphs 25 and 28, it is possible to verify that the values obtained from the simulations between *Material Air* at the Earth's surface, defined by MEGALib, and the composition of the atmosphere, approximated by our method, show very similar tends. It is observed in both graphs that for a source far from 1, 5 and 10 m, the efficiency of the aircraft primary model is about 100%. As the source moves away from the aircraft primary model, the variation in efficiency as a function of distance show similar trends shape and very close detection efficiency rates. It is also confirmed that for a distance of 1 km there are practically no events. Thus, it can be concluded that the method used to calculate the components of the atmosphere for high altitudes (10 km and other altitudes in the next sections) is correct.

3.4.4 Aircraft Primary Model: Monochromatic beam

The next phase aims to analyze the absorption of gamma-rays as a function of distance, but for the entire range of energy from typical emissions of TGFs. Now that we have confidence in this model, these calculations will be repeated for minimum and maximum emission energies of TGFs. Currently, TGFs are detected in the energy range from 100 keV to 100 MeV, so these will be the limits to be used in the next phase of the simulations. Considering again the altitude of 10 km and the respective atmosphere composition, the efficiency of the aircraft simple model will be determined for a monochromatic beam of

100 keV, 1 MeV, and 100 MeV, for a source that is moving further and further away from the aircraft primary model. The beam remains 10 mm in diameter. As more realistic information is being considered, the distances will be greater, the first being 50 m and the last 50 km, to evaluate the photons' range.

The values for each energy beam, that is, 100 keV, 1 MeV, and 100 MeV, are in the tables 15, 16, and 17. The representation of the values is in a single graph (figure 29), to allow better visualization of the differences between the energies used.

Distance (m)	**Triggered/Beamphotons**	**Efficiency (%)**
50	83073	83.073 ±0.288
100	61955	61.955 ±0.249
500	5036	5.036 ±0.071
1000	208	0.208 ±0.014
5000	0	0.000 ±0.000

Table 15: Source with a beam of 10 mm in diameter, with constant energy of 100 keV and at a distance d from the aircraft primary model; Material: Atmosphere at 10 km altitude.

Distance (m)	**Triggered/Beamphotons**	**Efficiency (%)**
50	93877	93.877 ±0.306
100	83472	83.472 ±0.289
500	29314	29.314 ±0.171
1000	7638	7.638 ±0.087
5000	0	0.000 ±0.000

Table 16: Source with a beam of 10 mm in diameter, with constant energy of 1 MeV and at a distance d from the aircraft primary model; Material: Atmosphere at 10 km altitude.

Distance (m)	Triggered/Beamphotons	Efficiency (%)
50	100000	100.000 ±0.316
100	99999	99.999 ±0.316
500	93267	93.267 ±0.305
1000	71592	71.592 ±0.268
5000	4645	4.645 ±0.068
10000	114	0.114 ±0.011
50000	0	0.000 ±0.000

Table 17: Source with a beam of 10 mm in diameter, with constant energy of 100 MeV and at a distance d from the aircraft primary model; Material: Atmosphere at 10 km altitude.

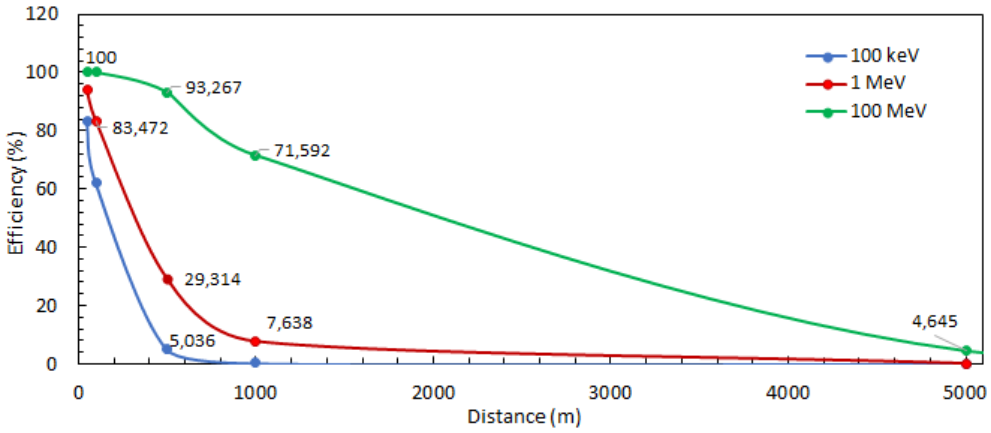

Figure 29: Efficiency (%) for the aircraft primary model as a function of source distance (m), for a 100 keV, 1 MeV and 100 MeV beam at 10 km altitude.

The data in the graph 29 are in agreement with the data obtained in the simulations above. In fact, these curves show similar trends, again corroborating that the method used to approximate the atmospheric composition is correct. As expected, as energy increases, the number of photons that reach the aircraft also increases. Clearly, for 100 MeV there are many more interactions than for 100 keV, considering the same distances. It is also concluded that a source 50 km from the aircraft primary model, generates approximately 0 interactions.

Then, the same procedure was carried out for 20 km of altitude, obtaining the same conclusions. However, it appears that the number of interactions for 20 km altitude is greater than for 10 km altitude, for each distance from the source. This is due to the variation in atmospheric density. In fact, for 10 km of altitude, there is a density column of 270 g/cm^2, while for 20 km of altitude there are 62 g/cm^2 [18]. Simulations were performed for altitudes of 15 and 20 km, just to confirm that the number of interactions increases with altitude and that the simulations we are carrying out have consistent values. However, these data will not be used for our study, since the flight altitudes of commercial aircraft varies from 7.62 km to 12.5 km. So simulations will now be carried out for the altitudes of 7.5 km and 12.5 km to obtain the efficiency of the aircraft primary model again. The atmospheric compositions for 7.5 km and 12 km are in the tables 18 and 19.

Component	**Atoms/(cm^{-3})**	**ComponentByMass**
Atomic oxygen (O)	0.000	0.000
Nitrogen (N_2)	8.881×10^{18}	7.55624E-01
Oxygen (O_2)	2.382×10^{18}	2.31490E-01
Helium (He)	5.960×10^{13}	7.24422E-07
Argon (Ar)	1.062×10^{17}	1.28851E-02
Atomic hydrogen (H)	0.000	0.000
Atomic nitrogen (N)	0.000	0.000
Density (g/cm^{-3})		5.46400E-04

Table 18: Atmosphere composition at 7.5 km altitude.

Component	**Atoms/(cm^{-3})**	**ComponentByMass**
Atomic oxygen (O)	0.000	0.000
Nitrogen (N_2)	5.234×10^{18}	7.55599E-01
Oxygen (O_2)	1.404×10^{18}	2.31511E-01
Helium (He)	3.512×10^{13}	7.24293E-07
Argon (Ar)	6.261×10^{16}	1.28891E-02
Atomic hydrogen (H)	0.000	0.000
Atomic nitrogen (N)	0.000	0.000
Density (g/cm^{-3})		3.22000E-04

Table 19: Atmosphere composition at 12.5 km altitude.

For these two cases, homogeneous and mono-energetic beams of 100 keV, 1 MeV, and 100 MeV were again considered. Distances vary from 50 m to 20 km, since it was found that for 50 km distance there was almost no interaction. All graphs for the different altitudes

present an expected curve. As the altitude increases, the atmospheric density decreases, contributing to the decrease in the interaction of gamma-rays with air particles. Therefore, the higher the altitude, the greater the number of gamma-rays reaching the aircraft primary model, as expected. Firstly, we have simulations for 7.5 km of altitude, corresponding to the tables 20, 21, and 22 and the graph 30. The, tables, 23, 24, and 25 and graph 31 refer to 12.5 km high.

Distance (m)	**Triggered/Beamphotons**	**Efficiency (%)**
50	78990	78.990 ±0.281
100	54261	54.261 ±0.233
500	2093	2.093 ±0.046
1000	44	0.044 ±0.007
5000	0	0.000 ±0.000

Table 20: Source with a beam of 10 mm in diameter, with constant energy of 100 keV and at a distance d from the aircraft primary model; Material: Atmosphere at 7.5 km altitude.

Distance (m)	**Triggered/Beamphotons**	**Efficiency (%)**
50	92253	92.253 ±0.304
100	79342	79.342 ±0.282
500	20600	20.600 ±0.144
1000	3699	3.699 ±0.061
5000	0	0.000 ±0.000

Table 21: Source with a beam of 10 mm in diameter, with constant energy of 1 MeV and at a distance d from the aircraft primary model; Material: Atmosphere at 7.5 km altitude.

Distance (m)	Triggered/Beamphotons	Efficiency (%)
50	100000	100.000 ±0.316
100	99999	99.999 ±0.316
500	90551	90.551 ±0.301
1000	63006	63.006 ±0.251
5000	1743	1.743 ±0.042
10000	16	0.016 ±0.004
20000	0	0.000 ±0.000

Table 22: Source with a beam of 10 mm in diameter, with constant energy of 100 MeV and at a distance d from the aircraft primary model; Material: Atmosphere at 7.5 km altitude.

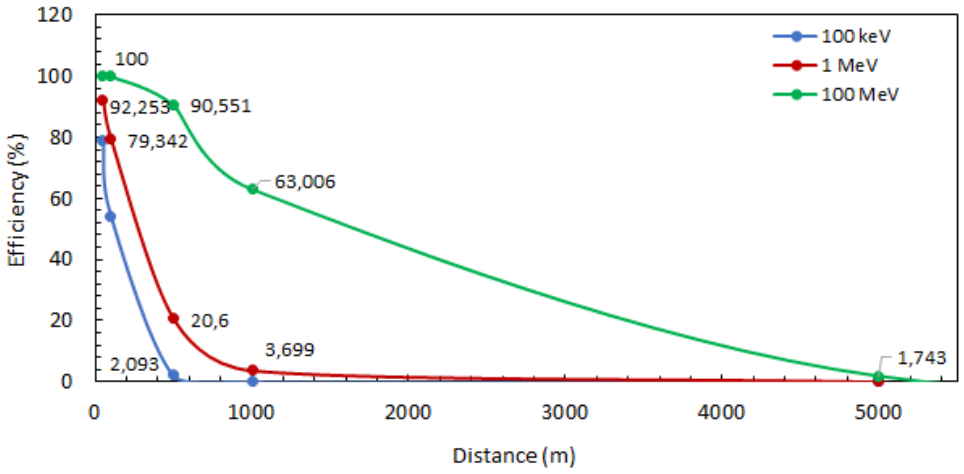

Figure 30: Efficiency (%) for the aircraft primary model as a function of source distance (m), for a 100 keV, 1 MeV and 100 MeV beam at 7.5 km altitude.

Distance (m)	**Triggered/Beamphotons**	**Efficiency (%)**
50	86694	86.694 ±0.294
100	69199	69.199 ±0.263
500	10074	10.074 ±0.100
1000	876	0.876 ±0.030
5000	0	0.000 ±0.000

Table 23: Source with a beam of 10 mm in diameter, with constant energy of 100 keV and at a distance d from the aircraft primary model; Material: Atmosphere at 12.5 km altitude.

Distance (m)	**Triggered/Beamphotons**	**Efficiency (%)**
50	95412	95.412 ±0.309
100	87291	87.291 ±0.295
500	39271	39.271 ±0.198
1000	14261	14.261 ±0.119
5000	1	0.001 ±0.001
10000	0	0.000 ±0.000

Table 24: Source with a beam of 10 mm in diameter, with constant energy of 1 MeV and at a distance d from the aircraft primary model; Material: Atmosphere at 12.5 km altitude.

Distance (m)	**Triggered/Beamphotons**	**Efficiency (%)**
50	100000	100.000 ±0.316
100	100000	100.000 ±0.316
500	95410	95.410 ±0.309
1000	78732	78.732 ±0.281
5000	9611	9.611 ±0.098
10000	664	0.664 ±0.026
20000	2	0.002 ±0.001

Table 25: Source with a beam of 10 mm in diameter, with constant energy of 100 MeV and at a distance d from the aircraft primary model; Material: Atmosphere at 12.5 km altitude.

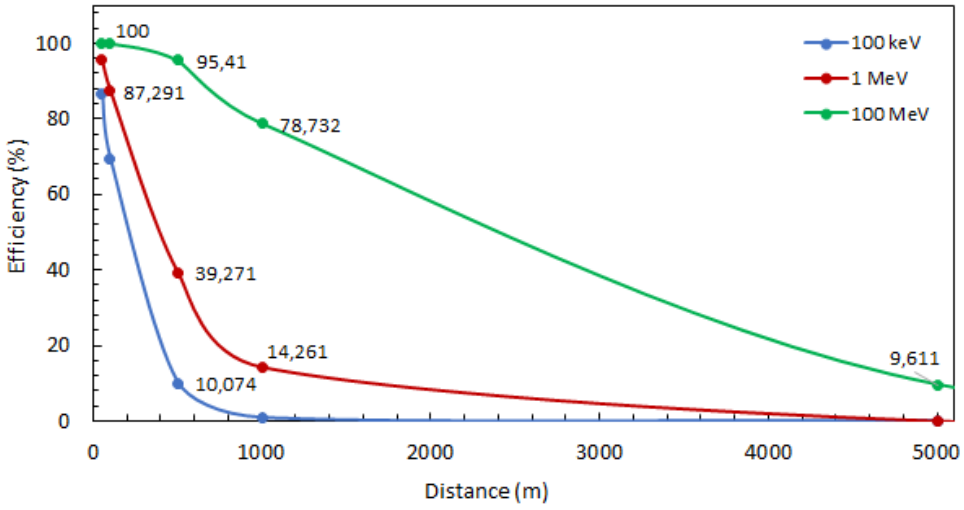

Figure 31: Efficiency (%) for the aircraft primary model as a function of source distance (m), for a 100 keV, 1 MeV and 100 MeV beam at 12.5 km altitude.

3.4.5 Aircraft Primary Model: Power-law

For this simulation set, the simplified aircraft model remains with the same characteristics of the simulations above, only a few parameters are changed at the source. For the study of photon indexes, the altitude of 12.5 km was chosen, because it is a typical flight altitude and it is rare for commercial planes to fly above 12.5 km. This way, the composition of the atmosphere was obtained for 12.5 km of altitude, through the same method described in the previous sections and already described in table 19.

Source features

The beam remains a homogeneous beam with 10 mm in diameter and the flow with 50 particles per second. This value for the flow is maintained since it is a required value for the simulation to run, and as mentioned before, it does not affect the interactions, because the stopping factor remains 100000 triggers. Thus, 100000 gamma photons are emitted through a power-law function. The distribution of the differential TGFs intensity is expressed as a power-law:

$$\frac{dN}{dn} = A_0 n^{-\lambda} \tag{3}$$

where dN is the number of TGFs observed in the dn range, A_0 is the normalization factor and λ is the photon index. This distribution of intensities is achieved through the observed altitudes of the TGF sources, combining with the satellite's detection efficiency. Cosima provide the following definition and parameterization for a power-law:

$$I(E) \propto E^{-p_4} \ \forall \ E \in [p_2, p_3] \tag{4}$$

where, p_2 is the minimum energy in keV, p_3 is the maximum energy in keV and p_4 is the photon index [41]. This way, it is possible to check the efficiency of the aircraft primary model, for different distances, but considering a function that covers the entire energy range of the TGFs. Besides, there are different values for the photon index, according to the energy spectra observed by the satellites referred to in section 2.1 so a set of simulations will be carried out to determine the best photon index to use.

Photon index for BATSE

The energy spectrum of the TGFs measured by BATSE is proportional to the function: $\varepsilon^{-\lambda}$, where ε is the count energy and λ is the photon index, which is between 0.6 and 1.5 [18]. This way, three simulations will be carried out, for a photon index equal to 0.6, 1 and 1.5, considering the energy range from 100 keV to 100 MeV. It was decided to make the simulations for the photon index equal to 1, to understand the behavior of the interactions in the middle of this range of values. Below are the tables (tables 26, 27 and 28) and the respective graph (graph 32).

Distance (m)	**Triggered/Beamphotons**	**Efficiency (%)**
50	98777	98.777 ±0.314
100	96421	96.421 ±0.311
500	75158	75.158 ±0.274
1000	54569	54.569 ±0.234
5000	5609	5.609 ±0.075
10000	368	0.368 ±0.019
20000	0	0.000 ±0.000

Table 26: Source with a beam of 10 mm in diameter, with a power-law from 100 keV to 100 MeV, and at a distance d from the aircraft primary model; Material: Atmosphere at 12.5 km altitude; Photon index = 0.6.

Distance (m)	**Triggered/Beamphotons**	**Efficiency (%)**
50	96444	96.444 ±0.311
100	90582	90.582 ±0.301
500	56105	56.105 ±0.237
1000	35579	35.579 ±0.189
5000	2956	2.956 ±0.054
10000	169	0.169 ±0.013
20000	0	0.000 0.000

Table 27: Source with a beam of 10 mm in diameter, with a power-law from 100 keV to 100 MeV, and at a distance d from the aircraft primary model; Material: Atmosphere at 12.5 km altitude; Photon index = 1.

Distance (m)	**Triggered/Beamphotons**	**Efficiency (%)**
50	92896	92.896 ±0.305
100	81950	81.950 ±0.286
500	32375	32.375 ±1.180
1000	14356	14.356 ±0.120
5000	703	0.703 ±0.027
10000	33	0.033 ±0.006
20000	0	0.000 ±0.000

Table 28: Source with a beam of 10 mm in diameter, with a power-law from 100 keV to 100 MeV, and at a distance d from the aircraft primary model; Material: Atmosphere at 12.5 km altitude; Photon index = 1.5.

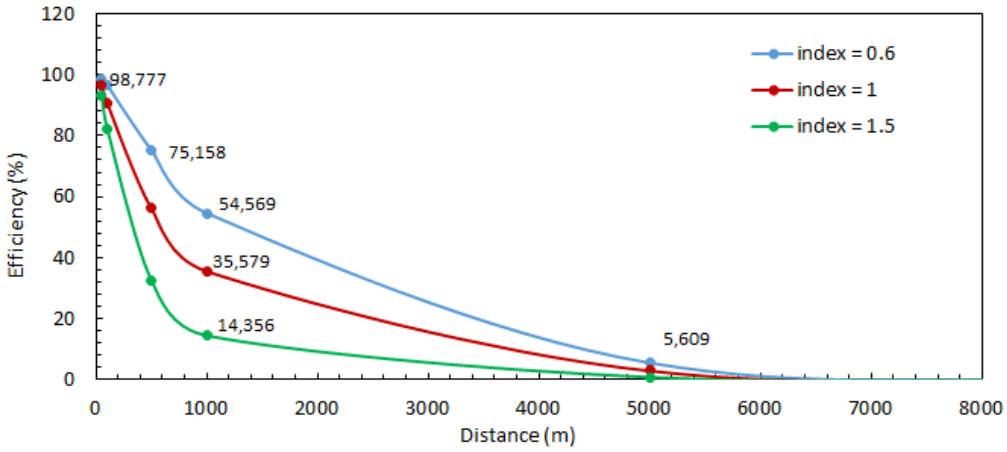

Figure 32: Efficiency (%) for the aircraft primary model as a function of source distance (m), for BATSE photon indexes, through a power-law from 100 keV to 100 MeV, at 12.5 km altitude.

Comparing the tables obtained with the data above for mono-energetic beams, it follows that the approximation to a power-law gives coherent and true values. The same can be verified by the graph curves. It is observed between the three curves that the higher the photon index, the lower the efficiency of the aircraft primary model, for the same energy situation and distance from the source. Therefore, in terms of increased efficiency, the lowest photon index should be used. However, as BATSE represents the oldest and most flawed satellite, BATSE photon indexes will not be considered in the next phase of the simulations.

Photon index for RHESSI

The energy spectrum of TGFs observed by RHESSI is also approximated by a power-law, but in this case with a photon index equal to 2.6, for the entire energy distribution. This way, simulations were performed for this case at 12.5 km altitude. The values are in the table 29 and represented in the graph 33. It is possible to verify that the graph presents a curve with the same shape as those obtained for BATSE. The photon index for the total distribution of the RHESSI spectrum is greater than those used by BATSE, but again, this higher photon index leads to a decrease in the efficiency of the aircraft primary model, when compared to BATSE. The RHESSI energy spectrum is also approximated to a cumulative spectrum, which will be explained and presented in section 3.6.

Distance (m)	Triggered/Beamphotons	Efficiency (%)
50	89091	89.091 ±0.298
100	74158	74.158 ±0.272
500	16375	16.375 ±0.128
1000	2966	2.966 ±0.054
5000	3	0.003 ±0.002
10000	0	0.000 ±0.000

Table 29: Source with a beam of 10 mm in diameter, with a power-law from 100 keV to 100 MeV, and at a distance d from the aircraft primary model; Material: Atmosphere at 12.5 km altitude; Photon index = 2.6.

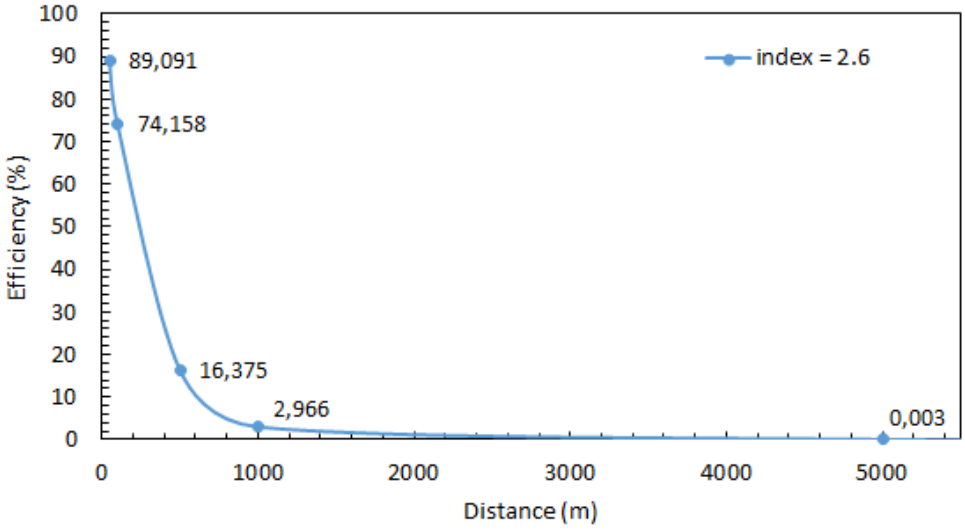

Figure 33: Efficiency (%) for the aircraft primary model as a function of source distance (m), for RHESSI photon index, through a power-law from 100 keV to 100 MeV, at 12.5 km altitude.

Photon index for Fermi

The best value for Fermi - GBM TGF observations was $\lambda = 2.20 \pm 0.13$ [25]. This is a value very close to that obtained by RHESSI, so it is expected that the simulations

will give efficiencies similar to those obtained by the RHESSI photon index. This way, the simulations were carried out for an atmospheric composition at 12.5 km altitude, but using a photon index of 2.20 ± 0.13.

Distance (m)	**Triggered/Beamphotons**	**Efficiency (%)**
50	89948	89.948 ±0.300
100	75630	75.630 ±0.275
500	18617	18.617 ±0.136
1000	4438	4.438 ±0.067
5000	53	0.053 ±0.007
10000	2	0.002 ±0.001
20000	0	0.000 ±0.000

Table 30: Source with a beam of 10 mm in diameter, with a power-law from 100 keV to 100 MeV, and at a distance d from the aircraft primary model; Material: Atmosphere at 12.5 km altitude; Photon index = 2.20 ±0.13.

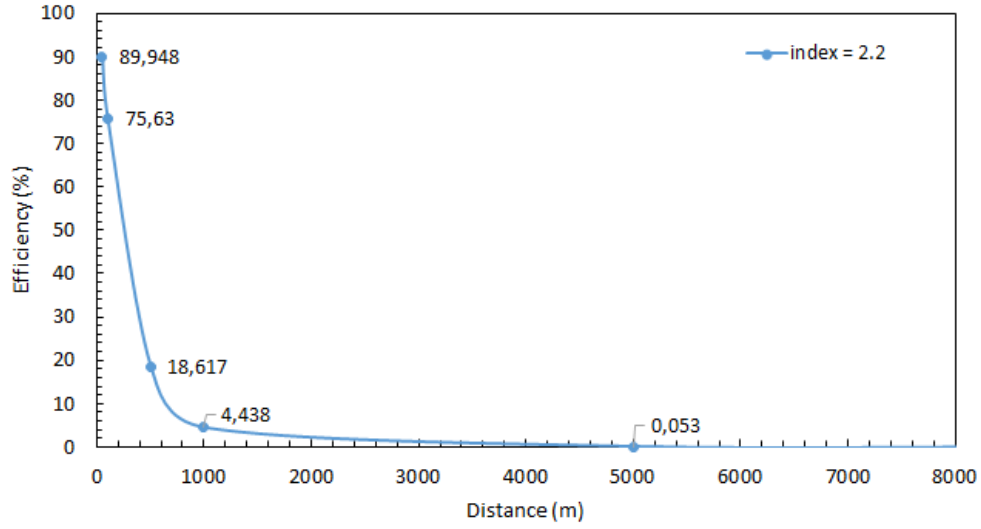

Figure 34: Efficiency (%) for the aircraft primary model as a function of source distance (m), for Fermi photon index, through a power-law from 100 keV to 100 MeV, at 12.5 km altitude.

Through the table 30 and the graph 34, it is confirmed that the efficiency values for the RHESSI and Fermi photon index are very close.

Photon index for AGILE

It can be seen through the AGILE spectrum that TGFs can be divided into two populations, one with low energy and the other with high energy. The higher energy population becomes dominant for energies above 30 MeV [25]. It was also found that the AGILE spectrum can be approximated to a power-law, with the following conditions:

1. $\varepsilon^{-0.5\pm0.1}$ for 1 MeV $< \varepsilon <$ 7.1 $\pm$ 0.5 MeV;
2. $\varepsilon^{-2.7\pm0.1}$ for 7.1 $\pm$ 0.5 MeV $< \varepsilon <$ 100 MeV;

where ε is the count energy. Thus, two simulations will be carried out, one for each index and considering the energy ranges for each one, for 12.5 km altitude.

Distance (m)	**Triggered/Beamphotons**	**Efficiency (%)**
50	98572	98.572 ±0.314
100	94153	94.153 ±0.307
500	60716	60.716 ±0.246
1000	35375	35.375 ±0.188
5000	896	0.896 ±0.030
10000	11	0.011 ±0.003
20000	0	0.000 ±0.000

Table 31: Source with a beam of 10 mm in diameter, with a power-law from 1 MeV to 7.6 MeV, and at a distance d from the aircraft primary model; Material: Atmosphere at 12.5 km altitude; Photon index = 0.5 ±0.1.

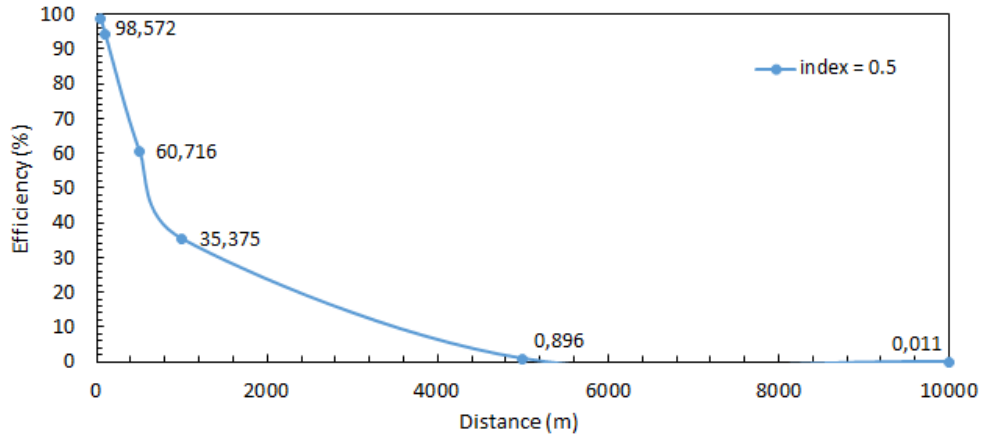

Figure 35: Efficiency (%) for the aircraft primary model as a function of source distance (m), for AGILE photon index, through a power-law from 1 MeV to 7.6 MeV, at 12.5 km altitude.

Distance (m)	**Triggered/Beamphotons**	**Efficiency (%)**
50	99928	99.928 ±0.316
100	98854	98.854 ±0.314
500	79593	79.593 ±0.282
1000	58778	58.778 ±0.242
5000	5309	5.309 ±0.073
10000	267	0.267 ±0.016
20000	4	0.004 ±0.002

Table 32: Source with a beam of 10 mm in diameter, with a power-law from 7.7 MeV to 100 MeV, and at a distance d from the aircraft primary model; Material: Atmosphere at 12.5 km altitude; Photon index = 2.7 ±0.1.

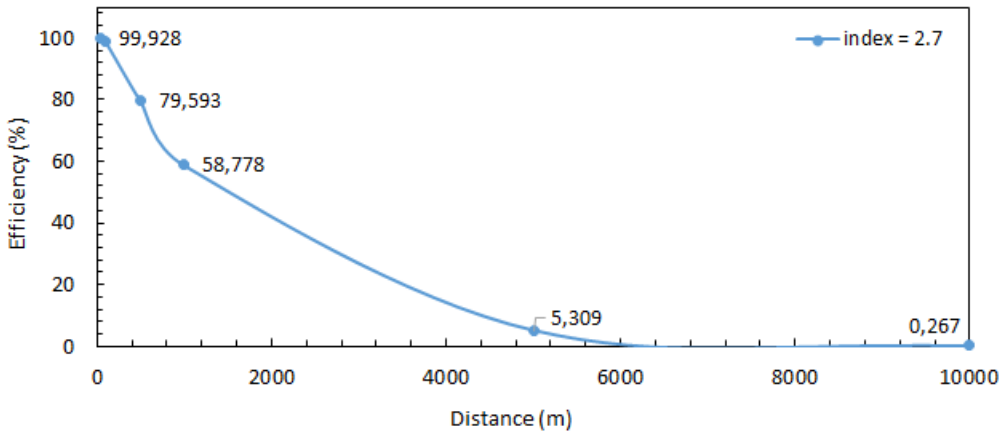

Figure 36: Efficiency (%) for the aircraft primary model as a function of source distance (m), for AGILE photon index, through a power-law from 7.7 MeV to 100 MeV, at 12.5 km altitude.

In fact, there is not a big difference between the trends of the curve for the two indexes (0.5 and 2.7) considered.

3.4.6 Aircraft Primary Model: Cumulative Spectrum

However, a cumulative distribution is also used, as it is compatible with a TGF production altitude of less than 21 km. The cumulative spectrum consists of a sum of the photon energies from several TGFs and is also described as a power-law, with an exponential cutoff model, being:

$$F(E) = kE^{-\alpha}e^{\frac{-E}{E_c}} \tag{5}$$

where k is a constant, E is the count energy, α is the photo index and E_c is the cutoff energy.

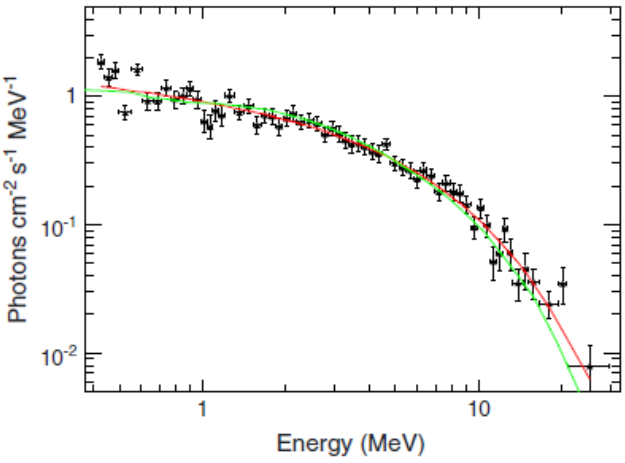

Figure 37: Cumulative spectrum for RHESSI and AGILE data [25].

Figure 37 represents the cumulative spectrum obtained for AGILE (red curve) and RHESSI (green curve). The cumulative spectrum was obtained for AGILE, in a range of 0.4 to 30 MeV, obtaining $\alpha = 0.20^{+0.12}_{-0.13}$, $E_c = 5.5^{+0.7}_{-0.6}$ MeV. The cumulative spectrum of the TGFs observed by AGILE, as well as the location, agrees with the results given by RHESSI [24]. The adjusting for the RHESSI spectrum, also between 0.4 and 30 MeV, we get $\alpha_{RH} = 0.04 \pm 0.03$, $E_{C,RH} = 4.2 \pm 0.2$ MeV. These adjustment parameters between RHESSI and AGILE are not 100% compatible, due to the differences that exist between satellites, such as the adopted trigger selection strategy, the energy limit of the detector, and the satellite range. Thus, simulations were performed for the photon index of AGILE and RHESSI also at 12.5 km altitude. The values are described in tables 33 and 34 and their representation is made together in graph 38.

In another model described by *M. Tavani* [24], the spectra detected by AGILE's MCAL was also adjusted to a simple cutoff power-law model, in the energy range from 500 keV to 40 MeV. In this case, the model has a spectral index of $\alpha = 0.39^{+0.27}_{-0.32}$, $E_c = 8.5^{+3.2}_{-2.2}$ MeV. However, simulations will not be carried out for these values.

Distance (m)	**Triggered/Beamphotons**	**Efficiency (%)**
50	99805	99.805 ±0.316
100	99290	99.290 ±0.315
500	86791	86.791 ±0.295
1000	67422	67.422 ±0.260
5000	7953	7.953 ±0.089
10000	584	0.584 ±0.024
20000	4	0.004 ±0.002

Table 33: Source with a beam of 10 mm in diameter, with a power-law from 100 keV to 100 MeV, and at a distance d from the aircraft primary model; Material: Atmosphere at 12.5 km altitude; Photon index = 0.04 ±0.03.

Distance (m)	**Triggered/Beamphotons**	**Efficiency (%)**
50	99718	99.718 ±0.316
100	98848	98.848 ±0.314
500	84712	84.712 ±0.291
1000	65172	65.172 ±0.255
5000	7417	7.417 ±0.086
10000	495	0.495 ±0.022
20000	2	0.002 ±0.001

Table 34: Source with a beam of 10 mm in diameter, with a power-law from 100 keV to 100 MeV, and at a distance d from the aircraft primary model; Material: Atmosphere at 12.5 km altitude; Photon index = $0.2^{+0.12}_{-0.13}$.

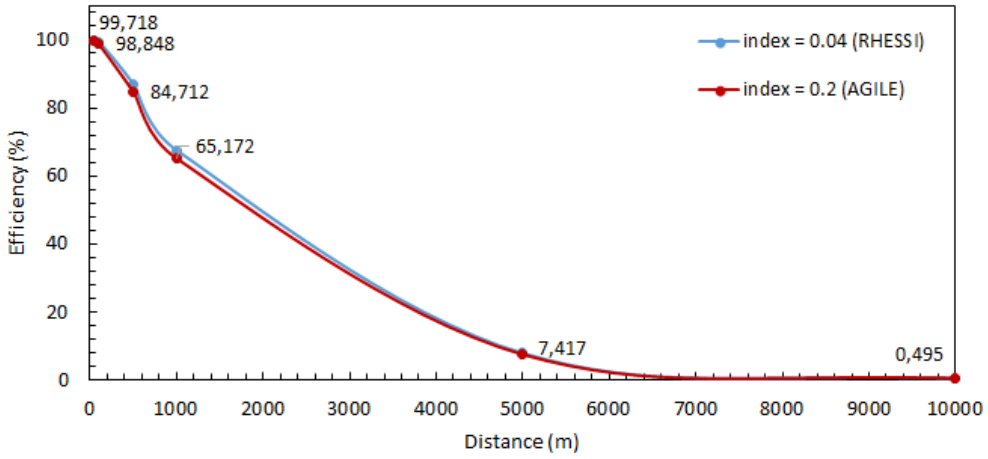

Figure 38: Efficiency (%) for the aircraft primary model as a function of source distance (m), for a RHESSI and AGILE cumulative spectrum, through a power-law from 100 keV to 100 MeV, at 12.5 km altitude.

It can be seen from the graph that the curves are practically overlapped on the measured distances, so it is stated that the efficiency using one or the other photon index will be approximately the same.

3.4.7 Aircraft Primary Model: Broken Power-law

The TGFs intensities can also be approximated to a broken power-law model, using two indexes $\lambda_1 = 1.7$ and $\lambda_2 = 2.6$, for the AGILE spectrum. Cosima provides a broken power-law function and the respective parameters as represented below:

$$I(E) \propto \begin{cases} E^{-p_5}, & \forall\ E \in [p_2, p_4] \\ p_3^{-p_5+p_6}.E^{-p_6}, & \forall\ E \in [p_4, p_3] \end{cases} \tag{6}$$

where, p_2 is the minimum energy in keV, p_3 is the maximum energy in keV, p_4 is the break energy in keV, and the break energy must be between the minimum energy and the maximum energy [41]. In this case, break energy of 10000 keV was used in the program, simply because it is in the middle of the energy range. Then, p_5 is the minimum photon index and p_6 is the maximum photon index, this is, $p_5 = 1.7$ and $p_6 = 2.6$. A simulation was carried out for 12.5 km of altitude and considering the broken power-law function, obtaining the values represented in table 35 and graph 39.

Distance (m)	Triggered/Beamphotons	Efficiency (%)
50	91628	91.628 ±0.303
100	79125	79.125 ±0.281
500	25823	25.823 ±0.161
1000	8934	8.934 ±0.095
5000	213	0.213 ±0.015
10000	11	0.011 ±0.003
20000	0	0.000 ±0.000

Table 35: Source with a beam of 10 mm in diameter, with a broken power-law from 100 keV to 100 MeV, and at a distance d from the aircraft primary model; Material: Atmosphere at 12.5 km altitude; Photon index min = 1.7; Photon index max = 2.6.

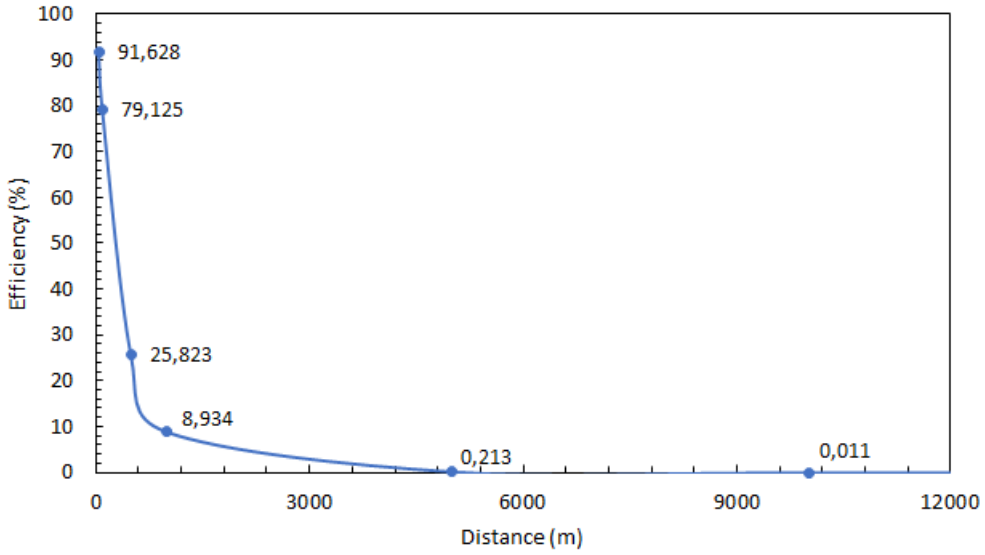

Figure 39: Efficiency (%) for the aircraft primary model as a function of source distance (m), through a broken power-law from 100 keV to 100 MeV, at 12.5 km altitude.

After all these simulations, it is concluded that the photon indexes that allow greater efficiency are those of the cumulative spectrum of RHESSI and AGILE. The photon index that will be used from now on, will be from RHESSI ($\alpha = 0.04 \pm 0.03$). It is our option to use this value because according to the literature [25], it presents a reliable and rep-

resentative spectral profile. Even though, broken power-law profiles are used to represent the energy spectrum of TGFs, power-law TGF are better establish and justified in the literature, in this sense power-laws will be used in the next simulation sets to represent and simulate TGFs.

3.4.8 Aicraft Primary Model: Cone Beam

TGFs are generated by the bremsstrahlung process when energetic electrons collide with air molecules. The energy spectrum and angular distribution of the electrons will determine the angle and energy spectrum of the photons emitted and which will be detected by a satellite or remote detector. The diagram below allows us to exemplify how the bremsstrahlung process happens and how the scattered electron angles are related [12].

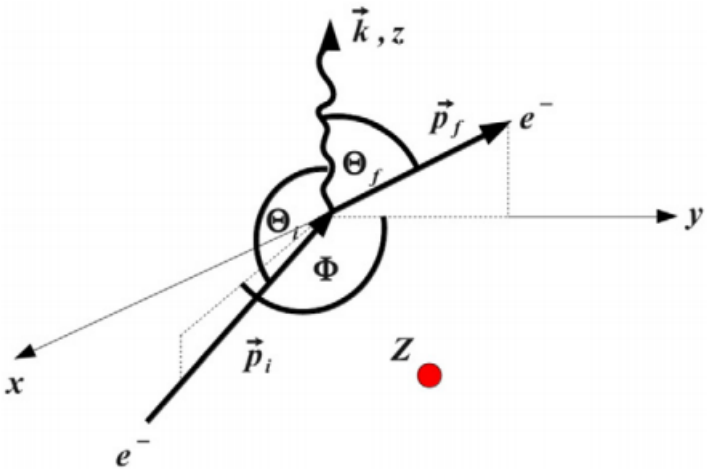

Figure 40: Diagram of representation for the bremsstrahlung process [12].

The incident electron has a p_i moment, the scattered electron has a p_f moment and the emitted photon is represented by the wavy arrow and is emitted with $\hbar\omega$ energy. Z is the atomic number of the scattering nucleus. As can be seen from the diagram, the emitted photon is characterized by the three angles, θ_i, θ_f, and ϕ, such that: θ_i is the angle between the moment of the incident electron and the moment k of the emitted photon; θ_f is the angle between the moment of the scattered electron and the moment k of the emitted photon; ϕ is the angle between the planes measured by the pairs of vectors (p_i, k) and (p_f, k). Thus, it is described by satellite observations that TGFs are emitted in an isotropic cone with an average angle of 30°-40°, indicating that they are produced in almost vertical electric fields (< 20° from vertical). It is also confirmed by *N. Østgaard* [38] that the most likely escape angles are 40° to 49°, but its limit is 60° opening. If it happens to collect a

TGF with a small exhaust angle, it means that it has suffered little dispersion [18]. This angular approach is conditioned by the point of view of the satellite, since measurements have not yet been performed at flight altitudes.

The time taken by photons to travel the accumulated path until they escape the atmosphere is given by $t = s/c$, where c is the speed of light and s is the length of the accumulated path [38]. In figure 41, z is the altitude, E is the energy, α is the polar angle to the Z-axis, β is the azimuth angle, r is the distance from the origin in the XY-plane and s is the length of the accumulated path. The accumulated path length can be calculated from [18]:

$$s \pm = \frac{-1}{a\ cos\alpha} ln \left[1 \pm \frac{ln(1 - rand) a\ cos\alpha}{\mu_\tau\ \rho_{z1}} \right] \tag{7}$$

The + symbol represents the way up, the symbol − represents the way down. The α angle is shown in the figure and is the polar angle to the Z-axis; *rand* is a random number; μ_T is the permeability. The density referring to the initial altitude, z_1, is given by:

$$\rho_{z1} = \rho_0 e^{(-az_1)} \tag{8}$$

where a is the exponential adjustment coefficient to atmospheric density. As they undergo Compton dispersion or pair production, the new s is calculated. This process is repeated until the photon is absorbed, reaches the ground, or escapes from the atmosphere. Electrons are accelerated along the electric field, however, it is the Compton dispersion that leads to the electrons scattering in a cone shape. The greater the dispersion angle, the greater the photon energy reduction. Although the formula of the path length will not be used here in the calculations of the path of the interactions, it serves as a confirmation that TGFs may exist from the bottom up and detected at ground level, as verified by *R. Dwyer* [23].

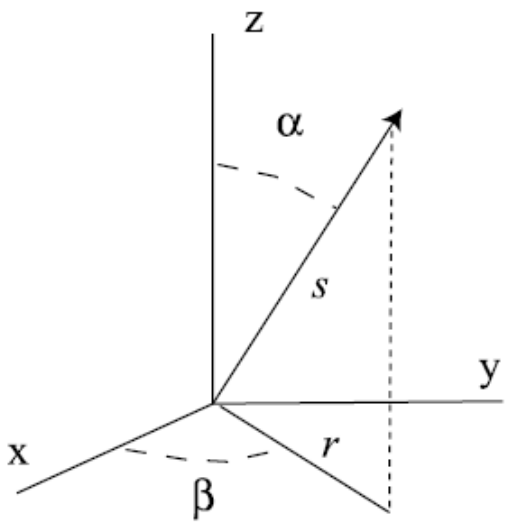

Figure 41: Geometry scheme for photon emission [18].

Source features

For this set of the simulations we will simulate a possible scenario of a commercial aircraft being irradiated by a TGF emission from below, when flying nearby a cumulonimbus cloud. Therefore, we will consider a cone-shaped geometry, oriented according to the z-axis and with direction (0,0,1), as shown in the diagram 42. The stop factor will again be 100000 triggers, so 100000 photons will be emitted through a cone-shaped beam. The flow remains at 50 particles per second, and as mentioned above is a base value for the simulations to run, without affecting the interactions, duration time, or the geometry of the source. Also, the cone emission is isotropic and will have a half opening angle θ, whose calculation and choice will be presented below.

As simulated above, in the study of photon indexes, it was concluded that the way to represent the source would be through a power-law from 100 keV to 100 MeV, using a photon index of 0.04. The source is placed at (0,0,-h) km, where (0,0, -h) corresponds to the tip of the cone. It will always be considered an emission from the bottom up because it is the most usual and frequent form of TGFs emission. The only parameter that will vary in the source is the distance h the source is from the aircraft and the opening angle. This way, a simulation phases will be carried out, to find out what is the best approach for the opening angle of the cone, which will be explained right away.

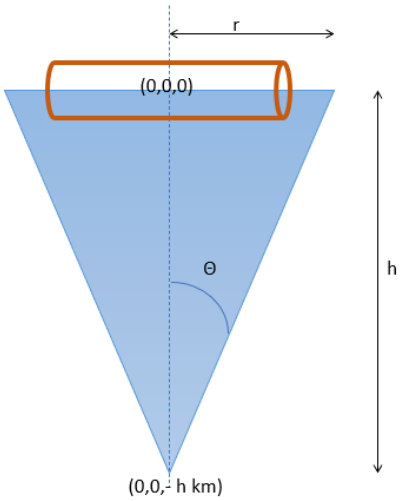

Figure 42: Geometry scheme used in the simulations for photon emission.

3.4.9 A first approach to the study of the cone angle opening

The aircraft is in position (0,0,0), corresponding to an altitude of 12.5 km. Then, the cone center is at a distance h from the aircraft. The cone center altitude will be simulated at 7.5 km, 10 km, and 12 km, with the h taking the values 5, 2.5, and 0.5 km, respectively. These distances were chosen in order to set possible scenarios for an aircraft at typical commercial flight altitude being irradiated by a TGF emission generated at different typical emission altitudes inside cumulonimbus clouds. For this reason, it was considered that 5 km would be the longest distance to simulate. For each range of altitude values, that is, for the difference between 12.5 km and 7.5 km, 10 km, and 12 km, it is necessary to have an atmosphere composition. So, according to the ".txt" file obtained for the constitution of the atmosphere, an average of the composition will be made for each range of values. The data will be presented in the following tables 36, 37, and 38. Again, the mathematical notation in the right-hand column expresses how the values are represented in the code.

Average composition	**ComponentByMass**
Atomic oxygen (O)	0
Nitrogen (N_2)	7.55611E-01
Oxygen (O_2)	2.31501E-01
Helium (He)	7.24357E-07
Argon (Ar)	1.28871E-02
Atomic hydrogen (H)	0
Atomic nitrogen (N)	0
Density (g/cm^{-3})	4.34200E-04

Table 36: Average atmosphere composition between 7.5 km and 12.5 km.

Average composition	**ComponentByMass**
Atomic oxygen (O)	0
Nitrogen (N_2)	7.55591E-01
Oxygen (O_2)	2.31520E-01
Helium (He)	7.24310E-07
Argon (Ar)	1.28881E-02
Atomic hydrogen (H)	0
Atomic nitrogen (N)	0
Density (g/cm^{-3})	3.71850E-04

Table 37: Average atmosphere composition between 10 km and 12.5 km.

Average composition	**ComponentByMass**
Atomic oxygen (O)	0
Nitrogen (N_2)	7.55565E-01
Oxygen (O_2)	2.31546E-01
Helium (He)	7.24291E-07
Argon (Ar)	1.28885E-02
Atomic hydrogen (H)	0
Atomic nitrogen (N)	0
Density (g/cm^{-3})	3.31600E-04

Table 38: Average atmosphere composition between 12 km and 12.5 km.

Again, three sets of simulations will be carried out, one for each value of h, also considering different mean angles of cone opening. The half angles used are 5^o, 30^o, and 40^o.

The radius r is calculated from $r = tg(\theta)$. Thus, for each altitude and angle, there is an associated radius, which will also be represented. The obtained efficiency values are shown in the tables below (tables 39, 40, and 41). The graph 43 shows the value for all simulations, to be able to better observe the difference between the angles used.

Distance (km)	**Radius (km)**	**Triggered/Beamphotons**	**Efficiency (%)**
5	0.437	74	0.074 ±0.009
2.5	0.219	665	0.665 ±0.026
0.5	0.044	10926	10.926 ±0.105

Table 39: Source with a cone beam, with a power-law from 100 keV to 100 MeV; Photon index = 0.04; $\theta = 5^{o}$.

Distance (km)	**Radius (km)**	**Triggered/Beamphotons**	**Efficiency (%)**
5	2.887	6	0.006 ±0.002
2.5	1.443	62	0.062 ±0.008
0.5	0.289	826	0.826 ±0.029

Table 40: Source with a cone beam, with a power-law from 100 keV to 100 MeV; Photon index = 0.04; $\theta = 30^{o}$.

Distance (km)	**Radius (km)**	**Triggered/Beamphotons**	**Efficiency (%)**
5	4.195	1	0.001 ±0.001
2.5	2.098	40	0.040 ±0.006
0.5	0.420	572	0.572 ±0.024

Table 41: Source with a cone beam, with a power-law from 100 keV to 100 MeV; Photon index = 0.04; $\theta = 40^{o}$.

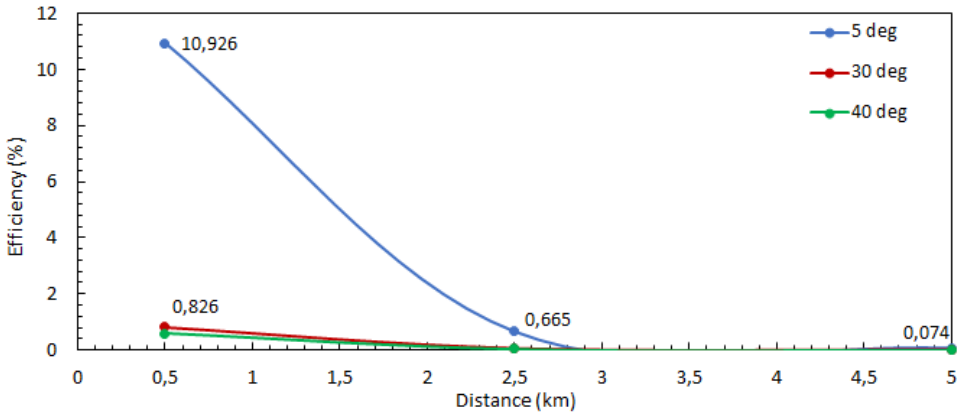

Figure 43: Efficiency (%) for the aircraft primary model as a function of source distance (km), for a source with a cone beam with different opening angles.

It turns out that the efficiency for 5° half-opening is much higher than for 30° or 40°. The 30° and 40° curves are very similar, as they almost overlap. We can be concluded that the lower the TGF aperture angle, the higher is the radiation exposure of the aircraft and passengers.

3.4.10 Aircraft Primary Model: Real flux

According to Fitzpatrick [2015] [17], for an electric field of 400 kV/m, with a source altitude of 15 km and an emission in an isotropic cone with a 45° average angle, a source with 10^5 electrons is created, which will be multiplied by RREA. Thus, for 5 avalanche lengths, that is, for a length of approximately 50 m, 1.6×10^8 photons are propagated from the source to an altitude of 100 km. At this altitude, the atmospheric density is very low, so it is considered that the photons will maintain the trajectory from 100 km to 565 km, corresponding to the Fermi altitude [17]. Also, the satellite must be inside the emission cone so that it can observe the total number of TGFs. Otherwise, the number of TGFs observed decreases considerably, detecting only those with higher energy. For each detector, the number of incident photons is given by the product between the fluence and the detector's geometric area. The fluence, ϕ, is defined by $\phi = \frac{dN}{dA}$. This is the number of particles dN that reach a sphere of cross-section dA and is expressed in m^{-2}. So, the incident photon fluence is calculated by dividing the number of counts observed by the effective area.

Acoording to *T. Gjesteland* [39], three TGFs were observed over the Mediterranean basin, by RHESSI, on the following dates: May 27, 2004, November 7, 2004, and October

16, 2006. These TGFs occurred in the subtropical region, which is outside the typical production region, and come from clouds with a top between 10 and 12 km in altitude. For each TGF, the initial number of photons with energy greater than 1 MeV was estimated, by approximating the propagation of the TGF through the atmosphere to the RHESSI altitude and comparing it with the satellite fluency, using the expression for the typical RREA spectrum:

$$\frac{dN}{dE} \propto \frac{1}{E} \times exp(-E/7.5MeV) \tag{9}$$

where E is the energy. Also an opening of 30° for a typical TGF emission was considered. Thus, the estimated values for the initial number of photons with energy greater than 1 MeV, vary between 4×10^{17} and 7×10^{20}. Taking this into account, a real flow of 1×10^{18} will be considered as a new parameter for our simulations, since, these values are measured according to the fluency of the satellite. As 1×10^{18} is the number of photons and not the flux, this value will be combined with another stopping factor from Cosima, namely time. The time, in seconds, in the code allows the simulation to end after the chosen time, that is, the stopping factor of 100000 triggers will now be replaced by the time in all the following simulations. Therefore, the next phase of simulations will use a cone-shaped source, radiating from below the detector, and using a flow of 1×10^{18} photons for 100 μs, as will be described below.

Horizontal and homogeneous beam

Before proceeding to a more complex cone beam geometry inside the cloud, it was decided, first, to perform control simulations with a small diameter beam (10 mm) horizontally oriented irradiating the aircraft with the same initial intensity. The simulation characteristics and data are shown below.

Source features

The beam will be horizontal and homogeneous in the plane direction, which is 12.5 km above sea level, maintaining the power-law with the same parameters previously defined. The only parameter that will vary is the distance d from the source to the aircraft.

In this new stage, it is necessary to check the stopping time that should be placed in the code, so a simple study was carried out. The average photon fluence is 0.1 cm^{-2}, corresponding to t_{50} = 100 μs where t_{50} corresponds to the time interval in which 50% of the flow occurs. The t_{50} and t_{90} are defined as counting time intervals; the t_{50} is for central events and the t_{90} is for transient events. However, as we are not referring to transient light events, that is, blue jets, red sprites, and elves, we choose to use the t_{50}. Therefore, knowing that t_{50} = 100 μs corresponds to a fluence of 0.1 cm^{-2}, 100 μs was used as a stop criterion for the simulations. But, by putting 100 μs in the source code is neither

feasible nor practical, since for 100 μs the simulation lasted more than a week. So, by decreasing the time, this is, stop criterion, allows the simulations to last less. Then, the times placed were 1×10^{-15}s and 1×10^{-14}s, with 1×10^{-15}s being the time interval that allows the simulation to take less time. After the simulation of each time interval, the theoretical values of the triggered photons were calculated, for 100 μs, through a linear extrapolation. The values are in the tables 42 and 43, and in the graph 44.

Distance (m)	**Triggered/Beamphotons**
50	3.006×10^{19}
100	2.964×10^{19}
500	2.679×10^{19}
1000	2.028×10^{19}
5000	2.130×10^{18}
10000	1.500×10^{17}
20000	0.000

Table 42: Source with a beam of 10 mm in diameter, with a power-law from 100 keV to 100 MeV, at a distance d from the aircraft primary model; Material: Atmosphere at 12.5 km altitude; TGF duration approximated to 10^{-15}s.

Distance (m)	**Triggered/Beamphotons**
50	3.000×10^{19}
100	2.973×10^{19}
500	2.654×10^{19}
1000	2.039×10^{19}
5000	2.376×10^{18}
10000	1.560×10^{17}
20000	0.000

Table 43: Source with a beam of 10 mm in diameter, with a power-law from 100 keV to 100 MeV, at a distance d from the aircraft primary model; Material: Atmosphere at 12.5 km altitude; Approximation by 10^{-14}s.

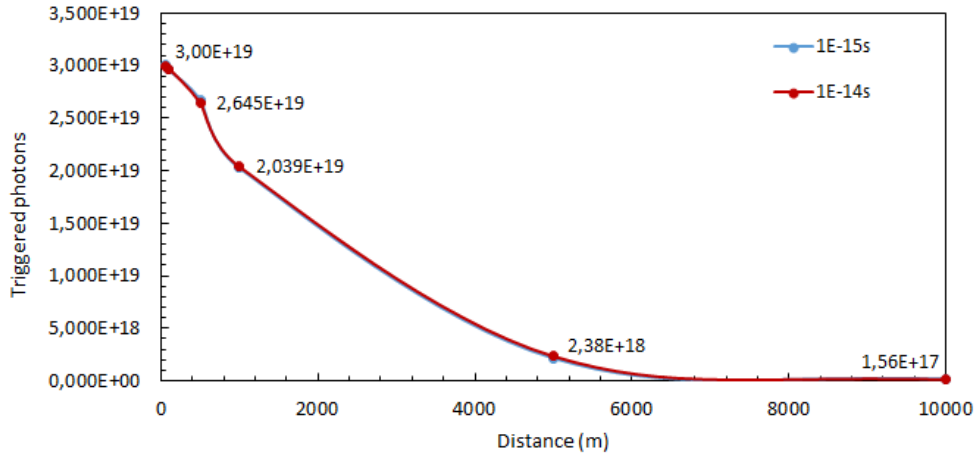

Figure 44: Triggered photons for a linear extrapolation to 100 μs, considering a horizontal beam incident on the aircraft primary model.

In both approaches the orders of magnitude correspond. The values are very similar and by representing the values in the graph, it is observed that the same characteristic curve is maintained. Since the actual flow is now being used, the efficiency of the detector is not calculated, because the objective is to check the amount of triggered photons that reach the aircraft primary model. It is also concluded that using a stopping time other than 100 μs provides a good approximation for triggered photons and that the higher the stopping factor, the better the estimate. In this sense and as for 1×10^{-15}s and 1×10^{-14}s, the simulations last a short time, between one to two hours, it was decided to place 1×10^{-13}s in the following simulations. Thus, a simulation with a more reliable estimate is achieved in a short time.

Cone-shaped isotropic emission

Then, new simulations were carried out, with the characteristics of the source and the aircraft primary model described above but now considering a cone-shaped beam, located under the aircraft. Again, the values of 5, 2.5, and 0.5 km will be considered for h, using the medium atmosphere as an environment, for each range of altitudes. For this case, the time interval 1×10^{-13}s was considered. The values are shown in the table 44 and in the graph 45.

Distance	Triggered/Beamphotons
5 km vertical	4.098×10^{14}
2.5 km vertical	1.347×10^{15}
0.5 km vertical	9.024×10^{16}

Table 44: Source with a cone beam, with a power-law from 100 keV to 100 MeV, at a distance d from the aircraft primary model; Linear extrapolation for 100 μs.

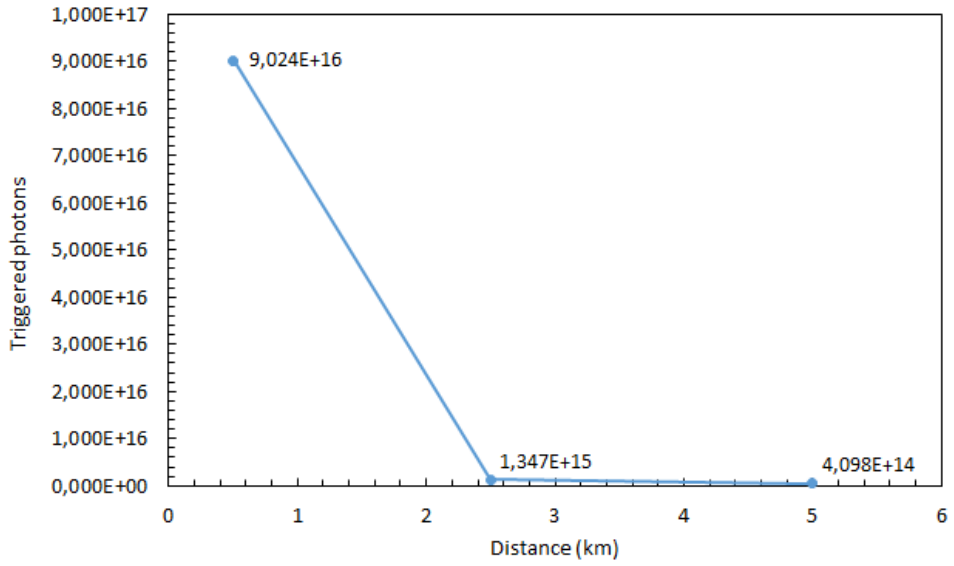

Figure 45: Triggered photons for a linear extrapolation to 100 μs, considering a horizontal beam incident on the aircraft primary model; Stopping time = 1×10^{-13}s.

As expected, for a vertical distance of 5 km there are fewer triggered photons than for 0.5 km, since the source is much closer to the model of the plane. As can be seen from the graph, a good estimate is also achieved with 1×10^{-13}s, with a curve that presents a shape very close to 1×10^{-14}s and 1×10^{-15}s.

Dispersion of events due to the conical shape of the emission

The fact that the emissions of TGFs on average have a conical aperture of 30°, means that not all photons reach the plane and are dispersed through the atmosphere. Thus, an approximation will be made to the exact value of triggered photons arriving at the model

of the airplane, through a relationship between the solid angle of the emission of the TGFs and the angle at which the emission occurs in our simulations. The relationship between the effective areas of the 30^{o} emission cone and the emission cone of our simulations depends on the value of h. This factor will be applied to all the next values of triggered photons, in order to obtain a more real approximation.

3.5 Aircraft Intermediate Model: With Aluminium and Air

As seen in section 2.5, aluminum is the main component of most commercial aircrafts' structures, in particular the aircrafts' fuselage, acting as well as a shield. To verify how the interactions happen by placing a layer of aluminum outside the aircraft model, it was decided to start with a thin layer of 1 cm of aluminum.

1 cm layer of aluminum

The source remains as a cone-shaped beam, located under the plane, at a distance d. The distances used were again 5, 2.5, and 0.5 km. The aircraft model maintains the same dimensions, adding only a 1 cm layer of aluminum surrounding the entire aircraft model. Since the interior of the aircraft is what we are interested in studying, namely the cabin area, it was considered that the air inside the plane is the *Material Air*, previously verified that it is the air corresponding to the atmosphere at sea level. The aircraft air is purified every 3 min, and every hour the air inside the plane's cabin is renewed 10 to 12 times. Therefore, the aircraft intermediate model will be a cylinder made of air, and around it will be a 1 cm layer of a cylinder, called a shield. The shield must also have a cylindrical shape. The values can be seen in the table 45. Note that in these values the ratio factor between the two emission areas is already considered, as described above.

Distance	Triggered/Beamphotons
5 km vertical	3.336×10^{14}
2.5 km vertical	1.216×10^{15}
0.5 km vertical	8.132×10^{16}

Table 45: Source with a cone beam, with a power-law from 100 keV to 100 MeV, at a distance d from the aircraft intermediate model; Average for 100 μs; shield = 1 cm.

Another set of simulations will also be carried out, for two different types of aluminum thickness, one 22 cm, and the other 25 cm. The Boeing 737 model has a fuselage width of 3.76 m and a cabin with 3.54 m. Thus, the width of the aluminum thickness is approximately 22 cm. For the Airbus model, the fuselage width is 3.95 m and the cabin is 3.70 m, making the aluminum thickness 25 cm. The source and model of the aircraft intermediate model remain the same, the only thing that will change is the thickness of the aluminum shield.

22 cm layer of aluminum

Distance	Triggered/Beamphotons
5 km vertical	1.932×10^{14}
2.5 km vertical	7.572×10^{14}
0.5 km vertical	5.792×10^{16}

Table 46: Source with a cone beam, with a power-law from 100 keV to 100 MeV, at a distance d from the aircraft intermediate model; Average for 100 μs, for a 22 cm aluminum shield.

25 cm layer of aluminum

Distance	Triggered/Beamphotons
5 km vertical	1.776×10^{14}
2.5 km vertical	6.915×10^{14}
0.5 km vertical	5.451×10^{16}

Table 47: Source with a cone beam, with a power-law from 100 keV to 100 MeV, at a distance d from the aircraft intermediate model; Average for a 100 μs duration TGF, for a 25 cm aluminum shield.

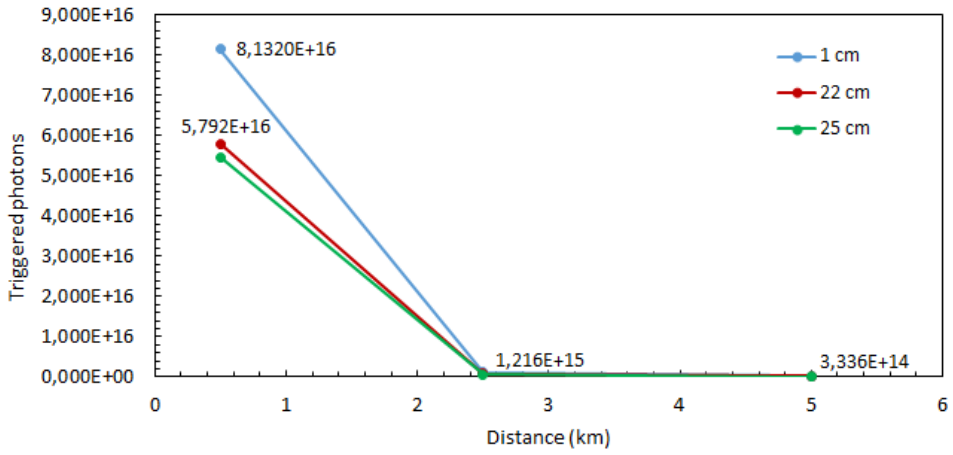

Figure 46: Triggered photons for a linear extrapolation to 100 μs, considering a cone beam incident on the aircraft intermediate model, for three different fuselages thicknesses.

Through these simulations, it is possible to conclude, as expected, that the greater the thickness of the aluminum shield, the smaller the number of triggered photons. This decrease is visible from the graph curves when there is a sharp decrease from 1 cm to 22 cm or from 1 cm to 25 cm. So, the best real thickness to be used in the next simulations is 22 cm. This is because there is only a difference of 3 cm in aluminum, and the curves are very similar, in addition to the fact that with 22 cm of aluminum more events can be achieved in the simulations.

3.6 Aircraft Advanced Model: Phantom

In this simulation set, a phantom model was set in order to evaluate the effect of TGF emissions in human beings inside an aircraft at flight altitude. The phantom is a material that represents human tissues and is widely used to determine the doses received by the tissue, as in studies of radiology and medical imaging. The phantom used in an example of MEGALib has the following components: Water, rib bone, spine bone, muscle, lung, brain and skull. Each of these constituents has its *Component By Mass* of the atoms present and the respective quantities. A real flow of 1×10^{22} particles per second is still used, and the source remains cone-shaped. The aircraft model maintains the same dimensions. It will consist of a 22 cm thick aluminium shield and inside it, instead of *Material Air*, the phantom material will be placed. We will thus have an advanced aircraft model consisting of a cylindrical mass only with phantom. This more abrupt approach was considered to verify how each component of the MEGALib phantom behaves in the simulations and how much each component can receive. This way, it was possible to obtain a more effective approach for the determination of the triggered photons obtained in each component. The stopping factor of the simulations was 1×10^{-13} s, and then the linear extrapolation to 100 μs was performed. The table below shows the average triggers that occur for sources distant from 5 km, 2.5 km, and 0.5 km from the aircraft.

Component	**Distance**	**Triggered/Beamphotons**
Water	5 km	6.120×10^{14}
	2.5 km	2.346×10^{15}
	0.5 km	1.601×10^{17}
RibBone	5 km	6.402×10^{14}
	2.5 km	2.354×10^{15}
	0.5 km	1.619×10^{17}
SpineBone	5 km	5.730×10^{14}
	2.5 km	2.359×10^{15}
	0.5 km	1.600×10^{17}
Muscle	5 km	6.252×10^{14}
	2.5 km	2.382×10^{15}
	0.5 km	1.600×10^{17}
Lung	5 km	6.630×10^{14}
	2.5 km	2.308×10^{15}
	0.5 km	1.591×10^{17}
Brain	5 km	6.336×10^{14}
	2.5 km	2.404×10^{15}
	0.5 km	1.612×10^{17}
Skull	5 km	6.204×10^{14}
	2.5 km	2.353×10^{15}
	0.5 km	1.613×10^{17}

Table 48: Source with a cone beam, with a power-law from 100 keV to 100 MeV, at a distance d from the aircraft advanced model; Average for 100 μs duration TGF, for the different phantom components.

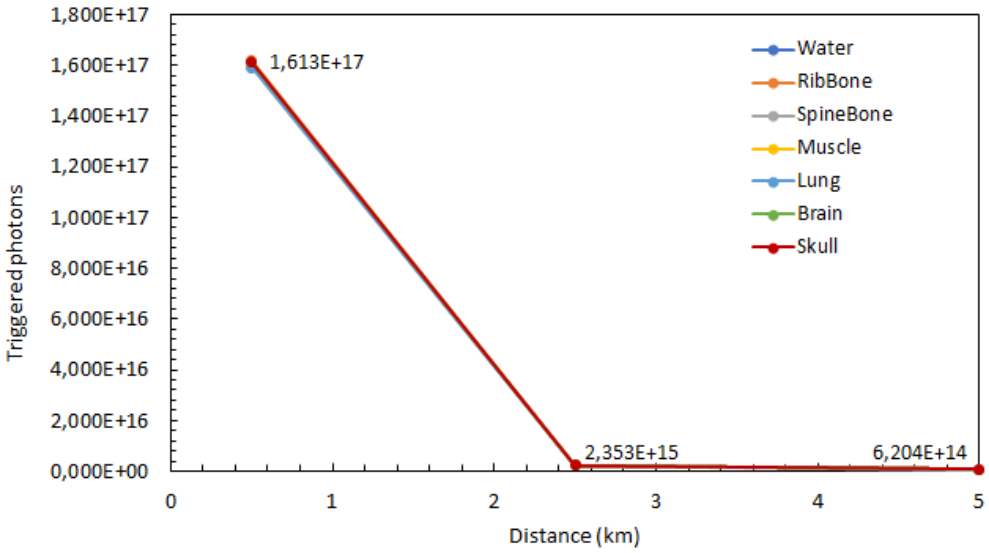

Figure 47: Triggered photons for a linear extrapolation to 100 μs, considering a cone beam incident on the aircraft advanced model, for each phantom component.

There isn't a big difference between the values of the components. In other words, no component deviates too much from the rest in terms of triggered photons, also showing orders of magnitude in a range of 10^{14} to 10^{17}. This is also confirmed by the graph curves, graph 47, where there is an overlap for all components. As expected, it is observed that the greater the distance from the source to the aircraft, the smaller the number of events.

3.7 Human model

Then, a human model was set in order to be placed inside the aircraft cylindrical volume filled with air to simulate a passenger or crew member irradiation by a TGF. Firstly, a human model was set by simply approaching the body volume to a cylinder with 1.80 m long and 47 cm in diameter. The human will be placed inside the plane, vertically and in the position (0,0,0), as shown in the diagram below (figure 48). Then the source will be a beam with a power law profile from 100 keV up to 100 MeV, with 0.04 as the photon index. The blue cylinder represents the human and the orange cylinder represents the 22 cm thick aluminum plane fuselage. The material inside the plane will again be *Material Air*. The simulations were restricted to water, because the human body is abundant in water and there is not a big difference in triggered photons for all the phantom components. So it is intended to verify how many triggered are obtained for the human model constituted

only by water. It is a valid approximation, because, as seen in table 48, there is not a significant difference between the recorded absorption relative to the different phantom components, essentially varying within 10 to 20%. However, it is worthy to note that the muscle generates a greater amount of triggered photons. Thus, the number of triggered photons for each distance is in the table below 49 and represented in graph 50.

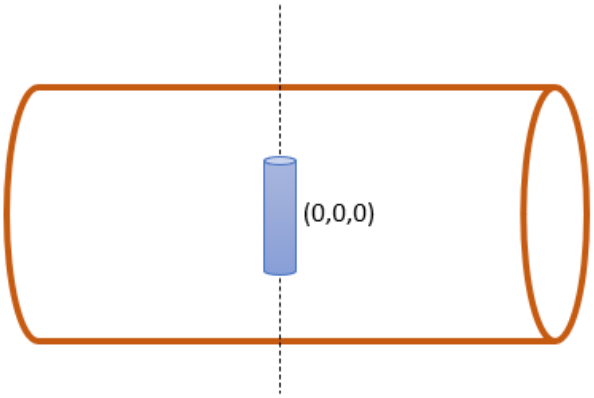

Figure 48: Diagram for the approximate human model, with cylindrical geometry, inside the aircraft advanced model.

The figure below (figure 49)represents a spectrum of emission of TGFs through a power-law, with the photon index equal to 0.04, obtained by MEGALib.

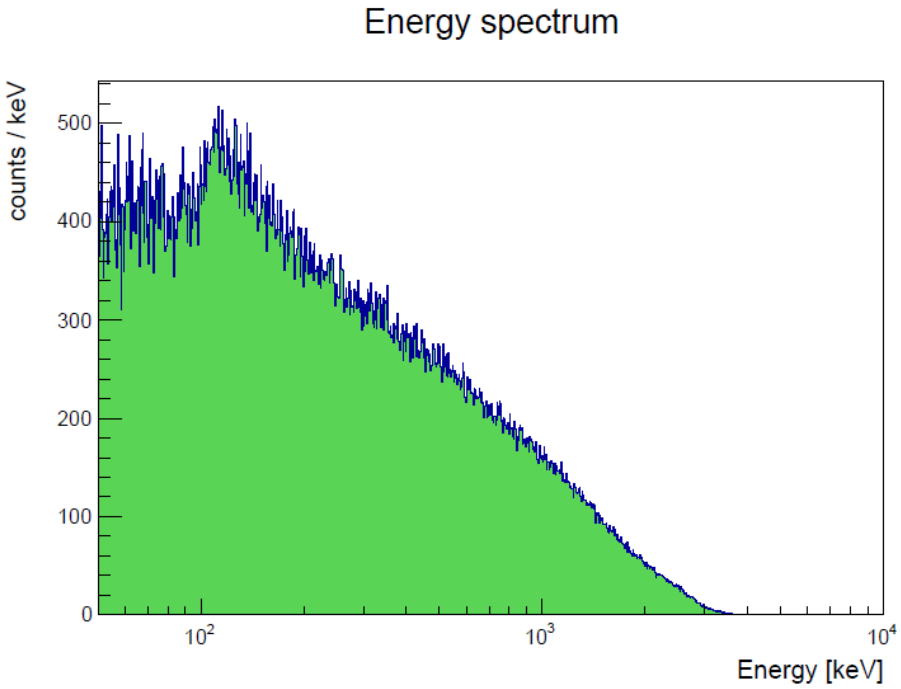

Figure 49: Representation of the energy spectrum of the recorded energy of a medium intensity TGF inside a human model volume, obtained by MEGALib.

Distance	**Triggered/Beamphotons**
5 km vertical	5.400×10^{8}
2.5 km vertical	2.250×10^{10}
0.5 km vertical	1.500×10^{12}
2 m vertical	7.218×10^{17}

Table 49: Source with a cone beam, with a power-law from 100 keV to 100 MeV, at a distance d from the aircraft advanced model; Average for 100 μs, for a human model consisting of water.

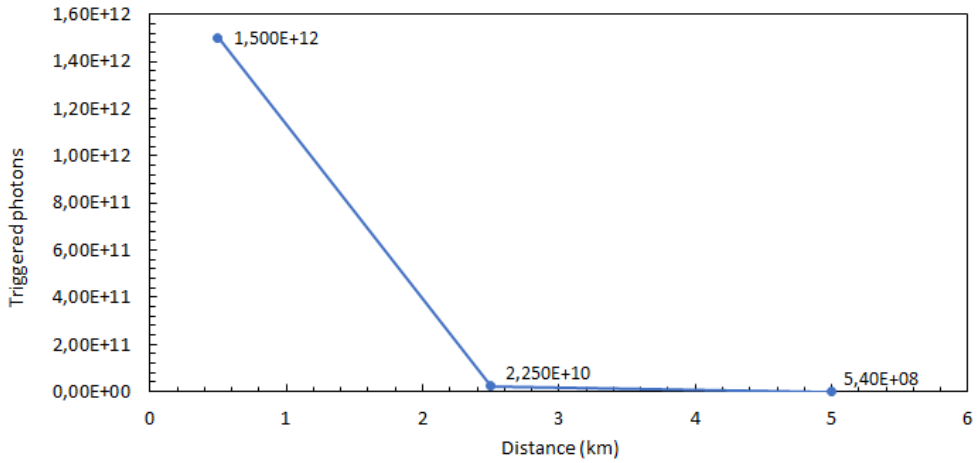

Figure 50: Triggered photons for a linear extrapolation to 100 μs, considering a cone beam incident on human model, inside the aircraft advanced model.

3.7.1 Absorbed dose for a human inside the aircraft advanced model

In the precedent set of simulations, a human model composed only by water provides a good estimation of the TGF radiation absorption. Furthermore, we are dealing with TGF and aircraft models that were not built with a high level of detail, therefore this water human model approach is largely satisfactory for the present level of simulations' accuracy. Through number of photons triggered inside the human body by a medium intensity TGF (1×10^{18} photons during 100 μs) , it is possible now to calculate the absorbed dose and the effective dose, concluding how severe the TGF emission is. We are going to consider 80 kg for the mass of the human being; 125 keV as average weighted energy from spectrum of fig. 49; the radiation weighting factor, for gamma-rays, is $W_r = 1$; and the human model consists of water and is in the position (0,0,0). Considering that the absorbed dose is defined as that the average energy deposited by the radiation in a volume of mass, as described in section 2.5.3:

$$D = E/m \quad Gray(Gy) \tag{10}$$

For this case, as $W_r = 1$, then the absorbed dose is equal to the equivalent dose, as also referred in section 2.5.3:

$$H = D \times W_r \quad Sievert(Sv) \tag{11}$$

The effective dose is defined as the sum of the equivalent weighted doses in all tissues

and organs of the body, resulting from internal and external irradiation. In this case, radiation from TGFs is only being considered, so the equivalent dose is considered to be equal to the effective dose. Also, 1 Gy = 1 J/kg = 1 Sv, so the values in the table 50 are in units of mSv, to make it easier to compare with the effective dose limits established by the general health department. The absorbed dose by the human model is calculated for each of the simulated distances. The values for the absorbed doses are in the table 50 below. The distance of 2 m from the aircraft advanced model, is the worst case scenario. However, it is a very unlikely situation, since pilots always try to avoid to cross cumulonimbus clouds, as it corresponds to a TGF being emitted just below the airplane fuselage during a flight trajectory that intercepts the cloud. In the contacts established with portuguese airline pilots, they confirmed us that it is rare, but sometimes it happens, that a pilot do not have any more options other than cross a cumulonimbus cloud. In this extremely unlikely scenario, the effective dose can reach fatal dose levels (> 10 Sv).

Distance	**Absorbed dose**
5 km	1.350×10^{-4} mSv
2.5 km	5.625×10^{-3} mSv
0.5 km	3.750×10^{-1} mSv
2 m	180.45 Sv

Table 50: Absorbed doses for the human model consisting of water, inside the aircraft advanced model, for medium intensity TGFs.

For more likely flights over cumulonimbus clouds emitting medium intensity TGFs at distances between 500 m up to 5 km, 1 mSv effective dose is not exceeded. However, for 500m we estimate a dose of 0.375 mSv, which contributes to the increase of the annual effective dose of an individual. It is known that the effective dose limit for the general public is 1 mSv per year, but they can exceed this value in one year, as long as the average dose in five consecutive years does not exceed 1 mSv. Regarding exposed workers, as aircraft crew members, they are allowed to higher dose limits, to a maximum effective dose of 50 mSv, so the effective dose absorbed by the crews for medium intensity TGFs at longer distances than 500m remain at acceptable levels. For a passenger irradiated by a medium intensity TGF at distances of about, it is very relevant to record that he was exposed to such dose since it represents about 38% of the 1 mSv limit.

3.7.2 Absorbed dose for strong TGFs: High flux

At this stage, a larger flow of TGFs was simulated, which we called a "strong TGF", to estimate again the effective dose absorbed by the human model inside the aircraft advanced model. The simulations are performed for the human model, maintaining the characteristics of the aircraft advanced model. The source remains with its conical shape

and underneath the aircraft model. Then, the only factor that changes is the flow used. A high flow of 1×10^{20} during 100 μs was considered, for distances from 2 m up to 5 km from the aircraft advanced model. As in the precedent section, through the triggered photons obtained by the simulation and applying the cone dispersion factor, the real photons that reach the human are obtained. Calculating the total energy of the photons and considering again that the human model is 80 kg, the absorbed dose formula is applied and the following values are obtained in the table 51 below.

Distance	**Absorbed dose**
5 km	0.589 mSv
2.5 km	20.1 mSv
0.5 km	210.6 mSv
2.0 m	1.854×10^{4} Sv

Table 51: Absorbed doses for the human model consisting of water, inside the aircraft advanced model for strong TGFs.

The effective doses estimated for a strong TGF present real risks to passengers and crew, because if an airplane is intercepted by one of these events, the annual limit of the effective dose for the general public is exceeded up to distances considerably longer than 2.5 km distances and for crews up to distances moderately longer than 500m. Again, even if in one year, the dose limit of 1 mSv can be exceeded, the absorbed dose of a passenger for a strong TGF for distances shorter than 2.5 km exceed the five year limit accumulated of 1 mSv per year. As mentioned above, crews have an annual effective dose limit of 50 mSv and 100 mSv of average effective dose, over five consecutive years. Clearly, for a flow of strong TGFs, these two values are exceeded for a source 500 m from the aircraft. For this reason, it is of great importance to tabulate and inform crews and the general public about the risks associated with these TGF emissions.

3.8 CdTe TGF Monitor

After the simulation set for a human model and the study of the absorbed and effective doses, a further set of simulations was performed in order to study the possibility of using a CdTe detector inside the aircraft cabin to operate as radiation monitor, providing alert and recording the detected TGFs intensity and spectral profile. With this information it is possible to estimate radiation dose absorbed by humans traveling inside an irradiated aircraft.

As mentioned in section 3.4.1, CdTe are very suitable to detect gamma-rays in the energy band where TGFs are more intense, specially in the 100 keV - 1 MeV domain, due to its good detection efficiency, among other advantages relative to other detectors. A a set of simulations was performed for a CdTe detector realistic volume: a cubic detector

with 1 cm size. The aircraft advanced model maintains the same characteristics, consisting of a 22 cm layer of aluminum and with *Material Air* inside. The CdTe detector is placed inside the airplane, at the position (0,0,0), as can be seen by the diagram in the figure 51. The data are in table 52 and represented in graph 52.

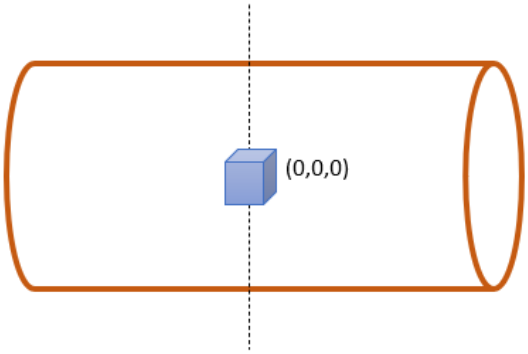

Figure 51: Diagram for the 1 cm edge CdTe detector, placed inside the aircraft advanced model.

Distance (km)	**Triggered/Beamphotons**
5 km vertical	1.997×10^{4}
2.5 km vertical	7.353×10^{4}
0.5 km vertical	4.912×10^{6}

Table 52: Triggered photons by approximation for a 1 cm edge CdTe detector.

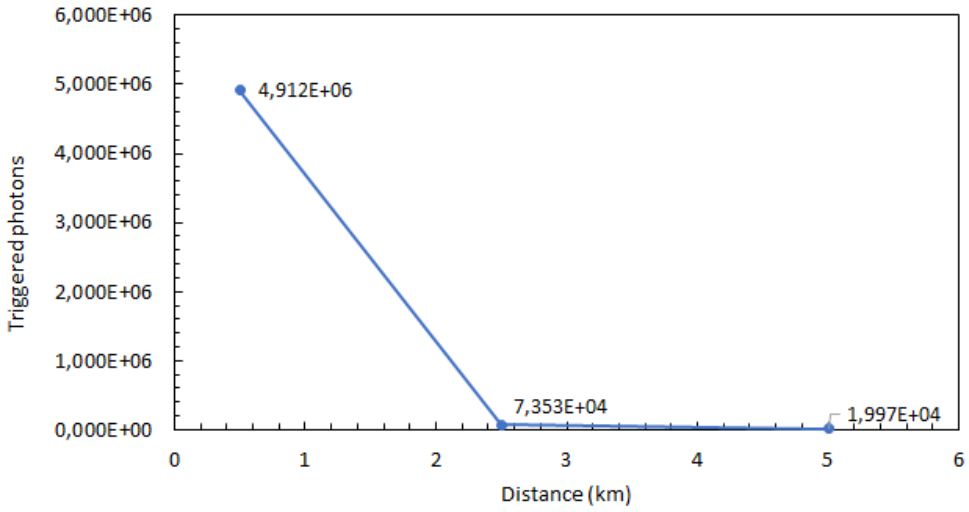

Figure 52: Triggered photons for a linear extrapolation to 100 μs, considering a cone beam incident on the CdTe detector, inside the aircraft advanced model.

It turns out that the triggered photons detected for distances of 5, 2.5 and 0.5 km are high, which allows us to conclude that the detector works and detects well, inside our advanced aircraft model. This corroborates that the production of a CdTe TGF monitor is quite feasible.

4 Chapter 4: Conclusions

The MEGAlib simulation model of a human inside an aircraft with a 22 cm thick cabin fuselage of aluminium, filled with air at 1 atm, when irradiated by a TGF emission at 500 m, modeled from real TGF data recorded by satellite gamma-ray observatories, provided an estimation for the effective dose absorbed by passengers or crew members, of the order of 0.375 mSv for medium intensity TGFs (1×10^{18} photons for 100 μs) and of 210.6 mSv for strong TGFs ($\sim 1\times 10^{20}$ photons for 100 μs). For TGFs 2.5 km distant from the aircraft, the effective dose was 5.625×10^{-3} mSv and 20.1 mSv, respectively for medium and strong TGFs, respectively. For 5 km distance the effective dose was 1.350×10^{-4} mSv and 0.589 mSv, for medium and strong TGFs, respectively. Bearing in mind that the effective dose limit for the general public is 1 mSv per year, that the dose for pilots and for crew members is 100 mSv for a period of five consecutive years (average dose for five years), and they can not exceed a maximum effective dose of 50 mSv each year, we can conclude from these results that medium intensity and mainly strong TGFs may expose passengers and crews to important risks. TGFs emissions at distances of about 500 m below an aircraft will have an impact on passengers and crew members' health, since the established limits for the absorbed dose per year will be clearly exceeded in the case of a strong TGF for a passenger over 2.5 km distance and for a crew member for distances over 500m away from the emission center. For a medium intensity TGF, we can conclude that at least the aircraft passengers should be informed of a TGF irradiation with its emission site at circa 500 m, since a substantial part of the the allowed dose limit per year (1 mSv) will be attained (38% for a 1×10^{18} photons and 100 μs duration TGF). Furthermore, for crew members, TGFs will contribute to increase their annual dose in addition to the effective dose generated by the cosmic radiation at which they are exposed, at altitudes of 7.5 up to 12.5 km above the ground.

Since the TGF emissions, according to the observations at a satellite altitude, follow a conical emission profile upwards, approximately in the zenith direction, with an average aperture of 30^{o}, the results above are of particular importance for the definition of the flight plan of an airline company operating in regions where cumulonimbus clouds are frequent and for the decisions and maneuvers that a pilot must take when cumulonimbus clouds form in the route of the aircraft. It is clear from this research work that pilots and airlines must avoid fly over or around the top cumulonimbus clouds during thunderstorms, since the risks of the exposure to TGF radiation is real and may have consequences on the health of crew and passengers. Furthermore emissions may present a certain inclination with respect to the zenithal direction and the plane could be within the emission cone zone, receiving a high amount of radiation. If possible airlines and pilots should circumvent cumulonimbus clouds, if possible at distances over 5 km to avoid any risks of direct irradiation or lateral TGF emissions, since so far there is still some uncertainty about the verticality of TGF emissions due to the lack of measurements at flight altitude.

Since TGFs might represent a hazard to commercial, scientific or military aviation,

in order to evaluate the possibility of measure TGF emissions for alert and recording the detected TGFs intensity and spectral profile, we simulated the response of a CdTe detector, with a volume of 1 cm^3. Even for a TGF at a distance of 5 km, and considering the dispersion in the atmosphere, the 1 cm edge detector can record a high count rate. Therefore, showing that this kind of device can operate as TGF monitor inside an airplane cabin.

As seen in chapter 2, the radiation value for which the most sensitive electronic devices have been damaged is D_c=5×10^3 rad = 50 Sv, which is a much higher value when compared to the effective dose limit for a human. Thus, we can conclude that for the airplane's electronic devices, TGF gamma-ray emissions are not particularly dangerous.

4.1 Limitations

The biggest limitation was the time it took Cosima to run for real flow simulations. The greater the number of triggers or events, defined in the source file, the longer the simulation time. After placing the actual flow, there was an even greater increase in the time the program took to run. For this specific case, time was used as a stopping factor, causing major complications in duration. Initially, a real-time of 100 μs was set, but it quickly moved to shorter times, since the simulations lasted for weeks. It was too long to run, and there were sometimes flaws on the internet. A few seconds without the internet immediately results in interrupting the simulation. To tackle this problem, it was thought to set a much lower stop criterion. The time intervals that allowed the shortest duration of the simulations were 1×10^{-15}s, 1×10^{-14}s, and 1×10^{-13}s, and for 1×10^{-12}s, this last one already implied a duration greater than 24 hours. The, through linear extrapolation it is possible to obtain a good estimate of the number of photons that reach the different materials.

Another limitation found was the situation of COVID-19, which prevented contacts from being made, to present TGFs and possible risks to aviation agencies. The goal was to get a partnership for the eventual and subsequent realization of a monitor to detect TGFs. This contact and construction project of the detector will be for future work.

4.2 Future work

As mentioned above, in this project the effect of neutrons has not been studied and neutron simulations were not performed because they require a higher degree of simulation code complexity and the aim of the present study was to analyse exclusively the effects of TGF radiation. The neutron impact on the absorbed dose will be considered in future work.

Another important aspect is the structure of the plane because, in addition to aluminum, the commercial aircraft has glass windows and composites in its structure. Therefore, a new approach could be to consider these composites that are based on carbon and

to see how the interactions happen.

According to the interviews conducted with an aircraft pilot and two mechanics of commercial aircraft, it is concluded that TGFs and any type of radiation event that occurs at flight altitudes are completely unknown by these professionals. There is no method carried out by the aeronautical agencies to measure the radiation dose absorbed by the pilots, nor to verify the damage that they can cause to the aircraft's electronic devices. There is no specific device for detecting TGFs or cosmic rays that exist in the atmosphere. The only study carried out was a master's thesis from the Faculty of Science and Technology of Universidade Nova de Lisboa, which built a prototype that allows identifying each crew member using a personal identification card, and also measuring and recording the radiation levels to which each member is exposed during one flight [16]. However, there is no knowledge that it has developed further than the prototype.

Therefore, it is concluded that it is really important to obtain measurements at flight altitudes, something that has never been done, and for this, a detector is required. Instead of the use of dosimeters by pilots and flight attendants that are analysed after weeks or moths their first use, a radiation detector on board a commercial aircraft allows to know the amount of dose absorbed during a commercial flight, in particular if the crew was exposed to TGF, the respective duration, and a real data set is obtained. The results here presented demonstrate that a 1 cm^3 volume CdTe monitor has the potential to perform this measurements. At the present time a project proposal is being elaborated to SPARK 4 TECH, a project call by Instituto Pedro Nunes and the Telecommunications and Integrated Applications Directorate of the European Space Agency, for feasibility studies regarding the transfer of technology. This is a proof of concept project of a CdTe based TGF monitor, to operate inside the cabin of commercial, scientific or military aircrafts. With these devices it will also be possible to study in more depth the horizontal TGF emissions and verify that the cone shaped emission profile is a reliable TGF emission characterization.

References

[1] Cari.(accessed: 23.07.2020). www.cariwellbeing.co.uk/cari.html.

[2] Community coordinated modeling center.(accessed: 23.07.2020). https://ccmc.gsfc.nasa.gov/modelweb/models/nrlmsise00.php.

[3] *Diário da República, 1.ª série — N.º 223 — 17 de Novembro de 2008.*

[4] Epcard.(accessed: 23.07.2020). www.helmholtz-muenchen.de/en/epcard-neu/index.html.

[5] Esa.(accessed: 23.07.2020). http://www.esa.int/Science_Exploration/Human_and_Robotic_Exploration/Secret_life_above_thunderstorms_uncovered.

[6] Geant4.(accessed: 23.07.2020). https://geant4.web.cern.ch/.

[7] Otd.(accessed: 11.05.2020). http://ghrc.nsstc.nasa.gov/lightning/overview_otd.htm.

[8] Pcaire.(accessed: 23.07.2020). new.pcaire.com/.

[9] Sata.(accessed: 28.10.2020). https://www.sata.pt/pt-pt/sata/frota.

[10] Sievert.(accessed: 23.07.2020). https://www.sievert-system.org/?locale=en.

[11] Tap.(accessed: 28.10.2020). https://www.flytap.com/pt-pt/a-bordo/conhecer-a-frota?tabid=filters-tab3.

[12] Ute Ebert Christoph Köhn. *Angular distribution of Bremsstrahlung photons and of positrons for calculations of terrestrial gamma-ray flashes and positron beams.* 2013.

[13] Geant4 Collaboration. *Book For Application Developers.* December 6th, 2019.

[14] T. Gjesteland Collier, A. B. and N. Østgaard. *Assessing the power law distribution of TGFs.* Journal of Geophysical Research, 2011.

[15] V. Connaughton. *Associations between Fermi Gamma-ray Burst Monitor terrestrial gamma ray flashes and sferics from the World Wide Lightning Location Network.* Journal of Geophysical Research, 2010.

[16] Joaquim João da Silva Horta. *Desenvolvimento de um Sistema para Monitorização de Dose de Radiação em Cockpit de Avião - Dissertação para obtenção do Grau de Mestre em Engenharia Biomédica.* 2013.

[17] Sheila McBreen Gerard Fitzpatrick, Eric Cramer. *Compton Scattering in Terrestrial Gamma-ray Flashes detected with the Fermi Gamma-ray Burst Monitor.* 2015.

[18] Thomas Gjesteland. *Properties of Terrestrial Gamma ray Flashes.* Department of Physics and Technology, University of Bergen, April 2012.

[19] G. C. Gonçalves. *Consequências da exposição à radiação cósmica em pilotos.* 2018.

[20] Gustavo Gonçalves. *Consequências da exposição à radiação cósmica em pilotos.* 2018.

[21] D. J. Boccippio H. J. Christian, R. J. Blakeslee. *Global frequency and distribution of lightning as observed from space by the Optical Transient Detector.* 2003.

[22] D. M. Smith J. R. Dwyer. *A comparison between Monte Carlo simulations of runaway breakdown and terrestrial gamma-ray flash observations.* Geophysical research letters, 2005.

[23] M. M. Schaal J. R. Dwyer. *Observation of a gamma-ray flash at ground level in association with a cloud-to-ground lightning return stroke.* 2012.

[24] F. Fuschino M. Marisaldi. *Detection of terrestrial gamma ray flashes up to 40 MeV by the AGILE satellite.* Journal of Geophysical research, 2010.

[25] M. Tavani M. Marisaldi, F. Fuschino. *Properties of terrestrial gamma ray flashes detected by AGILEMCAL below 30 MeV.* 2014.

[26] A. Argan M. Tavani. *Possible effects on avionics induced by terrestrial gamma-ray flashes.* 2013.

[27] C. Labanti M. Tavani, M. Marisaldi. *Terrestrial Gamma-Ray Flashes as Powerful Particle Accelerators.* 2011.

[28] G. Barbiellini M. Tavani. *Science with AGILE.* 2004.

[29] T. A. Silva M. V. Costa. *A Importância do Radar Meteorológico de Bordo na Prevenção de Acidentes Aeronáuticos da Aviação Geral.* IX Simpósio de Segurança de Voo.

[30] B. Malfitano. *Understanding airplanes.* 2018.

[31] Aviation Handbooks Manuals. *Aircraft Structure, Chapter 2.*

[32] J. T. Bonnell R. J. Nemiroff and J. P. Norris. *Temporal and spectral characteristics of terrestrial gamma flashes.* Journal of Geophysical Research, 1997.

[33] J. B. Stephen R. M. Curado da Silva, E. Caroli and P. Siffert. *CIPHER, a polarimeter telescope concept for Hard X-ray Astronomy.* Exp. Astron., Vol. 15, n°1, pag. 45-65, 2003.

[34] N. Auricchio et al R. M. Curado da Silva, E. Caroli. *Hard-X and Soft Gamma-ray Polarimetry With CdTe Array Prototypes.* IEEE Trans. Nucl. Sci., Vol. 51, n 5, pp. 2478-2484, 2004.

[35] G. Fitzpatrick S. Foley. *Pulse Properties of Terrestrial Gamma-ray Flashes detected by the Fermi Gamma-ray Burst Monitor.* Journal of Geophysical research, 2015.

[36] M. S. Briggs S. Foley, G. Fitzpatrick. *Pulse Properties of Terrestrial Gamma-ray Flashes detected by the Fermi Gamma-ray Burst Monitor.* 2015.

[37] M. Stolzenburg T. C. Marshall. *Voltages inside and just above thunderstorms.* 2001.

[38] N. Østgaard T. Gjesteland. *Effects of dead time losses on terrestrial gamma ray flash measurements with the Burst and Transient Source Experiment.* 2010.

[39] N. Østgaard T. Gjesteland. *Observation of intrinsically bright terrestrial gamma ray flashes from the Mediterranean basin.* 2015.

[40] S. Heever W. Cotton, G. Bryan. *Storm and Cloud Dynamics*, volume 99. 2011.

[41] Andreas Zoglauer. *Cosima: A Cosmic Simulator for MEGAlib based on Geant4.* 2015.